Concentrated Solar Power Development for Milk Pasteurization in Rural South Africa

by

James Mallett

Thesis presented in partial fulfilment of the requirements for the degree of Master of ***Engineering in Electronic Engineering*** *in the Faculty of Engineering at Stellenbosch University*

Supervisor: Prof. M. Maaza

Co-supervisor: Prof. W.J. Perold
Dr. S. Khamlich

April 2019

Declaration

By submitting this thesis electronically, I declare that the entirety of the work contained therein is my own, original work, that I am the sole author thereof (save to the extent explicitly otherwise stated), that reproduction and publication thereof by Stellenbosch University will not infringe any third party rights and that I have not previously in its entirety or in part submitted it for obtaining any qualification.

Date: April 2019

Abstract

This thesis explains the designs, technologies and testing procedures used to develop a low-cost parabolic solar reflector unit for the pasteurization of raw milk.

Throughout Southern Africa there are large portions of the population that rely on milk as a source of nutrition and income. However, for those that do not have access to adequate infrastructure including electricity, this can pose challenges. Raw milk can be home to significant amounts of bacteria and pathogens, which can cause it to be potentially unsafe for consumption. Raw milk will also spoil in a short space of time, if not treated properly. The process of milk pasteurization involves heating it to specific temperatures for certain periods of time, and by doing so bacteria can be destroyed, increasing the lifespan of the milk. The energy required for this heating process can be problematic or resource dependant, but fortunately solar energy is abundant in Southern Africa.

By utilizing a solar concentrating device, the energy needed for heating can be obtained directly from the sun at zero cost. A parabolic trough was designed to perform this function, which allows for continuous flow pasteurization. An important component in such a system is the receiver tube solar absorber coating, which is responsible for absorbing the concentrated energy. For this reason, additional analyses was done on a commercial selective solar absorber, black spray paint and a candle soot coating as potential low cost receiver tube coatings. These were characterized using UV-vis-NIR and Raman spectroscopy, HR-SEM, HR-TEM, EDS and XRD.

The parabolic trough system was tested by heating water to the temperatures necessary for pasteurization. Each of the receiver tube solar absorber coatings were used, and temperatures above 75 °C were achieved with all of them. The system was then tested using milk, and the same temperature ranges were obtained, allowing the milk to be successfully pasteurized.

Acknowledgements

The author of this thesis, James Mallett would like to thank the following people for their contribution to this project.

- Prof. Malik Maaza, for the fantastic opportunities that have been made available to me, and the exceptional supervision and ideas throughout the duration of the project.
- Dr. Saleh Khamlich, for providing invaluable advice, recommendations and extensive support every step of the way, your guidance was greatly appreciated.
- Prof. Willem J Perold, for the valued assistance on the project and positive outlook during the past two years.
- Peter Paulson, and the rest of the workshop staff at iThemba labs, for their guidance with refining the CSP design, and construction of the system.
- My parents and siblings, for their continual love and support throughout my life and for helping to get me where I am today.

Contents

List of Figures

List of Tables

Nomenclature

Variables

a	Aperture width
A_a	Aperture area
A_f	Geometric factor
A_l	Total aperture area loss
c_p	Specific heat
C_g	Concentration Ratio
d_{min}	Minimum solar beam disk
d_o	Receiver tube outer diameter
$E_{optical}$	Rate of optical radiation incident on a solar absorber
f	Focal length
F_R	Collector heat removal factor
h	Parabola height
$h_{w,r,c}$	Wind(convective), radiation and conductive losses
I_s	Direct solar irradiance
l	Trough length
$\dot{m}$	Mass flow rate
η_{col}	Collector efficiency
η_o	Optical efficiency
$\dot{Q}_{loss}$	Rate of energy loss by solar collector system
$\dot{Q}_u$	Rate of useful energy obtained by solar collector system
T	Temperature
U_L	Loss coefficient

Symbols

α	Solar Absorptance
β	Angle of misalignment
γ	Intercept factor
ε	Thermal Emissivity
θ	Solar zenith angle, Incidence angle
λ	Wavelength
ρ	Reflectance

τ Transmittance
ψ Rim angle

Constants

Sun Hour $= 1000\ \mathrm{W\,h\,m^{-2}}$
σ $= 5.6696 \times 10^{-8} Wm^{-2}K^{-4}$ Stefan-Boltzmann Constant
AM 1.5 Solar data at Air Mass 1.5

Abbreviations

ALP Alkaline Phosphatase
BSE Back Scattered Electron
CCD Charge-Couple Device
CFU Colony Forming Unit
CIP Clean-in Place
CSP Concentrated Solar Power
DHI Diffuse Horizontal Irradiation
DNI Direct Normal Irradiation
EDS Energy-dispersive X-ray spectroscopy
EU European Union
FDA Food and Drug Administration
FEG Field-Emission Gun
GHI Global Horizontal Irradiation
HR-SEM High Resolution Scanning Electron Microscopy
HR-TEM High Resolution Transmission Electron Microscopy
HTF Heat Transfer Fluid
NIR Near Infrared
PMO Pasteurized Milk Ordinance
PSD Particle Size Distribution
PV Photovoltaic
PWM Pulse width modulation
SAED Selected Area Electron Diffraction
SAURAN South African Universities Radiometric Network
SE Secondary Electron
SUN Stellenbosch University
TES Thermal Energy Storage
UV Ultraviolet
vis Visible light
XRD X-ray Diffraction

Chapter 1

Introduction

In the developing world, more specifically in regions of southern Africa, a substantial percentage of the populations currently living in rural areas do not have sufficient infrastructure available or an electricity supply that is reliable. In 2016 in sub-Saharan Africa, only roughly 42% of the total population, and 25% of those in rural areas, had access to electricity. [1, 2]. Many of the people that live in these communities, depend on their own produce to provide them with their primary source of sustenance and/or income [3]. Among these sources of produce is milk which is produced from dairy cattle. This forms a substantial amount of the total calories and nutrition that citizens of these developing areas have access to on a daily basis [4]. Raw milk can, however, potentially become unsafe for human consumption, as it can attract and contain sizeable amounts of harmful bacteria. If not treated properly within a short space of time this milk is also prone to spoiling, which can be a waste of the limited available resources to people in these poor communities [5].

Pasteurisation is a simple process of milk treatment using heat, whereby it is held at certain elevated temperatures for predetermined periods of time. By doing so, the unsafe pathogens present in the raw milk are destroyed while simultaneously increasing the milk's life span, this is done while leaving its nutritional properties unaffected [6]. The problem lies, however, in regions where the necessary infrastructure, equipment or resources are unavailable, meaning the required heating process could be too challenging or expensive to perform [2]. Some of these challenges could be mitigated by making use of solar energy, an abundant resource in Southern Africa, as the primary and sole source of energy for the heating procedure [7]. By concentrating solar radiation in a way that it can be harnessed to heat the milk, the temperatures necessary for pasteurization can be reached without the need for any other fuel sources or electricity [2].

Capturing the solar energy incident on earth's surface using Concentrated Solar Power (CSP) technology, rather than non-concentrating solar devices, can allow higher temperatures to be reached and process times to be reduced [8]. This concentration could be implemented on a small scale by using a parabolic trough system, whereby the solar energy that falls on an aperture plane will be reflected onto a receiver tube. The energy concentrated onto the tube will then be absorbed and transferred to the fluid being pumped inside, milk in this case, and heat it to the temperatures required for pasteurization to take place [2]. To maximize the amount of solar energy absorbed by the receiver tube and to reduce the thermal emissions, selective solar absorbers can be coated onto the tube exterior [9]. These are coatings of various compositions and

materials that are designed to absorb maximum amounts of solar energy while radiating as little heat as possible.

In some parabolic trough systems and in most commercial systems, evacuated glass tubes are used around the receiver tube to further increase performance by reducing heat loss. The cost of using tubes such as these does, however, significantly increase the overall cost of parabolic trough systems. These tubes are also fragile and if the systems are being used in remote areas of the country, broken tubes can be expensive and difficult to replace [2, 10]. If the necessary temperatures can be achieved using materials that are cheaper and more widely available for people in rural areas, then the overall cost of the system can be reduced. This will improve the practicality of the system while also simplifying the design [2].

1.1 Objectives of this study

The goal of this thesis is to design, develop and test a small scale parabolic trough that would be able to achieve the temperatures necessary for the pasteurization of milk, and determine whether or not this is a viable solution to be used in rural areas of Southern Africa. This device would need to be mobile, easy to fix or maintain, and have a relatively low cost.

1.2 Contributions

The following outcomes were ultimately throughout the duration of this project and are detailed within this thesis:

- A small parabolic trough CSP system was successfully designed, built and tested.
- In-depth characterizations of a selective solar absorber, a candle soot based coating and black spray-paint gave valuable information about potential receiver tube coatings for use on the device.
- The trough was able to reach temperatures of around 100 °C with 3 different types of receiver tube coatings.
- The trough was able to successfully pasteurize raw milk using a novel low-cost receiver tube coating that could be available to anybody in the world, the candle soot.
- The trough used widely available materials such as stainless steel, mild steel and aluminium, instead of highly specialised materials that are generally used for the reflective mirrors and receiver tube.
- Sections of this thesis were presented at the Africa Material Research Society(AMRS) conference in Botswana, 2017. The same sections were also used in a publication of a paper by the Author in *MRS Advances*, April 2018, that is titled "Comparative study of flat and cylindrically-shaped selective solar absorber for CSP application". The contents of this paper, the details of which are highlighted in Appendix F, form a part of Chapter 5 of this thesis.

1.3 Chapter overviews

This thesis is broken down in seven main chapters, including the current introductory chapter. A brief overview for each of the following chapters is given below:

Chapter 2: Background study

This chapter covers the background study and literature review of the various different fields that are relevant to this thesis. Background studies were done on solar energy, CSP systems, small scale solar energy applications, milk pasteurization and existing applications that utilize solar power for pasteurization.

Chapter 3: Parabolic trough design

In this chapter, the design of parabolic trough systems is discussed, along with all the necessary factors that need to be taken into account in the design process. A description of the designed and constructed system that was used is given, including all the relevant components and methods that were used.

Chapter 4: Methods

This chapter discusses the methods and techniques used for characterization and analysis of the solar absorbers which are detailed in Chapter 5. The methods used include X-ray diffraction (XRD), high resolution scanning- and transmission- electron microscopy (HR-SEM, HR-TEM), Raman spectroscopy, and spectroscopy in the ranges of Ultraviolet, visible light and near infra-red (UV-vis-NIR).

Chapter 5: Solar absorber characterization

In this chapter the studies that were conducted on solar absorber alternatives are presented. This includes analysis that was done on a commercial selective solar absorber and black spray-paint, and characterization that was done on soot particles.

Chapter 6: CSP milk pasteurizer performance results

The results that were obtained in the testing of the CSP milk pasteurizing system are given in this chapter. The temperatures that were reached on each of the test days are illustrated and discussed, and the performance of the system is analysed.

Chapter 7: Conclusion and recommendations

This chapter presents the conclusion of the thesis and discusses all that is contained and accomplished within. Recommendations are also given for future research and potential applications of this system.

Additional document: Drawing pack

In addition to this thesis, a folder will be provided containing all relevant assemblies, sub-assemblies and individual part drawings of the designed system.

Chapter 2

Background study

This chapter highlights the literature and background knowledge that is relevant to the different aspects of the CSP system which was designed. The information that is included covers the two fields that are important to this project. The first field covers elements of solar powered systems, such as solar energy, CSP systems and small scale solar energy applications. The second covers details about the necessity of and process of milk pasteurization, highlighting the hazards of raw milk consumption, confirming pasteurization effectiveness and various ways that solar power has been used previously for pasteurization.

2.1 Solar energy

This section gives an overview of solar energy as a whole and the aspects of it that are important in harnessing its energy.

2.1.1 Solar energy overview

Solar energy is the most abundant renewable energy resouce available, and it is also the cleanest [11]. The technologies responsible for harnessing the solar radiation and converting it into useful energy are classified as either active solar energy, or passive solar energy systems [12].

Active solar energy systems rely on mechanical or electrical devices in order to convert the solar energy into another useful form, such as electricity or heat. Passive solar energy systems do not rely on any other devices and aim simply to utilize the local climate to heat buildings in winter and reflect excess heat in the summer [12].

2.1.2 Renewable solar energy

Renewable energy is energy that is harnessed from sources that are able to replenish themselves naturally over short periods of time. These sources cannot be depleted regardless of the amount of energy that is extracted. Finite energy sources such as oil, coal and natural gas are known as Fossil fuels, and these, once exhausted, are not able to be replenished. Renewable energy sources also provide energy that is much cleaner than the fossil fuel alternatives, meaning fewer pollutants and greenhouse gases are emitted during the use thereof [13, 14].

The renewable energy source that contributes the most to the worlds electricity supply is by far hydroelectric energy. It generates around 83% of the world's supply of renewable energy. The source with the second largest contribution is wind energy at over 7%, and at just under 7% are the combination of bio-waste and bio thermal energy. Geothermal energy has a 2% contribution, and the remaining percentage is made up of solar, tidal and wave energy combined [14].

Passive solar energy systems are often implemented in architecture and building design, where the natural heating and cooling processes caused by thermal convection, are taken advantage of and incorporated into buildings. A few other applications of passive solar include cool roofs, green roofs and radiant barriers, which all have the aim of reducing the amount of heat absorbed by the building [12].

There are two types of active solar energy systems, known as either Photovoltaic (PV) or CSP systems. PV panels harness solar energy as electricity directly by the phenomenon known as the photovoltaic effect. PV arrays usually consist of an arrangement of solar panels, which are collections of multiple, sometimes even hundreds of thousands, solar cells [12]. CSP systems however, use mirrors or lenses to reflect and concentrate the solar energy onto a focus point, where a fluid is then heated for use in further processes to generate electricity, or for other applications. The four main types of CSP systems are parabolic troughs, solar towers, Fresnel reflectors and Stirling dishes [12].

PV technology is not only used in large solar plants, but also in many smaller applications where it is extremely useful. Solar panels are used to provide electricity for houses and buildings when fixed onto their roofs, they are also often used to power street and highway lights, calculators and even water pumps [12].

CSP systems also have applications on a smaller scale, such as solar cookers, which are used in rural areas all over the world to cook food or clean water by boiling it [12]. These systems can even be used as solar water heaters, which convert the energy of the sun during the day to drive a convection process that heats water without the need for pumps or electricity [15].

2.1.3 Solar radiation

Solar radiation is the radiant energy that is emitted from the sun, caused by its nuclear fusion reactions, that provides earth with all of its heat and light. The solar radiation spectrum can be split into three main components, which are the UV-vis-NIR wavelengths. Around 42.3% of the radiation reaches the earth with a wavelength of between 0.4 µm and 0.7 µm, which makes up the visible light spectrum. Above 0.7 µm makes up the IR region, which accounts for 49.4% of the solar spectrum. The remaining 8% of the total solar radiation, which falls below 0.4 µm, is classified as UV radiation [16]. The incident solar radiation, also known as insolation, is the amount of solar radiation that reaches the earth's surface. This is measured as irradiance, which is the radiant flux received by a surface per unit area. Figure 2.1 shows all of these wavelengths at sea level and before they encounter earth's atmosphere, along with the spectral irradiance that each wavelength possesses [17].

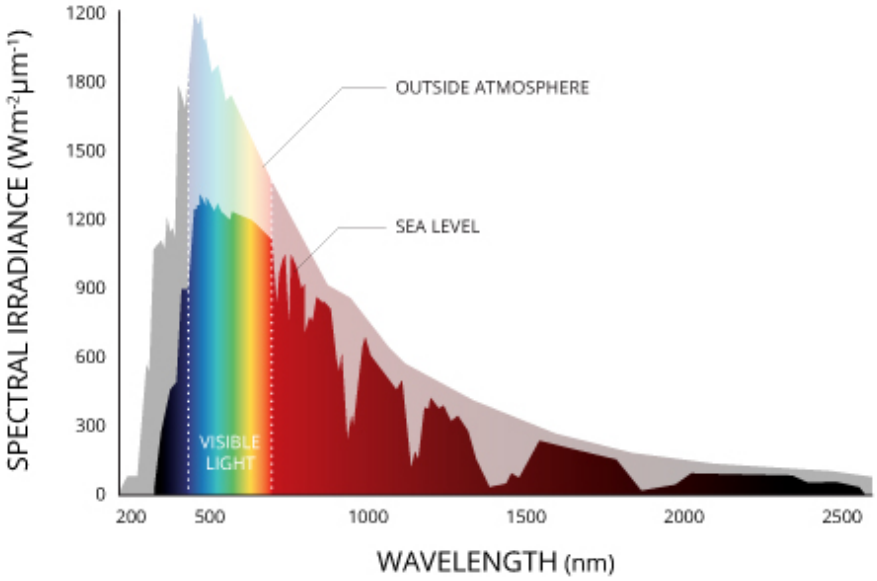

Figure 2.1: Solar radiation spectrum [17].

Before the solar radiation can reach the surface of the earth, it passes through multiple layers of the atmosphere, where some of the energy is reflected, absorbed and scattered. Clouds and other particles in the atmosphere directly scatter and reflect approximately 26% of the solar energy back into space, and around 18% of the energy is absorbed by the atmosphere, leaving only 56% of the energy to reach the earth's surface [17].

The energy that is eventually received on the earth's surface can then be classified using three different terms, Global Horizontal Irradiation (GHI), Direct Normal Irradiation (DNI) and the Diffuse Horizontal Irradiation (DHI). DNI accounts for the solar energy that is received on a straight line from the direction of the sun by a surface held perpendicularly to the rays. DHI is the radiation that is received indirectly from the sun, due to scattering in the atmosphere, and GHI is the sum of the direct and diffuse irradiations, shown by

$$GHI = DHI + DNI\cos(\theta) \tag{2.1}$$

where the solar zenith angle, θ, is the angle that the sun is away from being vertical [18].

For CSP systems, because their functionality is based on the concentration of direct solar energy, only the DNI of an area is considered when evaluating suitable locations. With PV systems, the GHI can also be considered, because the technology is able utilize both the diffused and direct irradiation of the sun to produce energy. Figure 2.2 shows the long term average of DNI across the world, with the regions of highest direct solar energy being shown with red and purple colours.

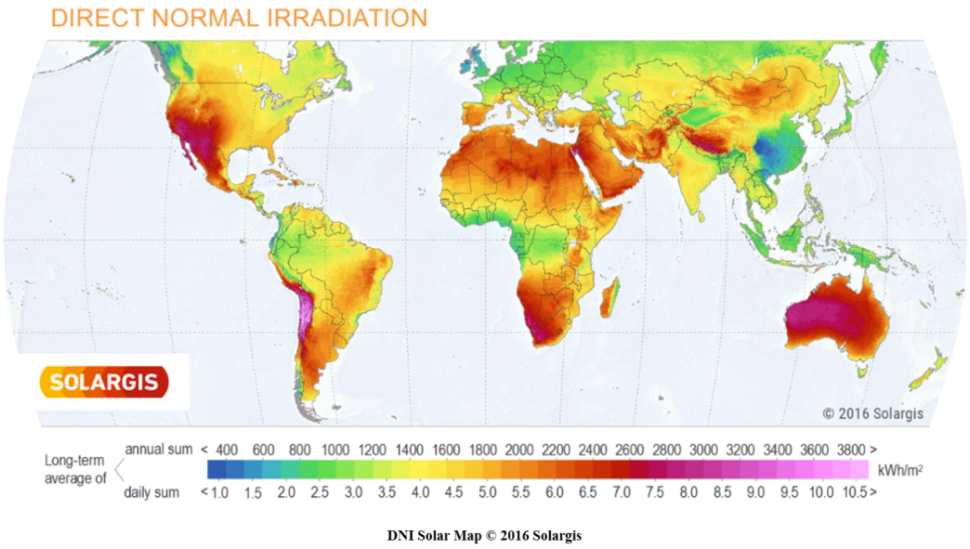

Figure 2.2: World DNI map [7]

The majority of areas in South Africa receive more than 2500 hours of sun per year (1 Sun hour = 1000 Wh/m^2) on average, with average solar radiation levels ranging between 4.5 and 6.5 kWh/m^2 each day. This is shown for South Africa in Figure 2.3 [19]. These high levels of solar radiation place South Africa among the countries with the highest potential for solar energy, compared to places such as Europe, that only receive around 1000 sun hours per year and are still among the leaders in solar energy generation [20]. Even in the coastal regions of South Africa, where the average annual DNI sits in the range of about 1400 and 1800 Wh/m^2, there is still a substantial amount of energy that can be harnessed.

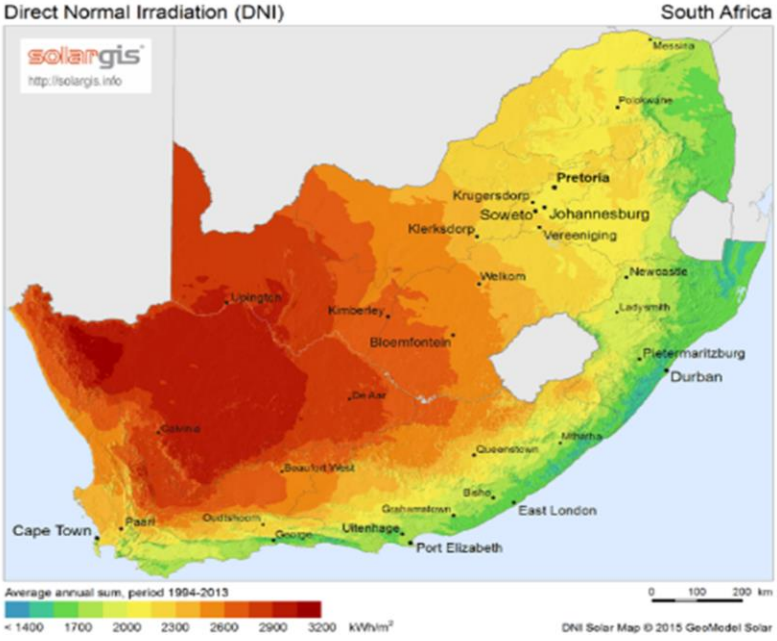

Figure 2.3: South Africa DNI map [7]

2.2 Concentrated solar power systems

This section focuses specifically on CSP systems, their designs, functionality and uses throughout South Africa and the World.

2.2.1 Technology overview

As of 2018, the most common type of CSP technology in use around the world is the parabolic trough system, which is thought to be the most commercially proven and developed of the different CSP technologies [21]. This system is a type of linear concentrator that uses mirrors or reflective sheets in a parabolic shape to reflect DNI onto a focus point, where a receiver tube is positioned. This is illustrated in Figure 2.4. A Heat transfer fluid (HTF) that flows through these receiver tubes then absorbs the heat from the concentrated solar energy, which is then used to generate electricity by creating steam and powering a steam turbine and generator [22]. These systems are implemented on a very large scale and generally consist of multiple rows of reflectors that stretch hundreds of meters.

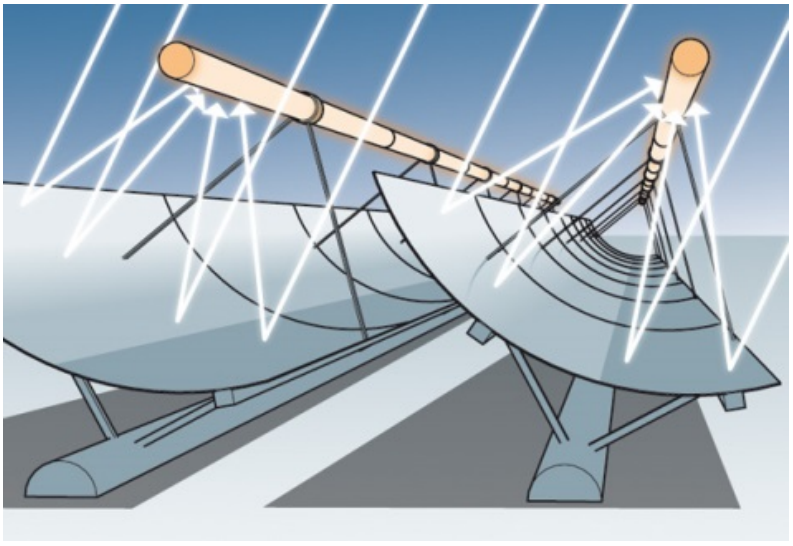

Figure 2.4: Simplified parabolic trough [23]

The solar tower is another type of CSP technology that is also used on a large scale for energy generation. These systems use flat mirrors, known as heliostats, to focus the solar energy onto a single receiver that is located at the top of a high tower, shown in Figure 2.5. These mirrors are individually automated allowing them to accurately track the sun and ensure that they are reflecting its energy in the correct direction [24]. The intense heat that is generated in the receiver, and which can even reach temperatures of 1000 °C, is then used to create steam to drive generators [25, 26]. The Ivanpah Solar Electric Generating System, which is currently the largest CSP plant in operation, has a capacity of 392 MW and incorporates 173500 heliostats and three different receiver towers [24].

Figure 2.5: A solar tower system [27]

The other two CSP technologies, which have not been implemented on scales as large as parabolic trough and solar tower plants, are known as Linear Fresnel reflector systems and Dish/Engine system respectively. The Fresnel systems use designs that are similar to parabolic troughs and are based on concentration to a receiver tube. However, instead of a parabolic mirror, they use multiple flat or slightly curved mirrors on a horizontal axis to focus the sunlight onto the receiver tube. This is illustrated in Figure 2.6 [22].

Figure 2.6: Linear Fresnel reflector [28]

The parabolic dish/Stirling engine systems, shown in Figure 2.7, use a parabolic dish mirror to reflect the solar energy onto a single focus point. These systems generate electricity differently than other CSP technologies, and use a Stirling engine placed at the focus point to generate electricity directly from the concentrated heat. These systems are generally used on a smaller scale in modular applications and can generally have capacities of between 3 and 25 kW each [29].

Figure 2.7: A parabolic dish concentrator with Stirling engine [30]

2.2.2 Noteworthy system components

In a conventional CSP system, excluding the Stirling engine systems, there are five different steps in the process of energy generation, which were summarised by Weinstein (2015) as follows:

1. Concentration: Solar energy that falls on a concentrating surface is redirected to a receiver.
2. Absorption: The energy received is absorbed and converted to heat.
3. Transfer: Heat is carried away by a HTF.
4. Storage: If needed, the heat can be stored for later use in thermal energy storage (TES).
5. Generation: The HTF provides a heat engine with the necessary heat to generate electricity.

In each of these steps, there are many different components that can greatly affect the overall performance of the CSP system. These components can affect the design parameters and change the overall dimensions of the system. On smaller scale systems, where the CSP system does not generate energy, there are a few important components that can be substituted and changed on a system that has already been constructed, which can have large effects on the overall efficiency. Two of these components are the reflective material used for the mirrors and the coating that is used on the outside of the receiver tube. Each of these can each make a big difference to the concentration and absorption properties of the system, which have a significant effect on the efficiency of the system as a whole.

In all concentrating solar collectors, the aim of the reflective mirror is to reflect as much of the solar energy that falls onto its surface area onto the receiver. Assuming that the system is designed to correctly target the reflected sunlight at the receiver, the reflective efficiency will be dependent on the optical properties of the material, in particular the spectral reflectance of the surface [31].

Silver and aluminium are known to have the highest reflectance, of around 97% and 92% respectively, and tend to be the most common reflective coatings in CSP systems [32]. In modern systems, however, reflective mirrors consist of several different layer combinations, with the purpose of improving the mechanical strength and lifespan of the mirrors while still achieving maximum reflection [33].

In parabolic trough and Fresnel type collectors, the coatings used on the receiver tube also play an important role in the system's overall efficiency. The simplest form of absorber coating would be a black body absorber, which would absorb energy of wavelengths that are directed towards it and end up on its surface. These types of absorbers do, however, also have the maximum amount of heat losses due to their thermal emission properties [31]. Selective solar absorbers are more commonly used, where coatings sacrifice a small portion of their solar absorptance to incorporate certain materials or structures that allow them to have reduced thermal emission [31]. This reduction in absorptance is justified by the large reduction of losses that would be caused by absorption of wavelengths in the IR region, which drives thermal emission, making it a much more efficient alternative. The ideal selective solar absorber would thus be able to absorb all solar radiation, except that which falls in the IR range, which would be reflected onto it. This concept is illustrated in Figure 2.8, where the reflective properties of an ideal selective solar absorber is shown relative to the solar energy spectrum and the radiation of a black body at 350 °C.

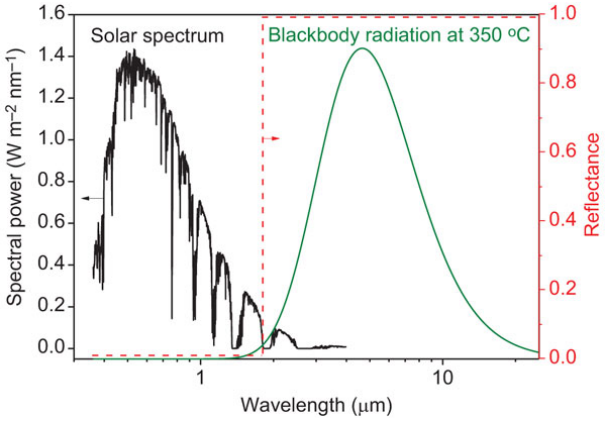

Figure 2.8: Ideal selective solar absorber behaviour [34]

If both the reflective mirror and the absorber tube coating can be chosen to have the best possible properties, while still keeping costs and other design parameters in mind, the overall efficiency of the small scale CSP system can be increased dramatically. On larger scales, these also play a large role in the overall system efficiency. However, the other system processes, such as heat transfer, heat storage and electricity generation are just as important and need to be designed perfectly.

2.2.3 Selective absorber surface coatings

In all parabolic trough systems, receiver tube surface coatings play an important role in the improvement of overall system efficiency. The performance of these coatings are assessed based on their solar absorptance and thermal emittance properties. To ensure

efficiency is kept as high as possible, these coatings need to have a high solar absorptance and low thermal emittance at the operating temperature of the system [35]. For opaque materials, the solar absorptance α, and thermal emissivity ε, can be expressed in terms of the total reflectance ρ, using Kirchoff's law, where

$$\alpha(\lambda, \theta) = 1 - \rho(\lambda, \theta) \tag{2.2}$$

and

$$\varepsilon(\lambda, T) = \alpha(\lambda, T) \tag{2.3}$$

and where λ is the wavelength, θ is the incidence angle of light and T is the given temperature [35]. These equations can be expanded, and by using measurements of the reflectivity that the surface has at different wavelengths, its absorption and emittance can be calculated as

$$\alpha(\lambda) = \frac{\int_{\lambda_1}^{\lambda_2} [1 - \rho(\lambda)] I_s(\lambda) \mathrm{d}\lambda}{\int_{\lambda_1}^{\lambda_2} I_s(\lambda) \mathrm{d}\lambda} \tag{2.4}$$

$$\varepsilon(T) = \frac{\int_{\lambda_{min}=0}^{\lambda_{max}=\infty} [1 - \rho(\lambda, T)] b(\lambda, T) \mathrm{d}\lambda}{\sigma T^4} \tag{2.5}$$

where I_s is the solar irradiation, $b(\lambda, T)$ is the spectral irradiance of a black body curve, and σ is the Stefan-Boltzmann constant (σ=5.6696x10^{-8} Wm^{-2}K^{-4}) [35].

There are various types of coatings and materials that have different temperature ranges and operating conditions based on their material composition. These types can be categorized as low ($T < 100$ °C), mid (100 °C $< T <$ 400 °C) and high temperature ($T > 400$ °C) coatings [35].

There are currently six distinct categories of selective absorber surface coating types as discussed by Kennedy (2002), which are a) intrinsic, b) semiconductor-metal tandems, c) multilayer absorbers, d) multi-dielectric composite coatings, e) textured surfaces, and f) selectively solar-transmitting coating on a blackbody-like absorber. These coating types are illustrated in Figure 2.9, and descriptions of each are given below.

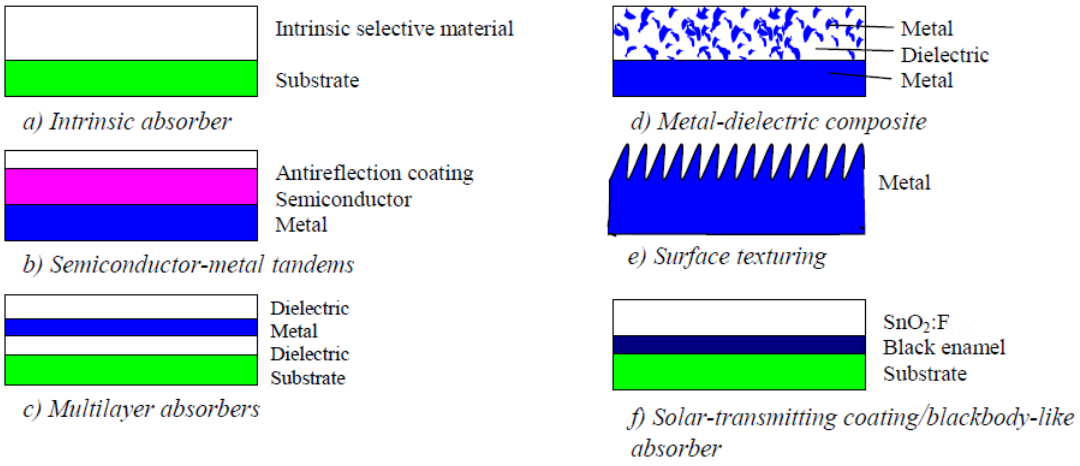

Figure 2.9: Types of coatings and surface treatments for selective solar energy absorption [35]

Intrinsic absorbers, also known as *mass absorbers*, are absorbers that have solar selectivity based on intrinsic properties of the material. These properties are found in transition metals and semiconductors, and after a large amount of modifications, they can be used as intrinsic absorbers. Because ideal intrinsic solar absorber materials do not exist, research on them has not been very productive historically. These materials are, however, finding an increased use as components in multilayer and composite coatings designed for high temperature usage [35].

Semiconductor-metal tandems are coatings that consist of a semiconductor layer, with bandgaps in the range of around ∼0.5 eV (2.5 µm) to 1.26 eV (1.0 µm), which absorb short-wavelength radiation, and an underlying metal layer which has a low emittance. The combination of these layers gives the solar selectivity desired by the coating. An anti-reflection coating is needed due to the high refractive indices of the useful semiconductors, which result in large reflective losses. The three semiconductor materials of interest for this type of coating are Si, Ge and PbS [35].

Multilayer absorbers or *multilayer interference stacks*, consist of multiple thin layers of dielectric and metal materials, allowing the coating to have both high absorption and low thermal emittance, and be stable at high temperatures. Metals that are commonly used in these coatings are Mo, Ag, Cu and Ni, and the dielectric layers commonly consist of either Al_2O_3, SiO_2, CeO_2 or ZnS [35].

Metal-dielectric composite coatings or *absorber-reflector tandems* are coatings which are highly absorbent in the solar region and transparent in the IR. These coatings are deposited onto metal substrates that are highly reflective in the IR region. The metal-dielectic composite consists of very fine metal particles in a dielectric or ceramic matrix. Another alternative is to have a porous oxide that has been impregnated with metal. These coatings are highly flexible, and by adjusting properties such as the thickness, particle concentration, size and shape, their solar selectivity can be optimized for a specific application [35].

Textured surfaces are surfaces that, if properly manufactured, have a micro/nano-scale surface structure that is able to absorb solar energy, while also appearing mirror-like and highly reflective to thermal energy. These surfaces are spectrally selective by using the optical trapping of solar energy. These surfaces are sensitive to the environment and require protection from contact, abrasion and dirt, all of which reduce the life span of the absorptive properties [35].

Selectively solar-transmitting coating on a blackbody-like absorber. These coatings can consist of a highly doped semiconductor such as SnO_2:F, SnO_2:Sb, In_2SO_3:Sn or ZnO:Al over an absorber with proven durability. Black enamel has been used before in low-temperature applications, and for high-temperature applications highly doped semiconductors can be used as the absorber material [35].

2.3 Small scale solar energy applications

In recent years, with the solar industry experiencing growth rates of over 60% annually [36], its applications have been broadened from purely energy generation to tasks that solve more specific issues. In agriculture there are several existing applications, such as cooking, crop drying, space and water heating and water pumping [37]. These systems are mostly based on utilizing PV systems or direct sunlight passively, and the use of CSP is relatively new in these kinds of smaller scale applications.

2.3.1 Solar cookers

In developing countries, it is estimated that over 2.5 billion people, which amounts to approximately 52% of population of these countries, are dependant on biomass as their primary fuel for cooking [38]. This percentage is greater in sub-Saharan Africa, where more than 90% of the rural populations rely on fuelwood and charcoal as a heat source [38]. These biomass fuels have been linked to several environmental impact and health issues, such as respiratory diseases, which cause over 4 million deaths per year due to inefficient use of solid fuels for cooking [39].

Solar cookers are an appealing alternative for cooking with biomass fuels, as only the sun is used as a heat source which produces no smoke. It is thus considered a clean way of cooking [40]. The use of solar cookers also has the added benefit of fuel and time saving, as well as energy security in areas where the supply is can be unreliable or non-existent [41]. As described by Muthusivagami et al. (2010), solar cookers can be classified into four types, namely the box, panel, collector, and concentrating solar cookers [42].

Box-type solar cookers are the most common type. They are generally constructed from an insulating material and a transparent medium, such as glass [43]. These cookers are able to gradually achieve temperatures of up to 70 °C to 140 °C in ideal solar conditions, depending on their design [44]. An example of a box-type solar cooker is given in Figure 2.10. These types of solar cookers are simple and stable, but they do, however, have a relatively low maximum temperature and take a significant amount of time to reach these temperatures.

Figure 2.11 shows a panel solar cooker, which is similar to the box cooker, except that it only has reflective panels instead of an insulated box. These are the most cost effective and easily constructed solar cookers, but have high heat losses and can be unstable in windy conditions [45].

Collector cookers, an example of which is shown in Figure 2.12, consist of both a flat plate collector and a cooker component. Reflecting mirrors can also be used around the collector to increase the solar energy captured. With these designs, the user is protected from the radiation, and the heat is transferred to the cooking component with a HTF, such as oil, which allows for higher temperatures to be reached [45]. These systems, although safe and convenient to use, are complicated to build and more expensive than box and panel cookers.

Figure 2.10: Box solar cooker

Figure 2.11: Panel solar cooker

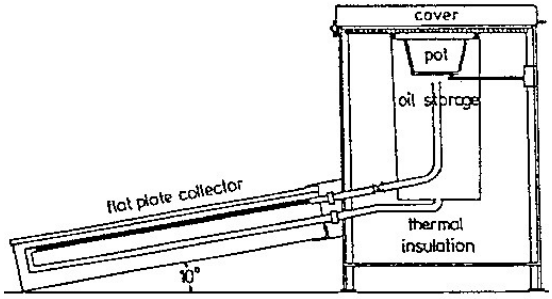

Figure 2.12: Flat plate collector solar cooker [46]

Concentrating solar cookers are able to achieve the highest temperatures and cook food faster than the other types of solar cookers [43]. These cookers make use of a parabolic shaped mirror to concentrate the solar energy onto a single focus point, where the energy can be utilized [47]. These shapes are mostly implemented in dish cookers, such as the one shown in Figure 2.13(a), but there are also several cooker models that make use of a parabolic trough technology, an example of which is shown in Figure 2.13(b). This system was designed by Yaholnitsky (2007) and works as an oven that is able to bake between 25-40 loaves of bread per day or roast various other foods [48].

(a) Parabolic dish cooker

(b) Parabolic trough cooker [48]

Figure 2.13: Concentrating solar cookers

2.4 Milk pasteurization

Pasteurisation is the process of heating foods for specified periods of time in order to destroy pathogens, and micro-organisms that can cause disease, which may be present in the foods. In the dairy industry, this process is used on milk to remove the potential pathogens without changing the original nutrients [6]. This section discusses the need for such a process, the necessary factors to consider when pasteurizing milk and the ways to check if the process has been successful.

2.4.1 Microbiological hazards in raw milk

As raw milk leaves the udder of a healthy and clean cow, it should be practically free of any bacteria. This condition is almost impossible to maintain and the surrounding environment can contaminate the milk almost instantly. This can occur in various ways, a few of which have been shown in Figure 2.14 [49]. The three main sources of contamination occur from within the udder, the exterior of the udder and from the equipment that is used to store and handle the milk [5].

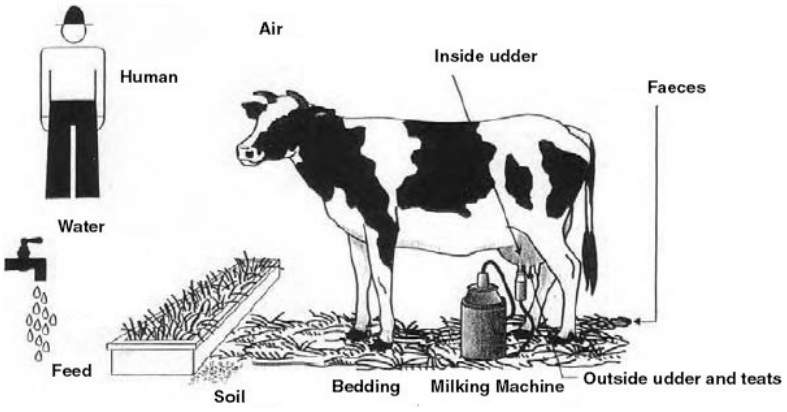

Figure 2.14: Milk contamination sources [50]

Pathogens that can contaminate the raw milk may originate from bacteria, fungus or other disease agents [51], and regardless of how the contamination occurs the most common way that these pathogens are transmitted to humans is through ingestion [5]. Some of the main health concerns for humans caused by the consumption of contaminated milk include Tuberculosis, Brucellosis, Q fever, Salmonellosis, Anthrax, E. coli and Staph Infections [52–55].

Tuberculosis and Brucellosis are among the most common illnesses that need to be addressed by the pasteurization of raw milk. Tuberculosis is a disease that, in 2015, was one of the top causes of death worldwide, with over 450000 cases reported in South Africa alone [56]. The bacterium found in milk which causes tuberculosis in humans is *Mycobacterium tuberculosis*, which is shown in Figure 2.15(a), using HR-SEM. Figure 2.15(b) shows a magnified image of the *Brucella abortus* bacteria, which is the cause of Brucellosis, a bacterial infection that has also been linked to the consumption of raw milk, which has over 500000 new cases reported worldwide each year [57].

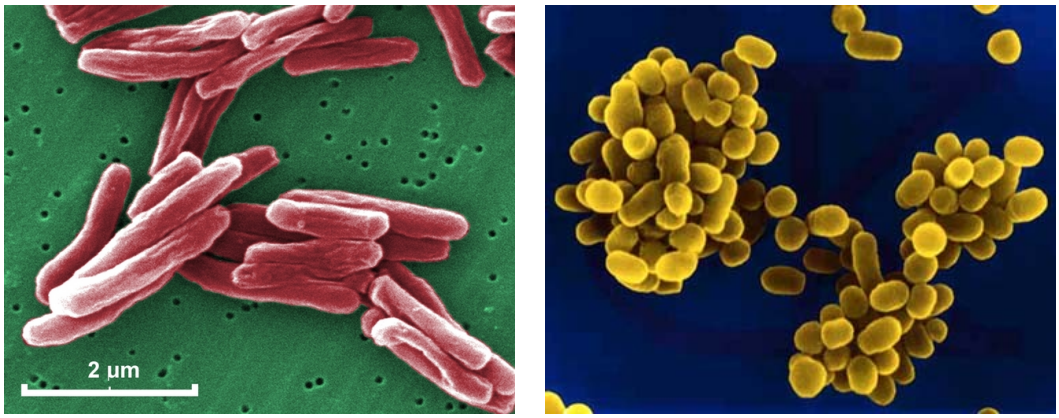

(a) *Mycobacterium tuberculosis* (b) *Brucella abortus*, Mag. 3900x at 35mm

Figure 2.15: HR-SEM images of bacteria

Coxiella burnetti is the bacterium which is known to be the cause of Q fever in humans and along with *M. tuberculosis* is one of the most heat resistant bacteria that could be present in raw milk [58]. Current pasteurization conditions have been designed to destroy these two organisms effectively [59]. By ensuring that these bacteria have been destroyed, or reduced to levels which do not pose health concerns, the assumption can be made that all bacteria with lower heat resistance have been removed, thus making it safe for consumption.There is also the added benefit that pasteurized milk is able to be stored for longer before it spoils, allowing for a reduction in wastage.

The bacteria that are present in milk can cause health concerns and illness when consumed by the general population. However, those with weaker immune systems, e.g. children, elderly people and pregnant women, are especially susceptible to the bacteria that are present in raw milk [60].

2.4.2 Milk pasteurization process

The process of heating milk in order to destroy bacteria was first developed in 1864 by Louis Pasteur. It has since been studied in depth, and standards have been developed to ensure that the necessary bacteria are correctly destroyed in the process [60]. Heat is lethal to all micro-organisms, and all different species have their own specific thermal resistances. During pasteurization, as well as other thermal destruction processes, the rate of destruction is logarithmic and is dependant on both the temperature and time at which the micro-organisms are held [61].

Table 2.1 shows the different temperatures and corresponding times at which raw milk must be held in order for pasteurization to be successful. These standards, as well as all other standards related to milk processes and procedures can be found in the *Grade "A" Pasteurised Milk Ordinance* (PMO) recommendations of the U.S. Public Health Service/Food and Drug Administration [62]. These regulations have been implemented in many states of the United States of America and are available to be adopted by many more countries, states and local health jurisdictions.

Table 2.1: Milk pasteurization standards [63]

Temperature (°C)	Holding Time
63	30 min
72	15 s
89	1.0 s
90	0.5 s
94	0.1 s
96	0.05 s
100	0.01 s

Alkaline phosphatase (ALP) is one of the many enzymes that is naturally present in milk, and is inactivated at temperatures marginally higher than the most heat-resistant pathogens that can be found in raw milk [6]. It plays no role in the storage properties of milk and is not a significant nutrient for people consuming the milk. The chemical testing for this enzyme can also be carried out easily, which makes it a good indicator of the effectiveness of the heat treatment procedure [64]. If significant activity of alkaline phosphatase is found, then it can be assumed that the pasteurized milk has either been contaminated with raw milk, or that the heat treatment was ineffective [61].

Figure 2.16 illustrates the thermal destruction curve of ALP in milk, which is shown to be very similar to the pasteurization standard of the U.K.. These curves are plotted on the same axis as the *M. tuberculosis* bacteria, which is also known as *tubercle bacillus*. These lines illustrates the temperature (x-axis) and time (y-axis) combinations that are required to meet the pasteurization standards of the U.K. and to destroy both *tubercle bacillus* and phosphatase.

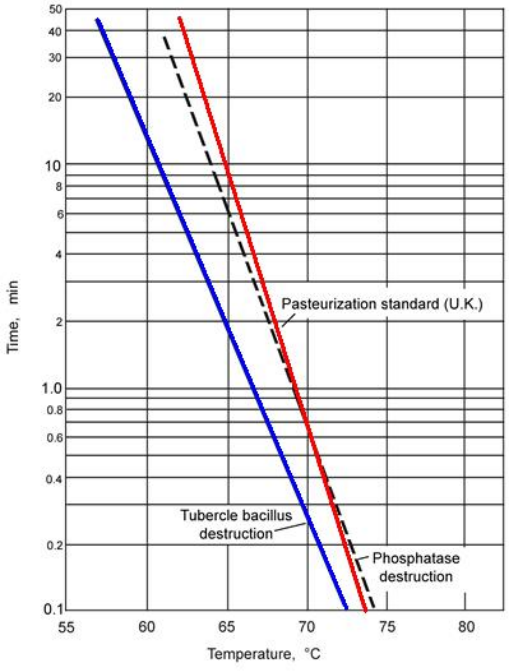

Figure 2.16: Milk pasteurization curve [64]

2.4.3 Testing of milk pasteurization

The regulations for milk and dairy products in South Africa were outlined by The Minister of Health in Section 15(1) of the Foodstuffs, Cosmetics and Disinfectants Act of 1972 [65]. These regulations state that raw milk with more than 50000 colony forming units (CFU) per 1ml may not be sold for consumption, and containing more than 200000 CFUs per ml may not be sold for any further processing. According to these regulations, it is also not permissible to sell pasteurized milk that contains more than 50000 CFUs per ml [66].

For both raw milk and pasteurized milk, sale for further processing or consumption is also prohibited if the tests for coliforms, *E. coli* and somatic cells indicate that the levels present are above the levels stipulated in the regulations relating to milk and dairy products in South Africa. It is also stated that milk can be classified as pasteurized if it passes the Aschaffenburg and Muller phosphatase test or any other test that is able to achieve the same accuracy of detecting ALP presence in milk [66].

The first methods used to determine the levels of ALP were colorimetric, which had a unit of measurement of micrograms of phenol per millilitre of milk [67]. The Sharer, Aschaffenburg & Mullen, and Rutger tests are examples of the colorimetric tests. These testing procedures are able to detect accuracies of around 0.1% of raw milk contamination (equivalent to 500 mU/L ALP) [68], and were the accepted public health standards from the 1950's through to the 1980's [67]. These testing procedures are still being implemented as the pasteurization testing standards in some countries, as is the case in South Africa.

More recently, however, with advances in technology, the acceptance level of both the European Union (EU) and the Food and Drug Administration (FDA) has been reduced from 500 mU/L ALP to 350 mU/L ALP [68]. This can be done using chemiluminescent procedures or a fluorometric method, which is more rapid, simple and sensitive than the previous testing methods [69]. The technology for these methods were developed in 1990's and have a detection limit of 0.003% [68]. ALP levels do vary based on different testing and processing conditions, and for milk processing plants it is advised for baselines to be determined, to which new samples can be compared [69].

2.4.3.1 Colorimetric testing

The earliest methods of testing for ALP in milk were based on reactions able to generate products that have certain colours, the first of which was done by Kay and Graham (1935). These tests involve the liberation of phenol from a disodium phenyl phosphate substrate, which then reacts with a colour forming reagent. This procedure initially required 19 to 24 h to complete, and had limited sensitivity [70]. Several other tests have been developed since then, using this method, which allow for reduced testing time and improved accuracy. These methods are discussed below.

Scharer Rapid Phosphatase Test. The Scharer rapid phosphatase test [71] was developed using the Kay and Graham (1935) method as a basis. The test gave a considerable reduction in analysis time, down to roughly 75 min. In this test, ALP cleaves a phosphate group from a disodium phenyl phosphate substrate, and after being

extracted with butanol, the released phenol group is reacted with 2,6-dichloroquinone-chlorimide to form a blue colour compound called indophenol [72]. Results of this test are expressed in micrograms of phenol per millilitre of milk, and an increased amount of ALP presence in the sample would result in an increased intensity of the blue colour. The output blue colour is read instrumentally using a spectrophotometer or by visual comparison against a set of standards [72].

Rutgers Phosphatase Test. This test was developed by Babson and Greely (1967) and follows almost the same procedure as Scharer's rapid test. Because the use of butanol in Sharer's test often produced an emulsion, which reduces the efficiency of phenol extraction [72], Babson and Greely (1967) substituted the original substrate with a phenolphthalein monophosphate substrate. This caused the ALP to release phenolphthalein instead, the concentration of which is determined with sodium hydroxide. Unlike the Sharer reagents, the products produced in this test are very stable over time and are easily stored [72].

Aschaffenburg and Mullen Test. This test is known to be slightly more sensitive than the Kay and Graham method, and does not require long incubation periods or an extraction step. The substrate used is ρ-nitrophenyl phosphate and the yellow colour that is developed is used as an indicator of the liberated nitrophenol [73].

2.4.3.2 Fluorometric and Chemiluminescent testing

Fluorometric methods involve the release of a phosphate radical from a substrate that is self-indicating, to form a product that is highly fluorescent [72]. Currently, for the testing of ALP in milk, a fluorogenic aromatic orthophosphoric monoester substrate is used [68]. A fluorescent compound known as "Fluoroyellow" is produced and then analysed using a fluorometer. The concentration of ALP is then correlated to the measurement of fluorescence generated over time [72].

The sensitivity of these methods is estimated to be 100-1000 times more sensitive than colorimetric methods, and significantly more rapid with reported times of $\sim$3 min [74]. Various aspects of the Fluorophos system have been compared to the Scharer and Aschaffenburg and Mullen colorimetric procedures for testing ALP levels in milk, and it has been reported that it has both high repeatability and precision while being both faster and simpler than the colorimetric alternatives [75].

Reports have determined that the sensitivity of fluorometric tests is in the range of 0.003 to 0.006% raw milk contamination or roughly 25 to 50 mU/L of ALP [76]. This is significantly better than that of the colorimetric methods which have sensitivity's that range from 0.1 to 0.5% [77].

Chemiluminescent tests are yet another way of measuring ALP activity in milk. They are based on ALP-mediated dephosphorylation of adamantyl 1,2-dioxetan substrates, which are cleaved by ALP to produce a phenoxide intermediate [72]. This intermediate then composes and produces a prolonged glow of light which can be measured using a refrigerated photon-counting device or luminometer [72]. Girrotti et al. (1994) was able to develop a chemiluminescent test for determining ALP levels in milk with a sensitivity and testing time similar to fluorescent methods. This test was able to obtain sufficient

results without the need for laborious solution and sample preparation [72].

Along with the fluorometric test, the Paslite chemiluminescent test, from Charm Sciences Inc., is another of the 3 testing procedures that is noted in the PMO as an acceptable means of testing for ALP in grade A milk products. The third is a rapid chemiluminescent method referred to as the Fast Alkaline Phosphatase test [78]. This test requires minimal sample size and preparation, and it is reported to have a response time of 45 s and a detection limit of 20 mU/L of ALP activity in pasteurized milk [72].

2.4.3.3 Biostrip Testing

There are several alternative testing methods which have also been developed to try combat some of the limitations of the technologies which are currently standard practice. These limitations can include price, accessibility and the use on different types of dairy products. Some of these testing methods include biostrip technologies, Electrochemical Assays, Immunochemical Assays and Polorographic Assays [72].

Biostrips have been developed to detect various chemical or biochemical parameters and have grown in popularity recently. Sharma et al. (2003) developed a biostrip test for ALP detection in milk, which produces an output dependant on the reaction between ALP and *p*-nitrophenyl phosphate in the presence of water. The reaction results in the liberation of *p*-nitrophenol and inorganic phosphate, the former of which reacts with a chromogen that turns the light-blue strip into green which is easily identified visually [72]. These tests have a sensitivity of >0.5 U/L and were developed for remote dairy industries where expensive testing facilities and equipment are not available, making them extremely useful alternatives for those in regions where more sophisticated tests are inaccessible [72].

2.4.4 Cleaning of milk pasteurizing equipment

It is important that milk intended for human consumption needs to be processed with equipment that maintains a high hygienic standard. To ensure that this is possible, the equipment that is used in the processing and pasteurization system needs to be cleaned and maintained on a continuous basis to prevent any contamination. It is important to ensure that the equipment maintains both its chemical and bacteriological cleanliness before and after any processing occurs [79]. This can be done by mechanical (manual) cleaning of the equipment with scrubbing brushes and detergent, or through more complex processes referred to as Cleaning-In-Place (CIP) systems, which clean the equipment internally without the need to dismantle any components.

When milk is heated to temperatures in excess of 60 °C, deposits of proteins, fats and calcium phosphates begin to form on the surfaces it comes in contact with. This is shown in Figure 2.17 and is known as milk fouling. Cold milk also leaves a thin film on the surfaces it comes into contact with which becomes harder to remove as it begins to dry out [79].

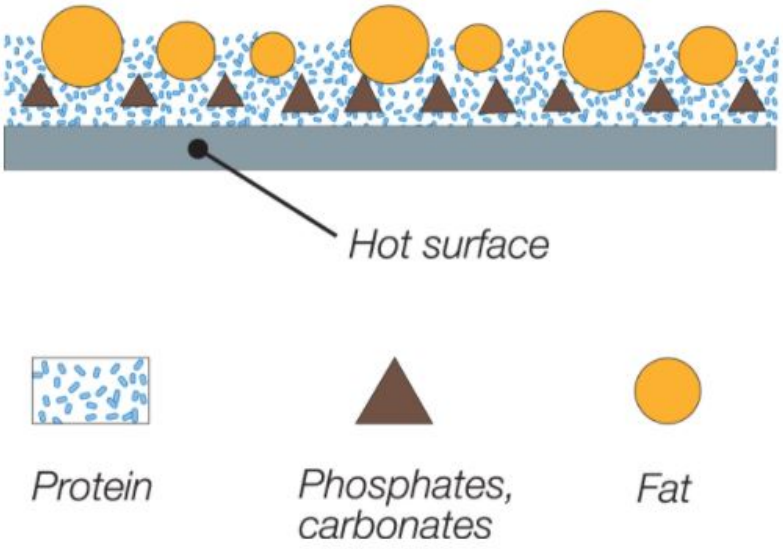

Figure 2.17: Milk deposits on a heated surface [79]

To remove the fouling and films that are left on the surfaces of the equipment after processing, as mentioned in the Dairy Processing Handbook by TetraPak (2018), a cleaning step that uses a detergent such as caustic soda (NaOH) and a step that includes an acidic solution such as Nitric Acid (HNO_3) are necessary. These cleaning products need to be circulated through the system at around 70 °C for a certain period of time to ensure that all solids and contaminants are removed from the equipment [79]. It is therefore crucial that the equipment used in milk processing be resistant to any chemicals which could be used in the cleaning process, as this may result in degradation that could further contaminate the milk.

2.5 Solar powered pasteurization

There are various different kinds of solar based devices that have been developed with the purpose of pasteurizing either milk or water. Using box or panel type solar cookers could be possible, but they can be slow to heat up. If there is insufficient solar energy during the day, the process may be unsuccessful. With these systems there is also only a very limited volume that can be processed per day. To ensure that the necessary high temperatures are reached in a short time frame, and to allow greater volumes to be processed, most systems are designed to incorporate either the flat plate collector or a type of parabolic concentrator [44, 80–82].

Zahira et al. (2009) were able to successfully pasteurize milk using a box type solar cooker. Their design was constructed from shipping cardboard, aluminium foil, a glass window and had inside dimensions of 52.5×24×36 cm. The achievable temperatures ranged from 65 °C to 75 °C and the time taken to reach these temperatures was up to 3 hours, because no concentration was used. This is illustrated in Figure 2.18, which shows the relationship of temperature vs. time on one of the testing days [83].

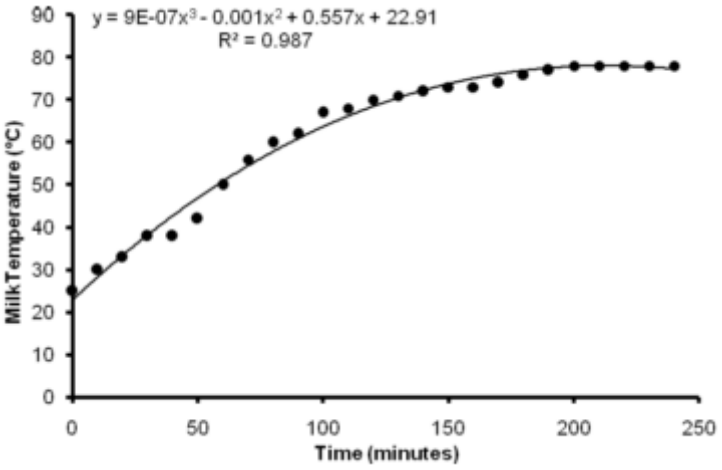

Figure 2.18: Box pasteurizer, milk temperature vs. time [83]

This box-type device shows that pasteurization is possible using even the most simple of methods. However, with the incorporation of some form of solar concentration, the time required to reach the necessary temperature could have been significantly reduced, which would have allowed greater quantities of milk to be pasteurized. This device would only be able to pasteurize small quantities of milk per day, and could potentially experience issues reaching the necessary temperatures on days when solar radiation is limited.

Franco et al. (2007) developed a concentrating dish cooker for pasteurizing goat milk in northern Argentina. The system used a parabolic style concentrator, shown in Figure 2.19, to heat water at its focus point, which was then circulated around a separate cooking container inside which the milk was held. This design was able to achieve the necessary temperatures (63 °C) for batch pasteurisation of 8l of milk in around 75 min [80].

Figure 2.19: Dish concentrator for goat milk pasteurization [80]

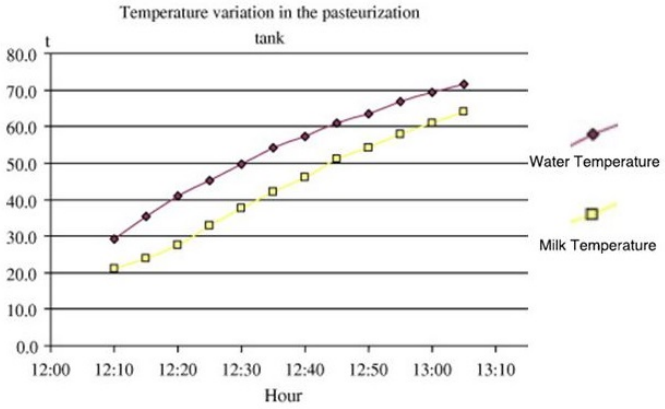

Figure 2.20: Dish concentrator, temperature vs. time [80]

Figure 2.20 illustrates the increasing temperature of the heating water and the goat milk that is being pasteurized during an experimental test of the system. This device had no automatic tracking system, and despite the need to be manually adjusted at constant time intervals, it was able to generate the necessary temperatures. This device was designed to pasteurize a single batch of milk, and the substitution of a pasteurized batch for a new batch could be potentially dangerous due to the high temperature of the water from which the milk container needs to be removed. This type of batch processing could also place a limit on the potential output of the system per day.

Wayua et al. (2013) developed a flat plate solar collector device, shown in Figure 2.21, as a means of pasteurizing milk. This design consisted of a commercial solar collector and an 80 l pasteurization vat. The tank was, however, not intended to be completely filled, and when tests were conducted with 70 l of milk, the maximum temperature reached was only 41.7 °C.

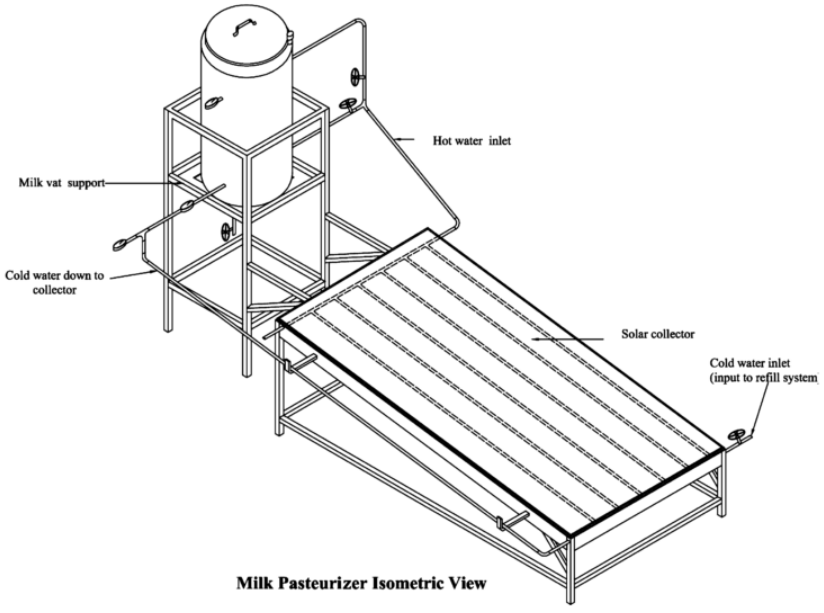

Figure 2.21: Isometric view of flat plate solar pasteurizer [81]

Figure 2.22 illustrates the results obtained for the testing of the flat plate solar pasteurizer of Wayua et al. (2013) in Marsabit, Kenya. The optimal milk volume inside the tank was found to be 40 l, and excluding the initial time needed for heating the water, the system took around 1.5 h to reach 69.7 °C, which is high enough to pasteurize the milk. These results were obtained on days with an average solar insolation of 783.7 W/m^2 and ambient temperatures of 30 °C. The average difference between the water and milk temperature was roughly 8.1 °C, and when the volume of milk used was reduced to 20 l, a maximum temperature of 81.4 °C was possible [81]. This design proved to be adequate for pasteurizing milk in batches under very favourable solar conditions, however when the solar energy is limited, the system may encounter some problems with reaching the necessary temperatures.

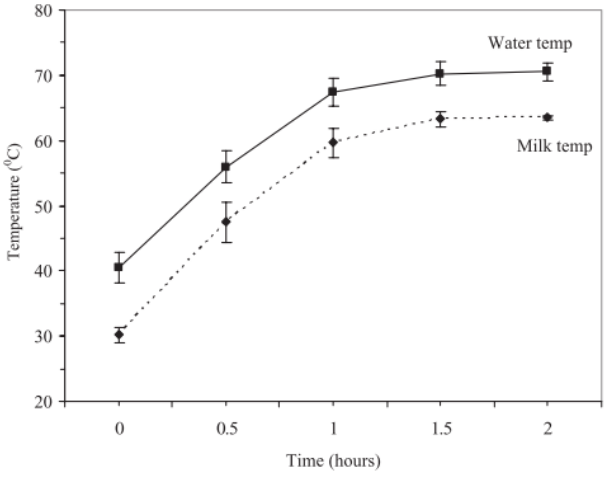

Figure 2.22: Flat plate solar pasteurizer, temperature vs. time [81]

Al-Soud et al. (2010) developed and tested a solar cooker that made use of a parabolic trough with two axis tracking system to follow the sun's position. The trough was only 100 cm long with a collector tube diameter of 10 cm. Despite their study being focused on the development of the tracking system, the results, which are shown in Figure 2.23, showed that the cooker was able to achieve a maximum water temperature of 90 °C on summer day where the ambient temperature reached 36 °C [84]. Although no such tests were conducted, this temperature would be sufficient for the thermal pasteurization of milk and water. The receiver tube of this system was not, however, designed for continuous flow, and the liquid inside the tube needs to be manually poured in, and drained after heating is completed, a process which can result various other problems and inefficiencies.

The results shown in Figure 2.23, were obtained on three different days of testing where the global solar radiation reached peaks of roughly 4.45, 4.75 and 5 kWh/m^2 respectively [84]. The solar radiation was monitored throughout the days of testing, and is plotted on Figure 2.24. This device shows that the use of a parabolic trough, even one that is relatively small in size, is able to produce the temperatures that would allow for milk pasteurization. Because the design is so small and does not allow for continuous flow of liquid through the system, it is only able to process a very limited amount of

liquid per day, making it an impractical solution. It does, however, illustrate that the use of parabolic troughs for heating liquid can be a viable solution.

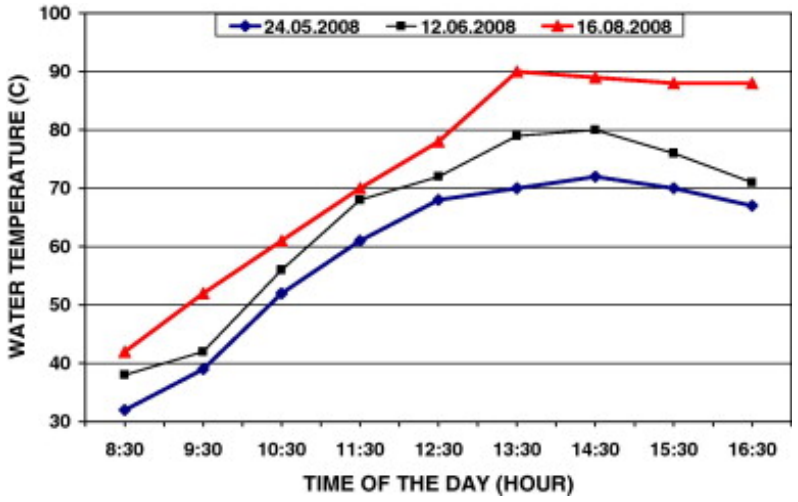

Figure 2.23: Small parabolic trough, temperature vs. time [84]

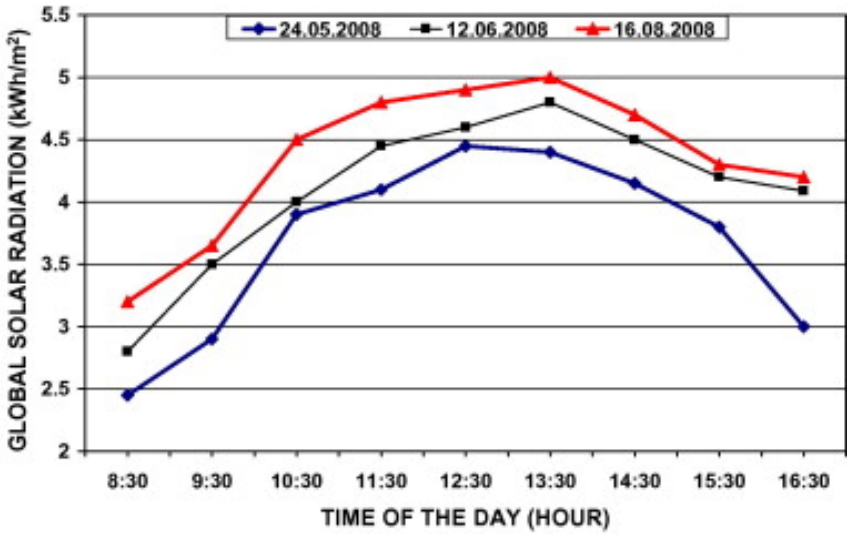

Figure 2.24: Small parabolic trough, test day irradiation [84]

Sonune and Philip (2003) developed a circular Fresnel type solar concentrator with an aperture area of 1.5 m^2, shown in Figure 2.25(a). The reflector material used in this design was buffed stainless steel, which performed well enough for this application with a reflectivity of around 78%. Their design incorporated a manual tracking system and was able to heat 1 l of water to 90 °C in around 20 minutes. The results of this test are plotted in Figure 2.25(b). The average DNI during the testing was around 700 W/m^2 with an ambient temperature of roughly 32 °C. This system was able to conveniently perform cooking and heating that would not be normally possible with a box-type solar cooker [85].

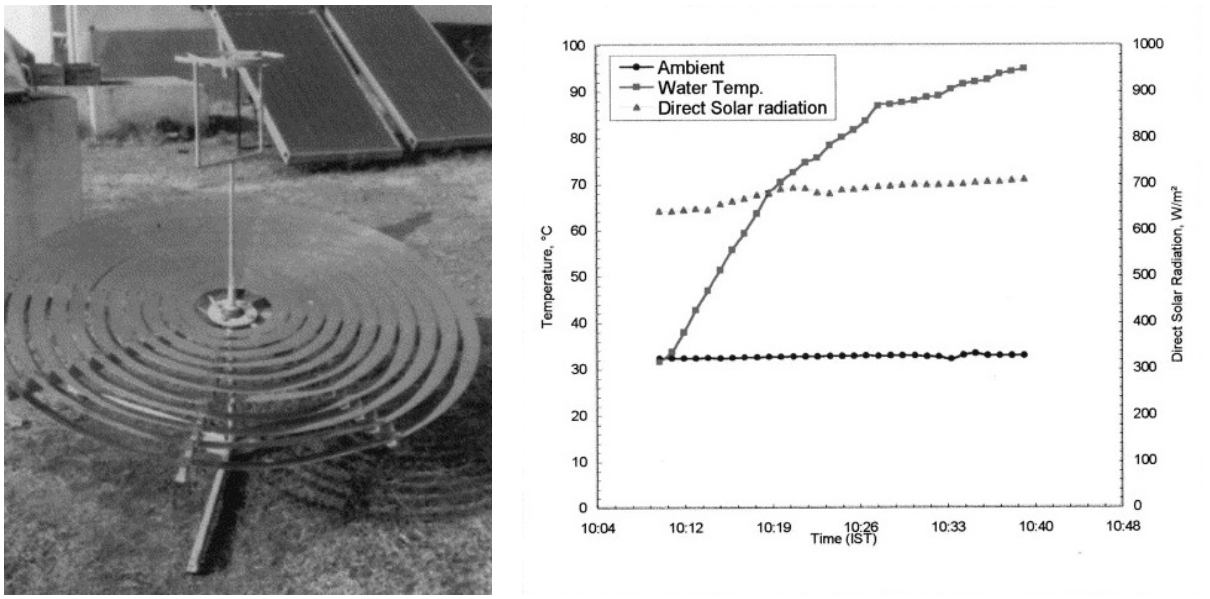

(a) Device (b) Performance

Figure 2.25: Sonune circular Fresnel reflector [85]

2.6 Design motivation

The aim of this thesis is to develop a prototype small scale system that uses CSP, and is able to pasteurize milk for people in rural areas. The system will utilize parabolic trough technology, and at the time of writing, this specific technology, which will incorporate continuous flow pasteurization, has not yet been used for application of this nature. A working system such as this could yield remarkable benefits for those in rural areas that are given access to it, allowing them to process milk, making it free of harmful bacteria and increasing its lifespan. Using solar energy for the heating process instead of electricity or biomass fuels will also allow the users to save costs consistently over the long term, and reduce any negative health and environmental impacts that are related to these sources.

By utilising the concentration of a parabolic trough systems, the solar pasteurizer will be able to continually heat and pasteurize milk that has a consistent flow. This will allow the system to process larger quantities of milk per day than other types of solar cookers that do not incorporate concentration. The system will thus aim at reaching temperatures of over 72 °C, which will allow for continuous flow pasteurization of the raw milk to take place.

In order to make the design practical, it must be made as simple as possible and incorporate low cost and readily available materials to a great extent. This is important, especially for components that are generally more expensive and are crucial to the systems performance, such as the reflector sheet and receiver tube coating. By doing so, if components are damaged or become degraded during operation, replacements can be easily sourced and installed, whereas if specialised components and materials are used, then this process becomes much more complex and expensive.

The system will also aim to facilitate the easy replacement of components that are most likely to degrade, i.e. the reflector and receiver tube coating. By designing the system with easily replaceable components, it will also allow for design optimisation during testing. Both of these components can be replaced with materials of different costs and optical properties, allowing for the system to be tested under different conditions. It is important that the prototype device is designed to be rigid, strong and able to maintain the necessary parabolic shape, which will be needed to test the viability of this type of system and will also allow for alternative tests to be run on the device at a later stage.

2.7 Chapter summary

This chapter covered the background information that is relevant to the different aspects of this project. Insights were given into solar energy as well as different CSP systems and some of their components. Existing solar cookers and pasteurizing devices were also discussed, showing that these devices are possible and can be of great use to people that have access them. The pasteurization of milk was also covered along with its benefits and the necessary steps in this process. Finally, a motivation for the design of CSP milk pasteurization system was given, which discussed why a small scale system such as this will be beneficial for those in need, and the key factors that would need to considered.

Chapter 3

Parabolic Trough Design

The introduction and literature review chapters presented a preface of this thesis and a detailed outline of the theory on which this project is based. This chapter highlights the design decisions that were made, taking into account the necessary theoretical aspects of designing such a system, as well as the equipment available at Stellenbosch University, iThemba Labs and through accessible partners.

3.1 Parabolic trough geometry and optics

The design of CSP technologies such as parabolic troughs and dishes are dependant on the geometrical properties of parabolas, which allow solar energy to be concentrated at specific locations where it can then be harnessed. The performance of these systems rely on their ability to collect solar energy and convert it into useful energy while experiencing minimal losses. The energy balance, given in Stine and Geyer (2001), can be written as

$$\dot{Q}_u = E_{optical} - \dot{Q}_{loss} \qquad \text{(W)} \tag{3.1}$$

where $\dot{Q}_u$ is the rate of useful energy the system is able to produce, $E_{optical}$ is the optical radiation incident on the receiver and $\dot{Q}_{loss}$ is the rate of thermal energy being lost by the system [86]. In the case of parabolic troughs, the useful energy is that which can be transferred to the HTF that flows through the receiver tube. The amount of heat that is added to this fluid can be represented by

$$\dot{Q}_u = \dot{m} c_p (T_{out} - T_{in}) \qquad \text{(W)} \tag{3.2}$$

where $\dot{m}$ is the mass flow rate of the HTF, c_p is it's specific heat, and T_{out} and T_{in} are the outlet and inlet temperatures of the fluid respectively [86]. These two equations are the governing equations of solar concentrators. The following sub-sections discuss the design and layout of parabolic systems in order to maximize the useful energy they can produce.

3.1.1 Overview of the parabola

A parabola, as described by Stine and Geyer (2001), is the locus of a point that moves such that its distances from a fixed line, referred to as the directrix, and a fixed point, or focus F, are equal. This is illustrated in Figure 3.1, where lengths FR and DR are known to be equidistant. The axis of the parabola, which in this figure forms the horizontal axis, is the axis that is perpendicular to the directrix and passes through the

focus. The point where the parabola intersects its axis is the vertex, denoted by V, which is midway between the directrix and the focus [86].

The standard equation of a parabola that is orientated as shown in Figure 3.1 would be

$$x = ay^2 + by + c \tag{3.3}$$

where a,b and c are constants and the horizontal axis is the x-axis.

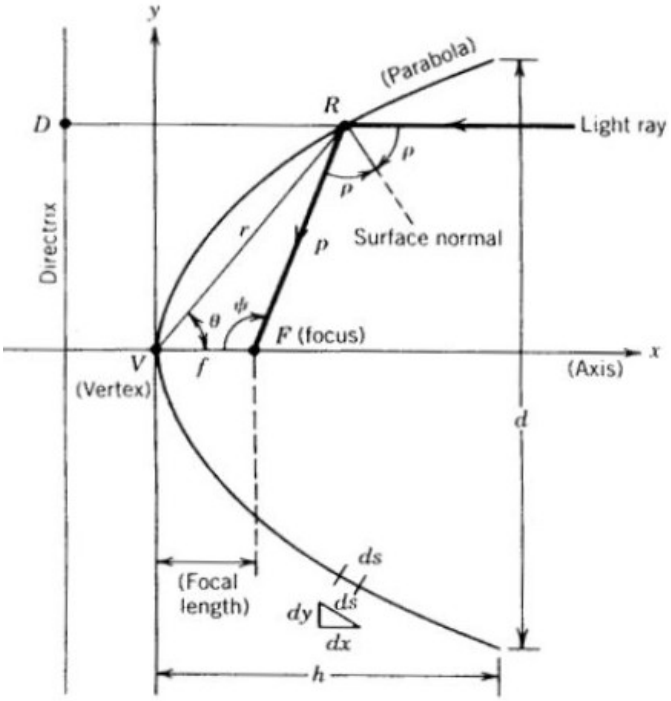

Figure 3.1: Important features of a parabola [86]

As per the definition of the focal point of a parabola, all incoming rays that are parallel to the axis of the parabola will be reflected through its focal point. If we assume that the parabola is correctly aligned and solar energy arrives at the parabolic surface as parallel rays, then by applying Snell's law, which states that the angle of reflection equals the angle of incidence, the focal point can be found as the ideal location for a receiver tube when considering CSP [87]. This concept has been illustrated in Figure 3.1, where the light ray is reflected off the parabola to the focal point of the parabola F.

3.1.2 Parameters that determine parabolic trough geometry

Parabolas that are used in solar applications have finite heights and widths and cover a specified surface area. In the design of these parabolic troughs there are four geometric parameters, as highlighted by Günther et al. (n.d.), that determine the form and size of different parabolic troughs, these parameters are the: trough length, focal length, aperture width and the rim angle [88].

The length of the trough is the longitudinal distance over which the parabolic shape is extended. The focal length f, is the distance between the vertex and the focal point of

the parabola, which is illustrated as the length VF in Figure 3.1. This length determines the overall shape and size of the parabola. Its effect can be seen in Figure 3.2, where larger focal lengths result in flatter parabolic shapes [88].

The aperture width a, is the distance from one rim of the parabolic shape to the other, as shown in Figure 3.2. The rim angle, ψ, is the angle between the axis of the parabola and the line from its focal point to the rim. Parabolas that have the same rim angle will have cross-sections that are geometrically similar. Figure 3.2 illustrates the relationship between the focal length and rim angle of parabolas with a common focal point and aperture width. Parabolas that have large rim angles will have a deep and narrow shape as is shown with parabola 1, whereas with a small rim angle such as ψ_4, the resulting parabola will have a much flatter shape.

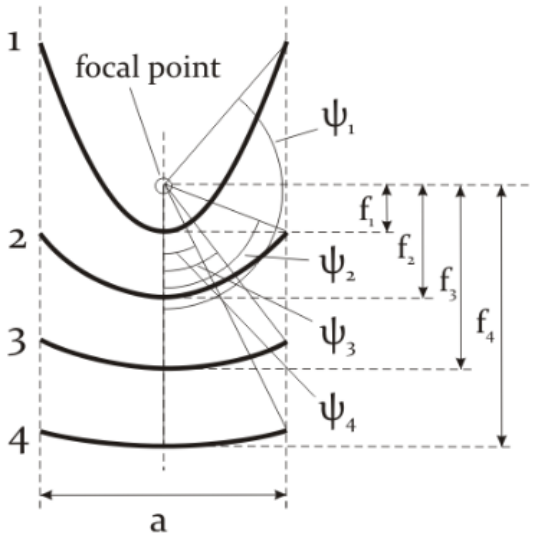

Figure 3.2: Parabolas with a common focal point and aperture width [88]

The height of a parabola, h, is defined as the distance from the vertex of the parabola, to a line drawn across its aperture. This parameter is important when designing a parabolic trough, and is also used in the calculations of other parameters. This can be given in terms of the aperture width and focal length of the parabola by

$$h = \frac{a^2}{16f}. \tag{3.4}$$

The rim angle ψ can also be determined in terms of the aperture width and focal length using [86]

$$\tan\psi = \frac{1}{(a/8h) - (2h/a)}. \tag{3.5}$$

When designing a parabolic trough, where the primary goal is reflecting solar energy onto a central receiver tube, there are two primary design considerations that determine the conditions under which it will be able to operate, and the amount of energy that can ultimately be harnessed. These are known as the concentration ratio and the aperture area of the system.

The aperture area, A_a, of the trough is the product of the length of the trough l, and the aperture width, given as

$$A_a = l \times a. \tag{3.6}$$

This area determines the total horizontal surface area that is covered by the trough, and subsequently, the amount of solar energy that can be harnessed and concentrated [88]. The concentration ratio, C_g, is used to help determine what the expected performance of the system would be and the conditions it will likely experience. It is defined as the area of the collector aperture in relation to the receiver surface area, and can be represented by

$$C_g = \frac{a \times l}{\pi \times d_o \times l} = \frac{a}{\pi \times d_o} \tag{3.7}$$

where the receiver surface area is the total surface area of the receiver tube with diameter d_o and length l [88]. This is an important variable when calculating expected temperatures and the output of the system under different solar conditions.

3.1.3 Parabolic optics

Parabolic mirrors are designed to reflect all rays that are parallel to their axis of symmetry onto a single point, as illustrated in Figure 3.3. This does, however, require the parabolic mirror to be aligned such that it faces the sun directly.

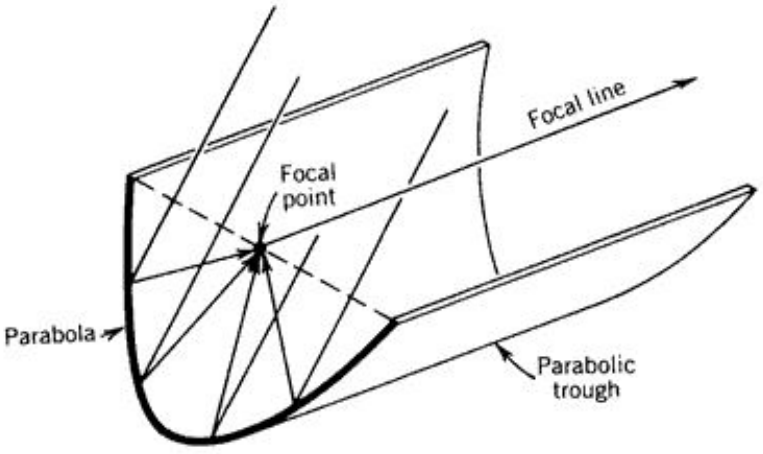

Figure 3.3: Parabolic trough focal point and focal line

As solar rays become offset from the axis of symmetry of the parabola, beam dispersion begins to occur and the focal point begins to spread. This is shown in Figure 3.4(a) and 3.4(b), where the effects of a 1° tilt on the focal point can be seen relative to the focal point when rays are normal. Therefore, in order for a parabolic concentrator to run as efficiently as possible, it needs to rotate during the day, by using either a tracking system or manual adjustment, to ensure that all possible solar energy is reflected correctly onto the focal point [86].

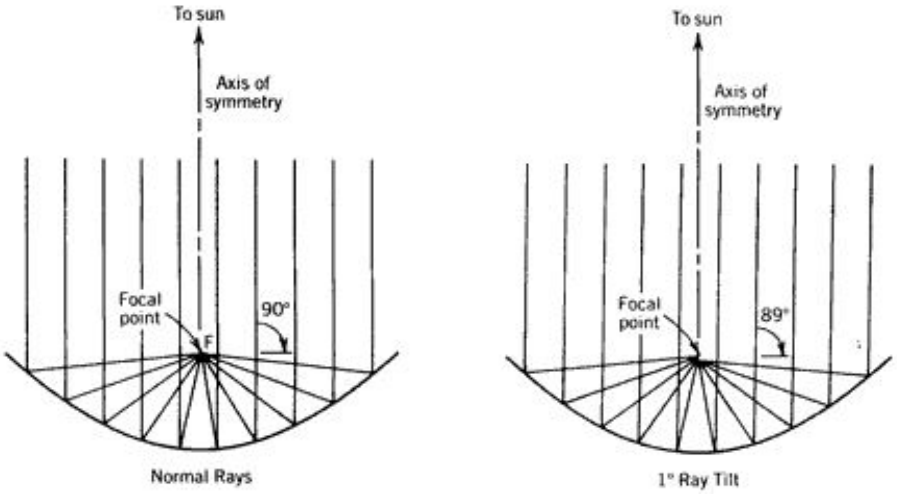

(a) (b)

Figure 3.4: Effect of misalignment on parabolic optics [86]

To simplify the explanation of solar rays, Figures 3.1, 3.3 and 3.4 have illustrated the incident light rays coming from the sun as perfectly parallel individual rays. However, this is not entirely accurate. In reality, the size of the sun causes the light rays to arrive on earth within a certain range of being perfectly normal. The fixed angular size of the sun's disc, as experienced on Earth, is approximately 33 minutes of an arc or 0.55°. This causes the light to travel and be reflected by the parabola within the same angular range. This means that instead of the all the sunlight being focused as a direct beam, it is reflected as a disk, illustrated in Figure 3.5. It is important that the absorber tube be designed to be larger than this disk, so that, if the system is correctly aligned, none of the directly reflected rays will miss the receiver tube.

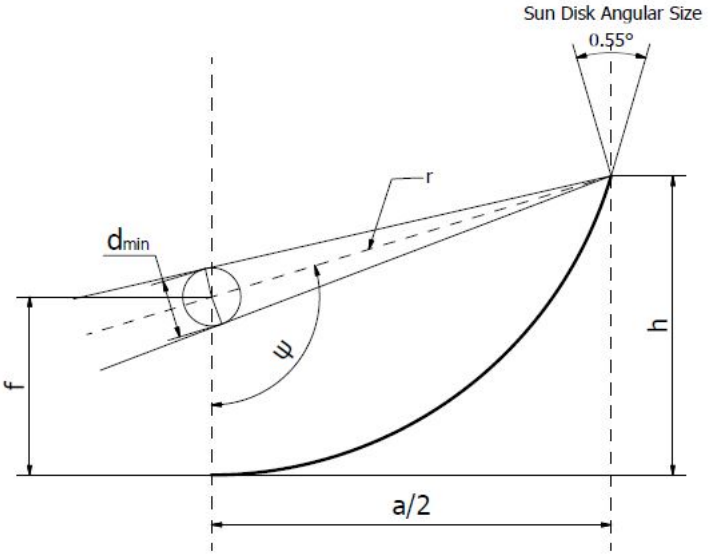

Figure 3.5: Angular size of sun disk relative to parabolic trough

The diameter of this disk, d_{min}, which is discussed further in Appendix A, determines the minimum size of a sphere that is able to intercept all of the solar beams being reflected by the parabola, assumed to have negligible optical errors and be properly aligned to receive sunlight at the normal position. Pih & Kalogirou (1997) expressed this property as [89]

$$\frac{d_{min}}{2} = \frac{a}{2\sin\psi}\sin(\frac{0.55}{2}). \tag{3.8}$$

3.1.4 Collector efficiency

The collector efficiency, η_{col}, of a parabolic trough describes its performance. This is dependant on the rate of useful energy that the system is able to produce, and the total amount of solar energy that falls on the aperture area of the system [90]. The simplified ratio is given as

$$\eta_{col} = \frac{\dot{Q}_u}{A_a I_s} = \frac{\dot{m} c_p (T_{out} - T_{in})}{A_a I_s} \tag{3.9}$$

where $\dot{m}$ is the mass flow rate of the heat transfer fluid, and T_{out} and T_{in} are the outlet and inlet temperatures of the fluid respectively [90].

The following subsection describes the optical and thermal losses which cause reductions in the overall efficiency of the system.

3.1.4.1 Optical and thermal losses

The optical efficiency, η_o, of a solar collecting system describes the ratio of solar energy that falls on the receiver tube relative to that which falls on the reflector surface of the system. This ratio is commonly represented by [91]

$$\eta_o = \rho\tau\alpha\gamma(1 - A_f \tan\theta\cos\theta) \tag{3.10}$$

where

ρ = Reflectance of the parabolic reflecting surface
τ = Glass cover transmittance
α = Absorptance of the receiver
γ = Intercept factor
θ = Angle of incidence
A_f = Geometric factor

The geometric factor, A_f, is determined by the collector's geometry and accounts for any abnormal effects on the solar concentration such as blockages, shadows and losses where energy is reflected beyond the end of the receiver, which is know as the *end effect*. Taking into account all effects, the geometric factor can be given as the ratio of lost area to the total aperture area of the collector [92]

$$A_f = \frac{A_l}{A_a} \tag{3.11}$$

where A_l is the total loss in aperture area, for which equations can be found in Kalogirou [92]. Assuming that the system will be correctly aligned with the solar rays during experimental testing, and that any shade over its surface can be neglected, this factor

can be approximated to equal 1, i.e. $A_f \approx 1$. This also allows us to approximate $\theta \approx 0$, because the angle of incidence is assumed to be normal to the collector. The expression for optical efficiency is thereby reduced to give

$$\eta_o = \rho\tau\alpha\gamma. \tag{3.12}$$

The intercept factor, γ, is the most complex parameter to be calculated when determining the optical efficiency. It is the ratio of the energy that is intercepted by the receiver tube to the energy reflected by the parabola, taking into account the receiver size, surface angle errors of the parabola mirror and the spread of solar beams [92]. It requires highly accurate experimental set-ups designed to measure these errors and accurately calculate the factor. The intercept factor incorporates both random and non-random errors, several of which are illustrated in Figure 3.6 [92].

Non-random errors are those that occur in manufacturing, assembly or during operation of the collector. Examples of these are misalignment errors of a certain angle (β) between the solar rays and axis of the parabola, and an incorrectly located receiver, which is a certain distance (d_r) from the focus, or imperfections in the parabolic profile [92].

Random errors are those that are truly random, such as changes in the sun's width, σ_{sun}, scattering due to random slope errors, σ_{slope}, or scattering caused by the reflective surface, σ_{mirror}. These can be modelled statistically at normal incidence, by determining the standard deviation of the total reflected energy distribution, which is given as [93]

$$\sigma = \sqrt{\sigma_{sun}^2 + 4\sigma_{slope}^2 + \sigma_{mirror}^2}. \tag{3.13}$$

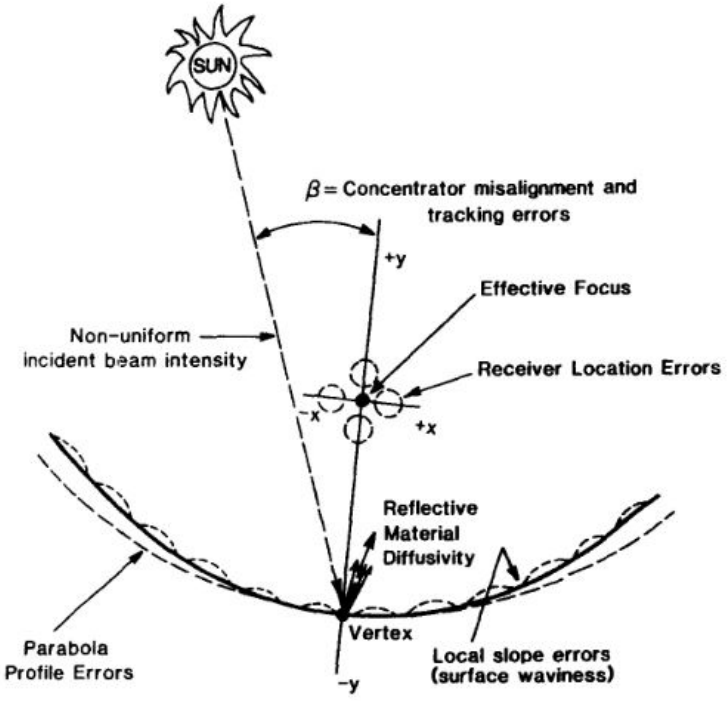

Figure 3.6: Potential optical errors in parabolic trough collectors [93]

When solar radiation is concentrated onto the receiver tube of a parabolic trough, a large portion of the energy will ideally be absorbed and transferred to the HTF, where it becomes useful energy. However, heat transfer to the environment through various modes is also inevitable, as is the case with all thermal systems. Thermal losses of the system need to account for all conductive, convective and radiative losses that occur in the system [92]. It is therefore necessary to determine expressions for the loss coefficient, U_L, and the collector heat removal factor, F_R. The heat removal factor describes the ability of the system to internally remove the heat that is absorbed. This factor is greatly dependant on the mass flow rate and thermal conductivity of the HTF being used, as well as the thermal conductivity of the receiver tube material [92]. The loss coefficient is representative of the thermal losses that the system experiences during operation. To simplify this coefficient, assuming there is no temperature gradient along a bare receiver tube, the loss coefficient can is given as [92]

$$U_L = h_w + h_r + h_c \tag{3.14}$$

where h_w is the wind loss (or convection) coefficient, h_r is the radiation coefficient and h_c is the conduction coefficient. To estimate the conductive losses of the system, the collectors support system needs to be analysed, and losses through the structure need to be calculated. Kalogirou (2014) gives an expression for the linearised radiation coefficient as [92]

$$h_r = 4\sigma\varepsilon T_r^3 \tag{3.15}$$

where T_r is the temperature of the receiver tube, ε is the emissivity of the surface, which would be dependant on the coating that is applied to it, and σ is the Stefan-Boltzmann constant. Kalogirou (2014) goes on to summarize the overall efficiency of a collector system as a combination of the losses from thermal and optical components as

$$\eta = F_R\left[\eta_o - U_L\left(\frac{T_{in} - T_a}{I_s C_g}\right)\right] \tag{3.16}$$

where C_g is the geometric concentration ratio (3.7).

3.2 Design and construction

The purpose of this system was to heat a HTF, milk in this case, to a temperature at which pasteurization will occur. The minimum temperature that was being targeted by the system was therefore 72 °C. It was, however, designed to be able to withstand temperatures well above this, to ensure it can be useful for other potential applications. Because pasteurization of milk at 72 °C requires holding it at that temperature for 15 seconds, the device will need to aim for a temperature of roughly 75-77 °C to ensure that there is sufficient time for pasteurization to occur. This and other general calculations, using different flow rates and solar conditions to estimate the output conditions of system, are given in Appendix A.

The key ideas that were kept in mind during the design of this parabolic trough were ease of operation, overall weight of the system, cost, and the use of long-lasting, readily available parts that can be simply replaced if necessary. All system components that came into contact with the HTF needed to be able to withstand the temperatures that could be reached. These components also needed to be safe to use with food products

intended for human consumption, and be unreactive to any chemicals used in the cleaning processes.

Another key design feature of the system, because it could have many potential uses, is that it needed to facilitate the testing of various different replaceable components. For this reason, the receiver tube and reflective sheet were designed to be replaceable, so that alternative materials could easily be tested in future. To ensure that the system's performance was robust and that it could function with different materials, the system performance was tested with 3 different receiver tube coatings, two of which are readily available and low cost, i.e. candle soot and black spray paint, and one which was a more specialized selective solar absorber. The reflective sheet that was used in the system also utilized an easily accessible material, and was made from a polished stainless steel sheet instead of the commercial reflective sheets that are more expensive and would be hard to replace if damaged.

The system, which is shown in Figure 3.7, consists of two main sub-assemblies i.e. the support frame and the rotating body, and several smaller components, such as the receiver tube, pump system, thermocouples and sun aiming pin. To ensure that the device was simple to operate, and that potential problems could be minimized, the system did not incorporate an automatic tracking system, and instead relied on manual adjustment during the day to ensure it was correctly aligned. An alternative to manual tracking would be the inclusion of an automatic tracking system comprising of several small sensors and a small motor to facilitate the rotation, all of which would not come to an infeasible cost for this application. A system such as this would allow the device to be left unattended for longer periods of time while accurately following the sun, and could significantly reduce the amount of time and effort that needs to be input by the operator. However, because the flow rate and the output temperature of the fluid were designed to be monitored and controlled manually with this system, to ensure that temperatures were safely above the temperature threshold needed for pasteurization, a tracking system such as this was not included in this design.

Appendix B contains CAD drawings of the main sub-assemblies and components of the milk pasteurizing device and Appendix C contains the necessary steps and procedures for set-up, operation and the replacement of device components.

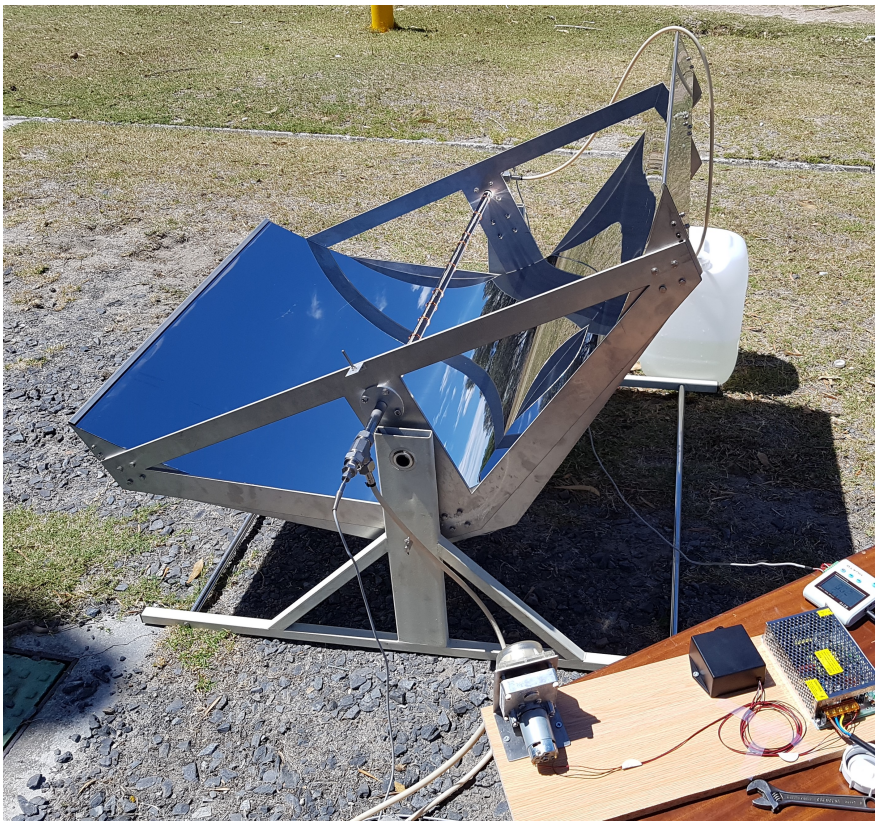

Figure 3.7: Parabolic trough full assembly

3.2.1 Parameters of the parabolic trough

The key parameters of the parabolic trough system are summarized in Table 3.1. These were chosen to maximize the potential output of the system, while still keeping the system on a scale small enough to allow it to be operated and moved by one or two people. Calculations used to determine some of these properties can be found in Appendix A.

Table 3.1: Parabolic trough parameters

Parameter	Nomenclature	Value
Trough length	l	1 m
Aperture width	a	1.2 m
Aperture area	A_a	1.2 m^2
Parabola height	h	0.4 m
Focal length	f	0.225 m
Rim angle	ψ	106.2602°
Receiver diameter	d_o	19.05 mm
Concentration ratio	C_g	20.051

The following subsections describe the different parts and components that make up the sub-assemblies and the system as a whole.

3.2.2 Frame and rotating body

The two main sub-assemblies of the parabolic trough are the support frame, and the rotating body. The purpose of the support frame is to hold the rotating body and allow it to rotate and be adjusted as necessary throughout the day. The two assemblies are joined along the axis of rotation, as indicated in Figure 3.8, where a brass bush allows for smooth rotation without the need for a bearing.

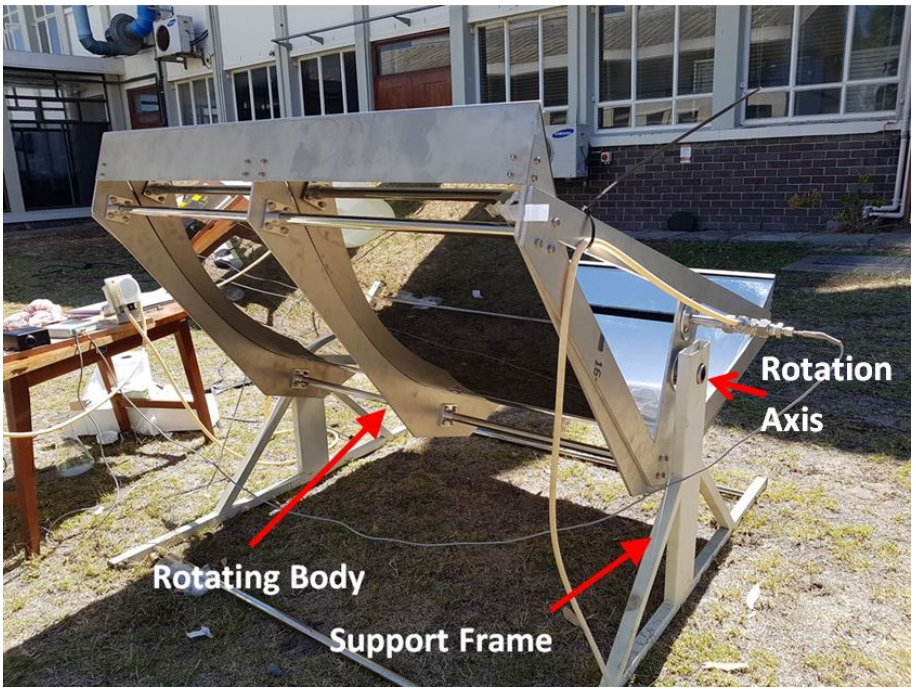

Figure 3.8: Parabolic trough rotating body and support frame

The key components of the rotating body are the ribs, identified in Figure 3.9. These ribs have a parabolic profile, which was produced by using a water jet machine, and are responsible for giving the reflective sheet its parabolic form. The reflective sheet is forced into this shape, and then held in place on the ribs with clips that run along both rims of the parabolic trough.

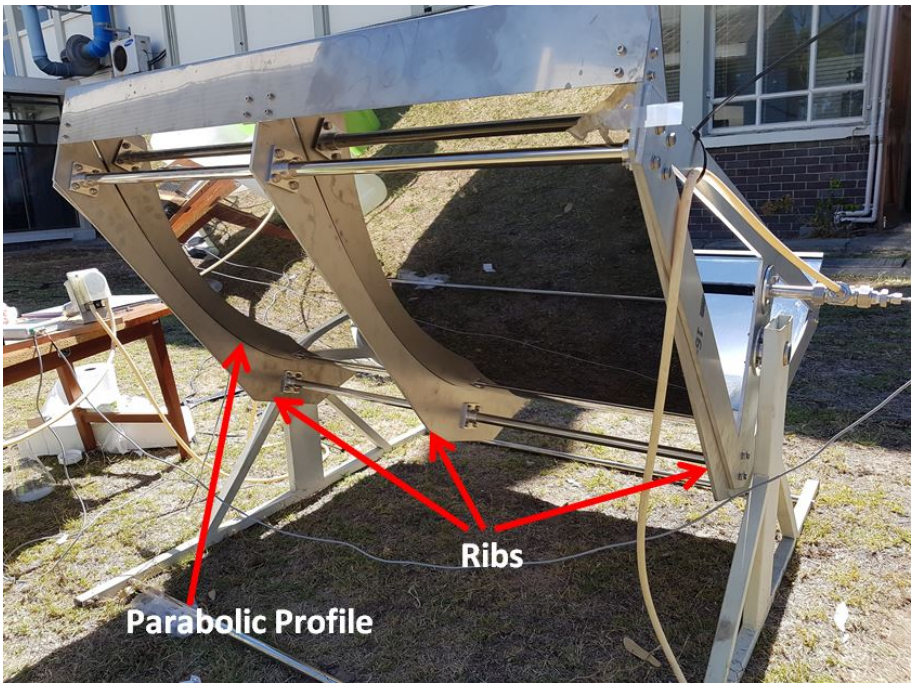

Figure 3.9: Parabolic trough rib placement

3.2.3 Reflector surface

In the selection process for a reflector sheet, the following factors were determined to be important, the sheet needed to:

- have a high reflectivity
- be low cost and readily available
- be easy to replace if damaged.
- be weather and corrosion resistant to a reasonable degree.
- be flexible enough to bend into a parabolic shape, and rigid enough to hold this form.
- be relatively lightweight, to keep total system weight low.

The material that was selected is 430 BA(Bright Annealed) grade polished Stainless Steel. This is a common type of steel with a good resistance to corrosion, it has an excellent surface gloss and is highly reflective. This type of metal sheet is low cost and will be available at most metal workshops throughout the country.

Although the reflectance of a stainless steel sheet such as this is only measured to be roughly 68% [94], compared to the commercial sheets which can reach reflectance's of above 90% [95], it is seen as an attractive alternative for a low cost system, because it is much cheaper, more readily available and has good corrosion resistance.

3.2.4 Receiver tube and coating

The selection of the receiver tube material and surface absorber coatings needed to take various factors into account. Not only did the tube need to be able to absorb as much solar energy as possible and transmit it efficiently to the working fluid, it also needed to be suitable for allowing milk and water to pass through the inside and be heated without being contaminated.

Dairy grade stainless steel tubing, which is made from 304 stainless steel, was thus chosen as the receiver tube material, because of the high purity and sanitary requirements of milk processing procedures. Although stainless steel only has a thermal conductivity of between 12 and 45 W/m°C, which is much less than other metals such as aluminium and copper that have thermal conductivities of up to 204 W/m°C and 386 W/m°C respectively, it is preferable because of its ability to withstand the chemicals that are used for the cleaning and sterilisation of the equipment without degradation [96, 97]. Stainless steel is used throughout many different food and beverage industries, including the dairy industry, because of its ability to be hygienically cleaned and its resistance to corrosion, making it the logical choice to stick with industry standards in this device. However, should another HTF be tested with the system in future, where resistance to chemicals and food safety is not of concern, the tube can be easily replaced with a material that has a higher heat conductivity, which would improve the system efficiency.

The outer surface of a machined stainless steel tube, has a solar absorptance of 0.47 and an emissivity of 0.14 [98], so in order to maximise the amount to solar energy absorbed by the tube, it needs to have a surface coating applied that will provide a higher solar absorptance.

3.2.4.1 Receiver tube surface coatings

In the testing of this system, three identical receiver tubes were used, however each was covered with a different surface coating. These coatings were Mirosol TS, a spectrally selective thickness sensitive paint applied onto thin aluminium sheets, a high temperature black spray paint, and candle soot. These three alternatives, two of which are shown in Figure 3.10, were chosen to compare the performance of a commercial product to cheaper and more widely available alternatives. Chapter 5 contains a detailed characterization study of the coatings used during the testing of this system, giving valuable insight about their material compositions and optical performances.

(a) Selective absorber sheets (b) Soot coating

Figure 3.10: Receiver tube surface coatings

The Mirsol TS sheets are primarily used in flat plate solar collectors, which generally do not reach the temperatures of which CSP systems are capable of. It was therefore important to assess if a coating such as this could be used in the system. In this device, the sheets were wrapped around the receiver tube, with thermal paste between them to try improve conductivity, and held in place with metal wire. This was done because the sheets could not be produced in a tubular form or coated directly onto the receiver tube. This coating method was not ideal and efficiency could be improved drastically if the selective absorber material could be applied directly onto the surface of the tube.

Black spray paint and candle soot were also used as coatings to determine whether the system would be able to reach the necessary temperatures with cheaper alternatives and without the use selective solar absorbers. Both black paint and soot, which can be applied to the absorber tube using a household candle, are not selective and are effectively black bodies, meaning their thermal emissivities are much higher than that of a selective absorber. However, if they could produce the desired results at their low cost, the implications for those that will make use of this technology in rural areas could be massive. The overall cost of the system could be greatly reduced and replacement of damaged coatings would require no new parts or significant investment .

Black spray paint was applied as a single layer on the tube, ensuring that all of the surface area was covered. The same was done with the soot coating, where a candle was moved underneath the tube so that its flame came into contact with its surface, resulting in the deposition of soot on the tube. Figure 3.11 shows what the process of coating the tube is like, and although it is time consuming for an individual, it is still highly effective.

Figure 3.11: Method to coat receiver tube with soot

3.2.5 Additional components

This subsection discusses all the additional components that were incorporated in the design to allow for repeatable and accurate tests to be conducted.

3.2.5.1 Sun aiming pin

One of the most important assisting components of the concentrating system is the aiming pin. Because this device was designed to be adjusted manually, it is important for the operator to know at all times if the system is correctly aligned, to ensure optimal focusing of the solar energy onto the absorber tube. A small aiming pin, shown in Figure 3.12, mounted on the rotating body on the same axis as the receiver tube, allows the operator to detect any potential misalignment as time passes during operation.

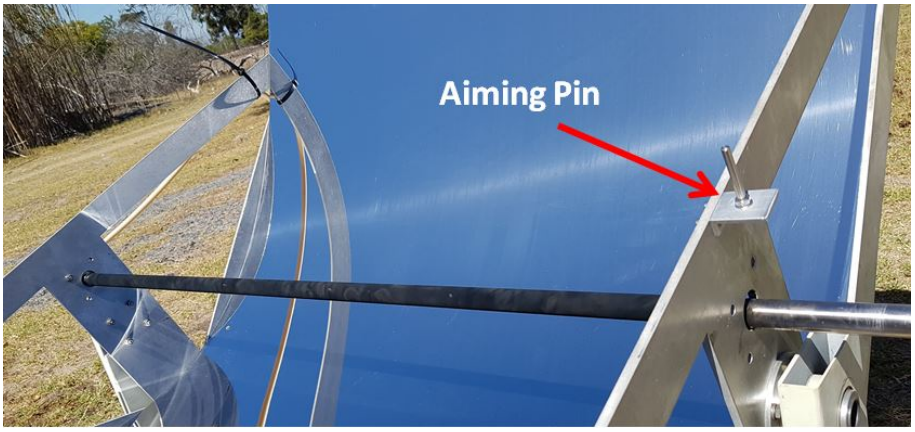

Figure 3.12: Sun aiming pin placement on CSP device

If the shadow cast by the pin on the aiming disk during operation is minimal, or absent altogether as in Figure 3.13(a), it indicates that the system is aligned correctly and that it is aiming directly at the sun. However, as the sun moves throughout the day, the pin will begin to cast a shadow, as shown in Figure 3.13(b), that is dependant on how misaligned the system becomes. By ensuring that the shadow is always kept to a minimum, the operator is able to ensure that the system concentrates the maximum amount of solar energy onto the receiver tube.

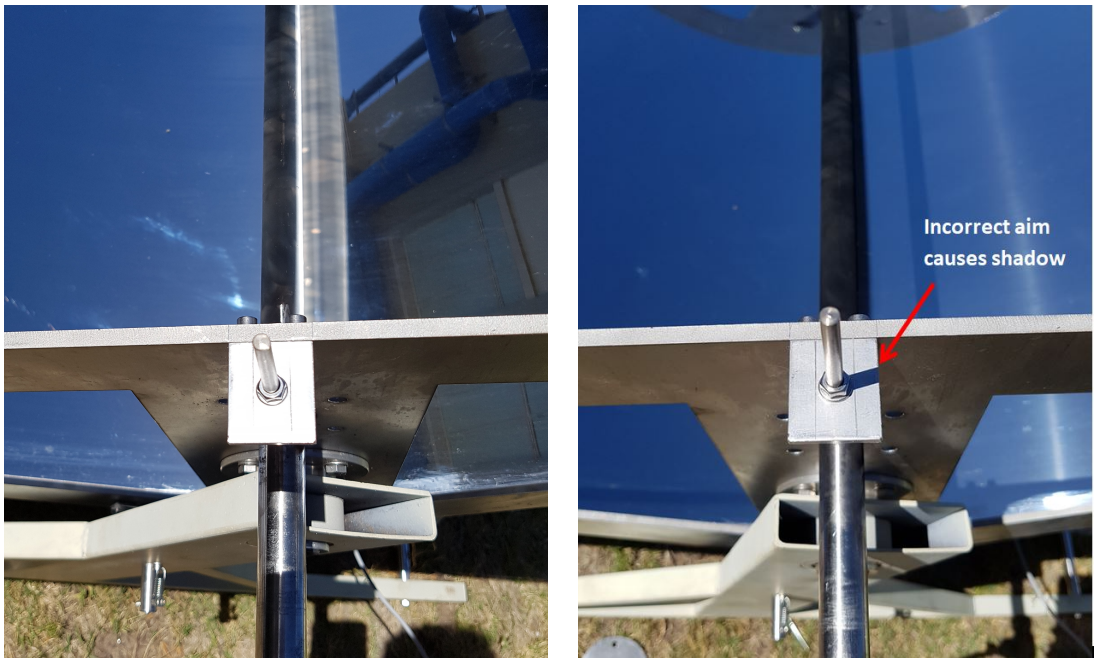

(a) CSP system correctly aimed (b) CSP system incorrectly aimed

Figure 3.13: Sun aiming pin in and out of focus

3.2.5.2 Pump system

The experimental set-up of this system also required the use of a pump and tubing system to facilitate the transfer of the HTF through the system. The pump needed to have an adjustable flow-rate to account for varying conditions in solar radiation on any particular day. It also needed to be safe to use with milk intended for human consumption, and with any chemical products that it may come into contact with during the cleaning process. The pump used in the system was a peristaltic pump with a Pulse Width Modulation (PWM) controller, shown in Figure 3.14. This pump is a type of positive displacement pump that is able to function with many different fluids over a large temperature range, with a maximum flow rate of 1 L/ min.

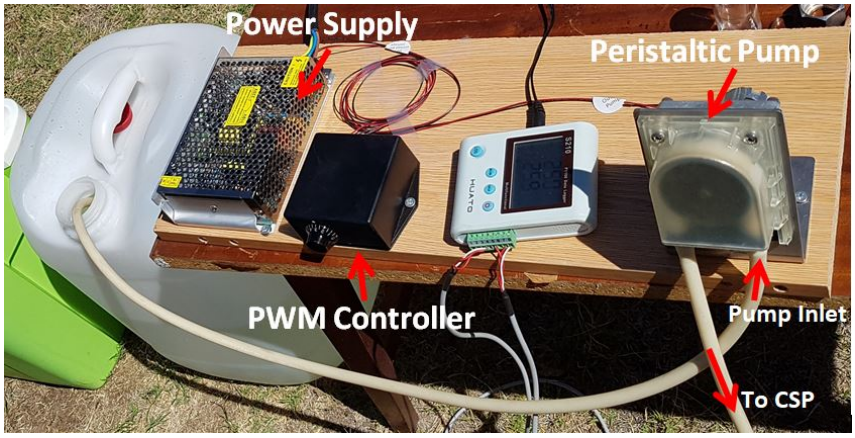

Figure 3.14: Peristaltic pump system components

Peristaltic pumps do not directly come into contact with the working fluid, and instead use two or three rollers to force the fluid through the attached tubes, as is illustrated in Figure 3.15. The tubing that was used in this application was Norprene® Food Grade tubing. This is a durable polypropylene based material that is compatible with most cleaning agents and sanitizers, and is used in food and dairy processing. This particular tubing is able to withstand temperatures up to 135 °C, which is more than sufficient for milk pasteurization [99].

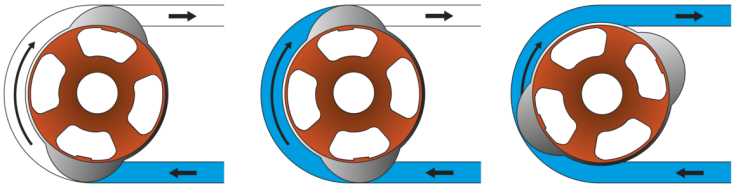

Figure 3.15: Flow of liquid through a peristaltic pump [100]

The pump system does not contain any automatic flow rate measurement device, as a device to measure the expected flow rates accurately, while also being safe to use with milk products, would need to be highly specialised and expensive. Instead, to obtain a rough estimate of the flow rates during the tests, when the desired output temperatures were reached, the measured volume output by the system over a certain time period was used to determine the flow rate.

In future, to allow this system to be used as an completely off grid device, this pump system could be powered with the incorporation of solar panels into the overall system. These panels could be used to provide the energy needed to power the pump and other small electronics that could be useful for the system to make use of.

3.2.5.3 Temperature probes and data logger

The milk pasteurization system required the use of two temperature probes and a data logger to keep track of, and record the inlet and outlet temperature of the system at all times. The temperature probes that were used were PT100, 3-wire simplex probes with pot-seal leads. The probes were 250mm in length, to allow for measurement in the direct flow of the HTF, 3mm in diameter, and made from SS316 to meet the sanitary requirements of the device. These probes were mounted onto each end of the receiver tube, as shown in Figure 3.16, where the signal wire of each is connected to the data logger for recording.

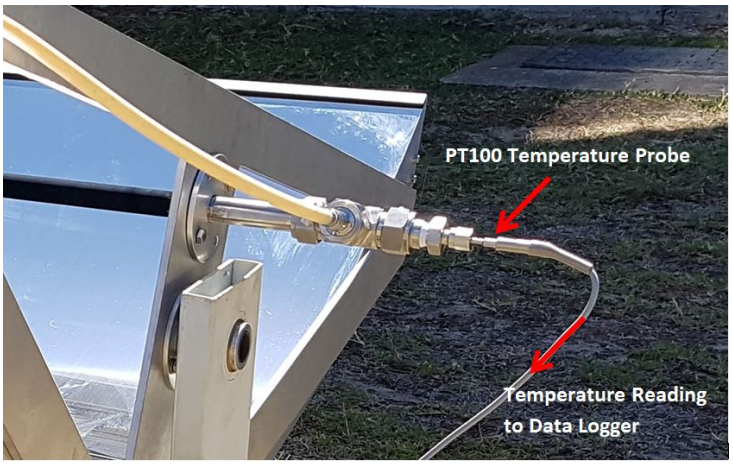

Figure 3.16: PT100 temperature probe mounted in experimental set-up

The data logger that was used, shown in Figure 3.17, is a two-channel PT100 data logger, where one channel is connected to the inlet temperature probe and the other to the outlet probe.

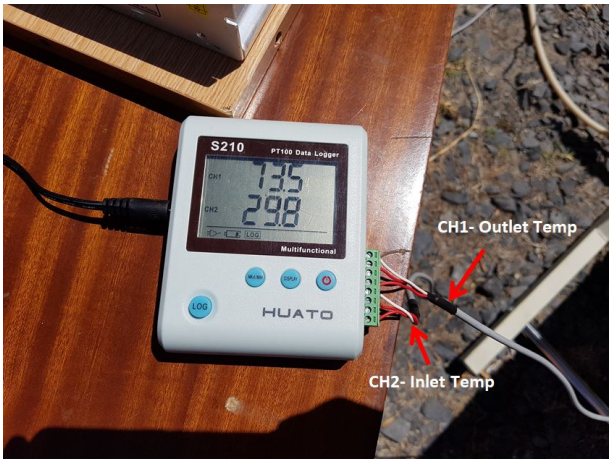

Figure 3.17: Data logger used in experimental set-up

3.2.5.4 Braking system

In order to ensure that the rotating body was kept aligned during operation, and did not fall out of position due to wind or other influences, a very basic friction braking system, shown in Figure 3.18, was added to the design. This mechanism consisted of a bicycle brake pad, a small metal rod and a spring. This was mounted onto the supporting frame and the natural position, held by the spring, keeps the rotating body in place with friction. When it is time to rotate the system, to keep it aligned with the sun, the operator pulls on the rod which releases tension on the brake, rotates the body as necessary and releases the rod which re-engages the brake.

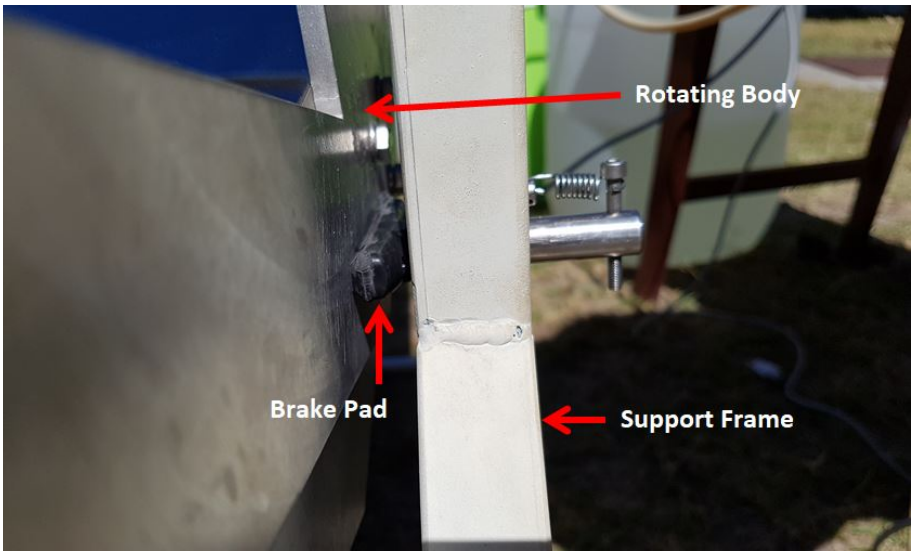

Figure 3.18: Parabolic trough simple braking system

3.2.6 Heat transfer fluids

At this stage of the system's development, two primary HTFs were used, namely water and milk. Water was used for the initial tests that were done on the system, as this allowed for the performance to be evaluated without the need for the cleaning processes associated with processing and heating milk. Milk and water have a similar specific heat capacity's c_p, of 3.93 and 4.19 (kJ/(kgK)) respectively [101], so the systems ability to heat water would therefore prove its ability to heat milk. Once the performance was proven with water, milk was then used as the HTF, and its ability to pasteurize milk was tested. The results of these tests are discussed in Chapter 6.

3.2.7 Testing location and solar data

All tests were conducted outside of the Materials Research Department, at iThemba Labs, the NRF research institute in Cape Town, South Africa.

All solar energy data obtained on the days of testing were gathered from Stellenbosch University (SUN) station, which is part of the Southern African Universities Radiometric Network (SAURAN). The distance between the two sites is approximately 16km.

3.3 Chapter summary

In this chapter the theory behind the design of a parabolic trough CSP system, and an overview of the geometrical and optical considerations involved in such a design were given. It also contained information on all other considerations that needed to be made in the system design, as well as the final parameters and a description of the important components of the designed CSP milk pasteurizing system.

Chapter 4

Characterization techniques

This project utilised three different kind of receiver tube solar absorber coatings, and to learn more about the behaviour and properties of these coatings, various different characterisation techniques were used. These methods allowed for information to be obtained about the materials such as their optical properties, morphological structures and chemical compositions. A brief overview of the technologies used for these studies, and the basic principles they involve, are described in this chapter.

4.1 UV-vis-NIR diffuse reflectance spectroscopy

UV-vis-NIR spectroscopy was used to study the optical properties of materials over a range of wavelengths, from 200 nm in the UV region to 2500 nm in the NIR region. This was done using a spectrophotometer, a device which allows measurements of reflectance to be taken of liquid, solid or powder samples over the specified wavelengths. From these measurements, the solar absorption can then be calculated using solar energy data over the same wavelength spectrum. This analysis technique can provide large amounts of information about the physical and chemical properties of samples that cannot be obtained using other methods, and thus has applications in a wide range of fields.

The most common method for measuring diffuse reflectance is by using a spectrophotometer that is equipped with an integrating sphere. This allows the device to measure the total and diffuse reflectance, as well as the transmittance of a sample. This is done by setting up the sample in one of the configurations that are shown in Figure 4.1 [102]. The configuration on the left shows that which is used for the measurement of reflectance, where R_d and R_s represent the diffuse and spectral reflectance respectively. In this configuration, Plate-1 would be replaced with a detector able to measure the spectral reflectance [102]. There are other setup variations that are designed to measure the diffuse reflectance, and this can be done by changing the location of the detector, through the use of a light dampening cone, or by changing the working angles of the beam and sample so that only the diffuse component of the reflectance is received by the detector.

The configuration shown on the right of Figure 4.1 illustrates how the transmittance of a sample would be measured, where Plate-2 would be the region at which the specular component of the transmittance, T_s, would be measured. The diffuse transmittance, T_d, would be measured by replacing Plate-2 with a light dampening cone and measuring the

remaining light inside the sphere at Plate-1 [102].

A Cary 500 Series UV-vis-NIR spectrophotometer, from Agilent Technology, equipped with an integrating sphere, was used for testing included in this thesis, to determine the total diffuse reflectance of the samples in the range of 200 - 2500 nm.

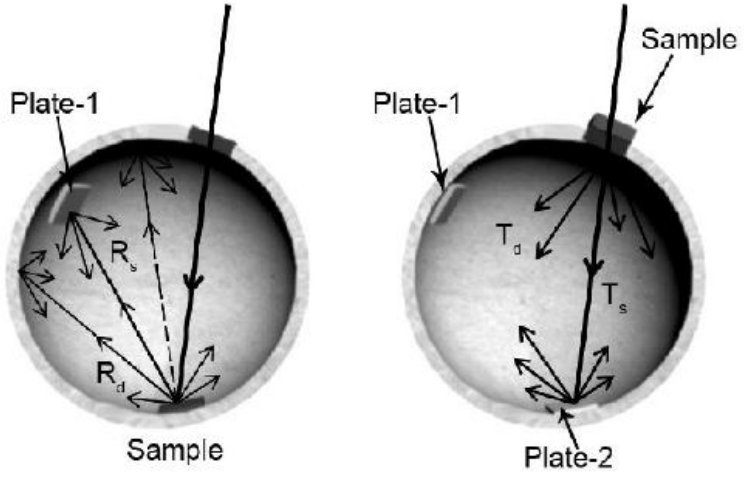

Figure 4.1: Integrating sphere configurations for reflectance (left) and transmittance (right) measurement [102].

4.2 Scanning electron microscopy and energy dispersive X-ray spectroscopy

A HR-SEM is a high resolution microscope that allows specimens to be magnified at high levels. This type of microscope forms an image of the target sample by using electrons and electromagnets instead of light and lenses, and by doing this it allows for more control over the magnification [103]. The highly magnified images allow for detailed analyses and studies to be done on the surfaces of samples. A Zeiss Auriga HR-SEM was used in this study to investigate the surface structure of the different receiver tube absorber coatings.

The typical layout of a SEM device is shown in Figure 4.2. The electrons are generated in the top region of the SEM, known as the electron gun, and are then accelerated towards an anode, with voltages that can range from 0 to 30 kV. The simplest gun uses a heated tungsten wire as its source of electrons, but more expensive types use crystals (lanthanum hexaboride, LaB_6, or tungsten) [104]. Magnetic lenses then manipulate the produced electron beam, and focus it on the sample with a smaller diameter than it is generated with. The beam also passes through scanning coils inside the objective lens, which further focus the electron beam onto a specific region of the sample.

The energy of the focused beam is then transferred to the targeted specimen, which causes it to eject secondary- (SE) and backscattered electrons (BSE). The secondary electrons are low energy electrons ($<$50 eV) that are formed by inelastic scattering.

These can be detected and provide good edge detail and form the usual surface image of the specimens [104]. BSEs have higher energies (>50 eV) and are used to produce images that use contrast to illustrate the average atomic number of the sample. The final image is then generated based on all the electrons that are emitted from each spot on the specimen, and this gives the images a three dimensional appearance. The resolution of these devices are based on the size of the electron beam and the interaction volume, and different instruments can achieve resolutions in the range of between 1 nm and 20 nm.

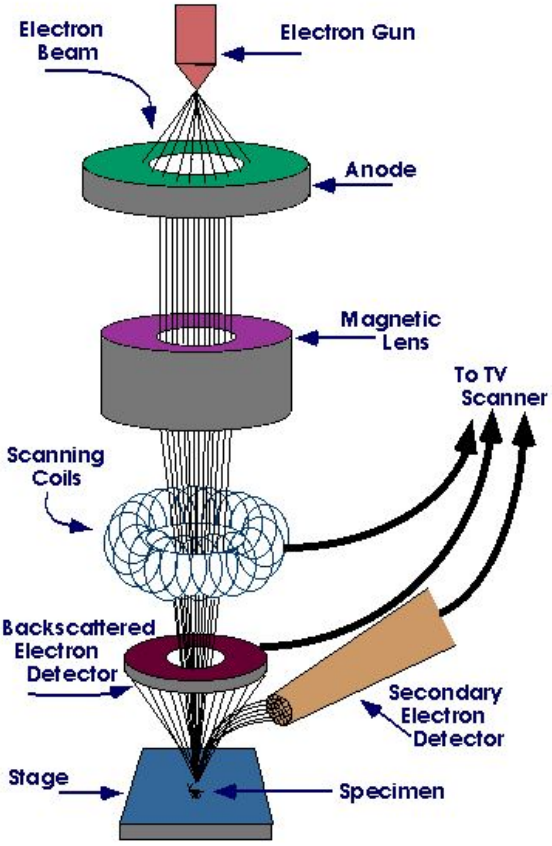

Figure 4.2: SEM schematic [103]

Energy dispersive X-ray spectroscopy (EDS) is an analysis technique that is generally integrated into SEM systems, because it is unable to operate on its own. This technique utilizes the detection of X-rays, emitted by a sample during exposure to an electron beam, to characterize the elemental composition of a target area on a sample [105]. This is done by bombarding the surface with the electron beam of the SEM, causing its atoms to eject electrons. The vacancies that result from this ejection are then filled by electrons from higher states. To balance the difference in energy between the two electrons' states, the higher state electron emits an X-ray when filling the vacancy. The energy levels of these emitted X-rays are characteristic of different elements, and by detecting them in this manner, the elemental composition of the target areas can be accurately determined [105].

4.3 Transmission electron microscopy

Transmission electron microscopy is another technique also used to obtain highly magnified images of samples, done by using many of the same optical operating principles as standard light based microscopes. Instead of using a light source, however, a TEM device makes use of an electron source, as is used in SEM, which allows them to also have a much higher resolution than standard light based microscopes. There are several similarities between TEM and SEM, both of which function by making use of electron beams. The main difference between the two however, is that the images produced by SEM are based on scattered electrons, whereas those of the TEM are created based on the electrons that are transmitted through a target sample. Also, while SEM produces images that appear to be 3D, TEM can only produce flat images in 2D.

A simplified schematic of a TEM device is given in Figure 4.3. It shows a reduced system that consists of four main components: an electron source, electromagnetic lens system, sample holder and an imaging system [106]. The electron source operates in a similar manner to that which is used in SEM, however, the accelerated voltages are usually set to a much higher range, from around 60 - 300 kV [107]. This beam is then focused in the electromagnetic lens system through a combination of magnetic lenses and an aperture, which restrict the beam allowed to pass through it to a defined energy level. The samples being imaged, held in the sample holder, are also limited in size and generally need to be less than 150 nm thick in order to produce desirable results. The machine shines the restricted electron beam through the target sample, and the electrons transmitted through are then used to generate images. This is done with another electromagnetic lens system that concentrates the transmitted beam onto an imaging plate. The imaging plate can make use of a phosphor screen, which glows upon electron impact, a CCD (charge-couple device) camera or an image producing film to generate an image dependant on the electrons that are projected onto it. The image produced is essentially a grey-scale "shadow image" of the specimen, with darker regions indicating a higher densities or overlapping particle structures.

TEM machines, because they utilize electron beams in a similar manner to SEM systems, are also able to perform EDS analysis on target samples by incorporating an additional spectrometer into the system. This allows for the elements present to be identified based on the emitted X-ray energies measured, which are characteristic of specific atomic structures and caused by the interaction of the electron beam with the sample. TEM machines are also able to perform selected area electron diffraction (SAED). This technique is used to gain further insight about material structures and possible defects that could be present. An aperture with several differently sized holes is placed below the sample holder, which selects a specific area of the sample to be targeted. The transmitted electrons that are able to pass through the aperture then project patterns onto the imaging plate, which are dependant on the crystalline structure of the material. The patterns that are produced then give a good indication of the crystalline structure of the sample.

The TEM system used for sample characterization during the course of this project was a FEI Tecnai G2 20 field-emission gun (FEG) TEM. This system was equipped with the necessary components to obtain TEM images as well as do EDS and SAED. It was operated in bright field mode while using an accelerating voltage of 200 kV. The energy

dispersive X-ray spectra were collected using an EDS liquid nitrogen cooled lithium doped silicon detector.

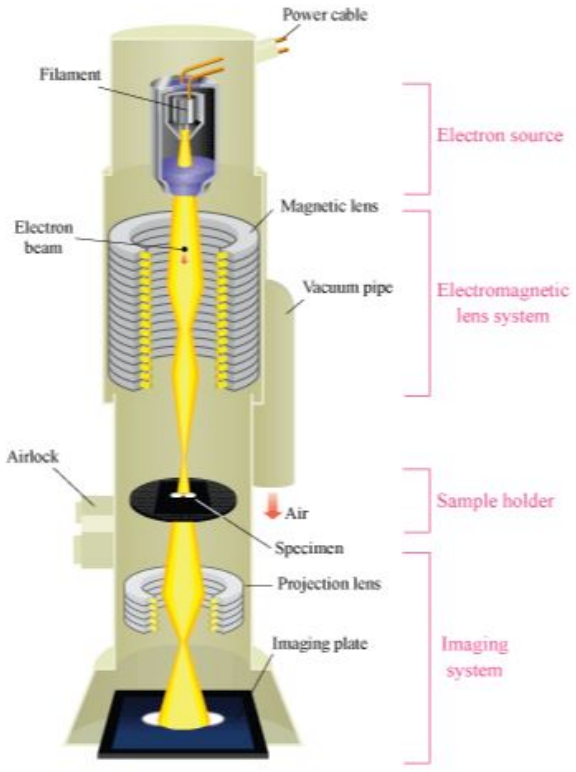

Figure 4.3: TEM schematic [106]

4.4 X-ray diffraction

XRD is an analysis technique that can be used to identify the phases of a crystalline material, atomic spacing, unit cell dimensions, sample purity and can also be used to identify fine-grained materials. This is a rapid technique for identification, and interpretation of the data is relatively straightforward. The process generally provides distinct elemental compositions of samples, and require minimal sample preparation before the analysis [108].

The diffractometers used for XRD contain three primary elements: an X-ray tube, sample holder and an X-ray detector. A schematic for an X-ray diffractometer is given in Figure 4.4, which illustrates a generalised beam path for the X-rays during the analysis. The X-rays are generated in the tube, which is a cathode ray tube, by heating a filament to produce electrons, and by applying a voltage these electrons are accelerated towards the target, which is bombarded with these electrons [108]. When there is enough energy in this bombardment, electrons of the inner shell of the material are dislodged, producing an X-ray spectrum. The specific wavelengths produced are dependant on the target used (Cu, Fe, Mo, Cr), and filtering is used to ensure that the rays are monochromatic and parallel [108].

The sample and the detector, at angles θ and 2θ, are rotated through a range of angles while exposed to the X-ray beam, as shown in Figure 4.4, and the intensity of the reflected X-rays are measured and recorded throughout these ranges. Peak intensities occur when lattice planes with certain d-spacings, a measurement of the inter-atomic spacing, in the material are appropriate to diffract the X-rays at the current rotation angle θ. The resulting peaks that are observed are then compared to databases of known materials with specific d-spacings, and based on the intensities measured, an accurate analysis of the material composition and surface structure can be determined [108].

The diffractometer used was a manufactured by Bruker AXS (Germany) and was used at the XRD facilities at iThemba Labs, Materials Research Department. The device used was a D8 Advance diffractometer with a LynxEye position sensitive detector, and a Cu-Kα radiation tube ($\lambda K\alpha_1 = 1.5406$ Å).

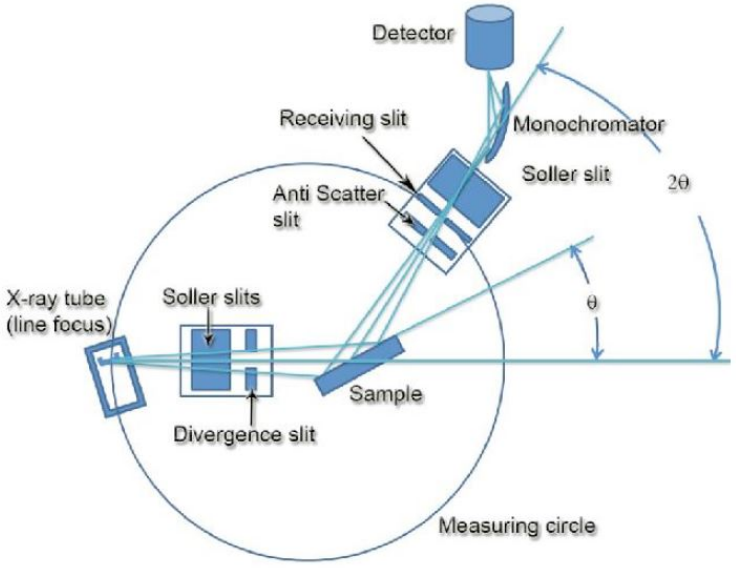

Figure 4.4: X-ray diffractometer beam path schematic [109]

4.5 Raman spectroscopy

Raman spectroscopy is a spectroscopic technique that is used to provide information about molecular vibration crystal structures. This is done by irradiating a sample with a laser light source, which produces a tiny amount of Raman scattered light to be detected using a CCD camera. This analysis technique is non-destructive, does not require sample preparation and can have a resolution on the sub-micron scale [110].

When light is scattered the majority is a result of Rayleigh scattering, which is an elastic process that results in no change in energy. A small portion undergoes an inelastic process, in which the scattered light has a different energy to the incident light, this type of scattering is known as Raman scattering, and is caused by the Raman effect [110].

Raman spectroscopy deals with the change in frequency observed when molecules cause the scattering of light. The Raman frequency is the magnitude of the frequency shift between the incident light v_o and the scattered light v_r, where $\triangle v = v_r - v_o$, which can either be positive or negative. There are two components of Raman scattered light, namely Stokes Raman- and anti-Stokes Raman scattering. Stokes Raman scattering involves energy absorption by the molecule, and results in the scattered light having less energy and a longer wavelength. The opposite is true for anti-Stokes Raman scattering, where the scattered light gains energy and has a shorter wavelength than the incident light [110]. The energy diagram illustrating the energy change in Rayleigh, Raman Stokes and Raman anti-Stokes scattering is shown in Figure 4.5, where S_0, S_1 and S_2 are electronic energy levels and the dotted lines represent virtual states.

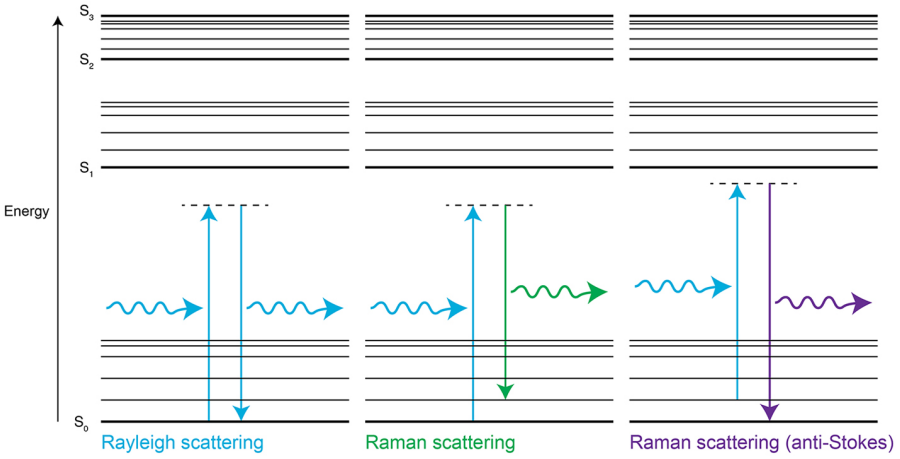

Figure 4.5: Rayleigh and Raman scattering energy diagram [111]

Raman scattering is caused by molecular vibration, and the results are given as a Raman spectrum, expressed as the intensity of scattered light versus the Raman shift (reciprocal of wavelength). A peak in the Raman spectrum would be caused by a specific lattice- or molecular vibration, and its width is an indication of the crystallinity of the material. This method of spectroscopy is used in a variety of fields and has a range of different applications, which include substance or polymorph identification, tracking changes in molecular structures or crystallinity, and assessing the orientation of molecules.

A basic overview of the components that make up a Raman spectrometer are shown in the schematic diagram of Figure 4.6. These various components allow for specific wavelengths, from the monochromatic laser, to be utilized and correctly focused on the sample, and for the resulting Raman scattered light to be isolated from the Rayleigh scattered light and measured.

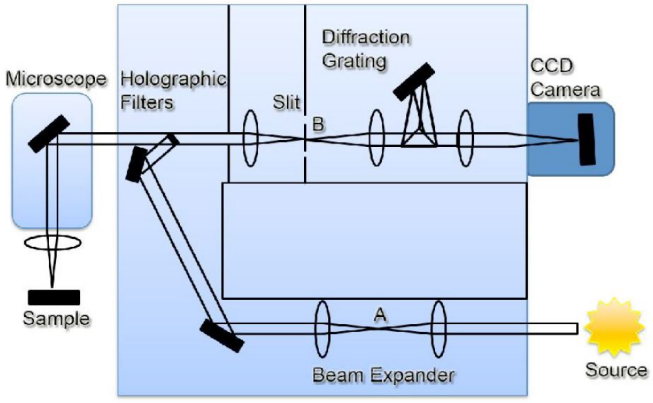

Figure 4.6: Schematic layout of a Raman spectrometer [112]

4.6 Chapter overview

This chapter gave descriptions of the different analysis and characterization techniques that were used in this project to assess different aspects of solar absorber coatings, the results of which appear in the following chapter. By looking at how the systems function and the main principles on which they are based, the results obtained from them become more easily understandable and intuitive.

Chapter 5

Solar absorber material characterization

This chapter discusses a characterisation study that was done on different absorber coatings for a receiver tube. It contains the assessment of a commercial selective solar absorber as both a flat sheet and after it was bent into a tube shape. Both of these were heated to temperatures at which performance was expected to degrade. Characterisation was also conducted on candle soot and black spray-paint as possible receiver tube coatings for low cost applications, the results of which are also given.

5.1 Absorber study introduction

This study served three different purposes. The first was to assess how exposure to elevated temperatures could cause changes in the material structural and to its optical properties of a commercial selective solar absorber coating. This would lead to obtaining a better understanding of its stability as a solar absorber. The material used was *Mirosol TS*, a product of *Alanod GmbH* [113]. The second was to determine whether the same commercial solar absorber sheet could be used as a coating for the tube of a parabolic solar trough, without the coating losing its desirable properties in a bending process. The third purpose of this study was to determine whether a spray paint or soot coating, applied using the flame of a lit candle, could be a practical way to coat the receiver tube, and act as a solar absorber coating with high solar radiation conversion efficiency. In order to use spray-paint or soot for such an application, it is important to first understand what properties and structures these potential coating possess.

The focal point of CSP systems can reach high temperatures during operation, and it is therefore important to ensure that the materials and coatings used can still function optimally when exposed to these temperatures. The commercial absorber was tested in its original flat shape, and in tubular form after being rolled. The temperatures at which the samples were all held, for a period of 1 hour each, ranged from 100 °C to 500 °C in increments of 100 °C. After annealing the samples at these temperatures, morphological analyses, as well as optical tests for determining the total diffuse reflectance's were conducted in order to assess the effect of elevated temperatures.

The soot samples, after being coated onto a glass and stainless steel substrate, were analysed using various methods mentioned in Chapter 4 to determine its optical

properties, surface structure and material composition. The black spray-paint was also coated onto a glass substrate and had its optical properties measured in a similar manner.

5.2 Experimental techniques

This section describes the procedures and steps used in preparing and analysing the different samples in this study.

5.2.1 Sample preparation

Commercial selective solar absorber

The sheets of Mirosol TS were provided by Alanod Solar in A4 size. The sheets consisted of an aluminium substrate coated with the selective solar absorber, and covered with a removable protective layer to prevent any surface damage during handling and preparation.

The sheets were cut to a more acceptable size for testing, approximately 1 cm x 3 cm, using a metal guillotine. Half of the strips cut were then rolled, with the selective absorber coating facing outwards, around a tube with a diameter of 10 mm. The other half of the guillotined samples remained as flat sheets so that a comparison could be made between the two types [2].

After removing the protective sheets on the samples, they were then put under vacuum conditions and heated to temperatures that ranged from 100 °C to 500 °C inside a TSH12 horizontal tube furnace, manufactured by Elite Thermal Systems Limited. The samples were held at these elevated temperatures for 1 hour each [2].

Soot coating

The soot coated glass and stainless steel substrates were tested as the low cost, readily available, alternative to commercial absorber products. To allow for comprehensive testing to be done on this type of coating, both glass and stainless steel substrates were used. This was done by holding the substrates in place at an angle, and by passing a burning candle underneath them. When the substrates came into contact with the flame, it resulted in the incomplete combustion of the flame, causing a layer of soot to be deposited on the substrate, and after several passes the resulting coat was uniform in colour and appearance. Figure 5.1 shows the glass slide used in the characterization that has been coated with candle soot.

To allow the soot coating to be analysed using HR-TEM, EDS and SAED, the coating was added to ethanol and sonicated for 10 minutes in a water bath to disperse the particles. A single drop was then drop-coated onto a carbon coated copper grid, and dried under a Xenon lamp for $\pm$ 10 min.

Black spray-paint coating

The black spray-paint coating was also applied to a glass substrate, and was tested as another low cost alternative to commercial solar absorbers. The paint used was a high temperature black spray-paint that is heat resistant up to 350 °C. It was used to coat an identical glass substrate to the one used for the soot coating, both of these can be seen in Figure 5.1.

Figure 5.1: Glass slides coated with candle soot (left) and black spray-paint (right)

5.2.2 Supplementary characterization tools

To interpret the images and for evaluating the Particle Size Distribution (PSD) of both the HR-SEM selective solar absorber images and HR-TEM images of the soot coating, a computer program called ImageJ Version 1.50e was used. This program runs on Java 1.8.0 and allows for the particle sizes to be accurately manually measured and stored [2].

Diffuse reflectance of the samples was measured using a spectrophotometer. MATLAB was then used to determine the solar absorption of the materials. AM 1.5 solar energy data was used in these calculations, and the MATLAB script used can be found in Appendix D.

5.3 Commercial selective absorber coating characterization results

This section highlights the results obtained for the characterization study of the commercial selective solar absorber.

5.3.1 Flat samples HR-SEM analysis

The analysis of the samples using the HR-SEM showed that the original sample of Mirosol TS, before any annealing, consisted of small dispersed particles with an average size of 73 nm, this highlighted that the thin film absorber contained nano-particles [2]. The SEM images, presented in Figure 5.2, illustrate that through the process of annealing, the higher temperatures result in the coalescence of the dispersed nano-particles to form more dense and compact structures [2]. This results in larger average particle sizes for samples that were exposed to higher temperatures. For the 200 and 500 °C samples, the average sizes were found to be 105 nm and 130 nm respectively. The PSD of the annealed samples, with the normalized frequency of the particle sizes given on the y-axis, are shown in Figure 5.3. These distributions have been fitted with a Gaussian distribution curve, which is the solid line on each plot, and all samples are shown to have a narrow bandwidth of particle sizes [2]. These PSDs confirm the observed agglomeration in the HR-SEM micro images, making it clear that higher annealing temperatures result in an increase of average particle size of the samples.

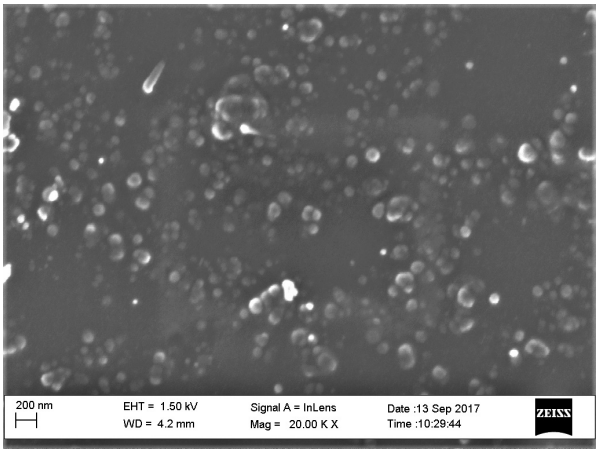

(a) Original sample

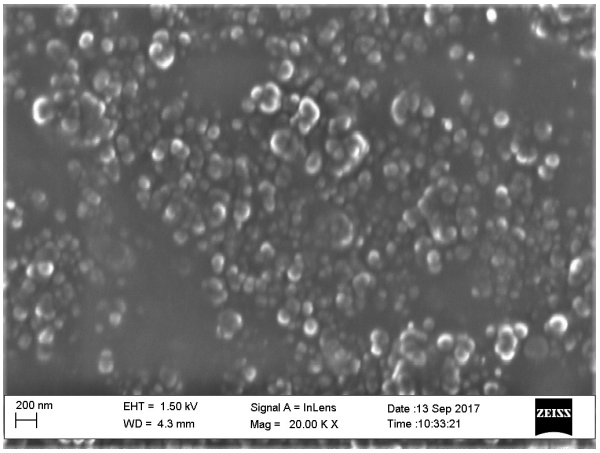

(b) Heated 100 °C - 1 hour

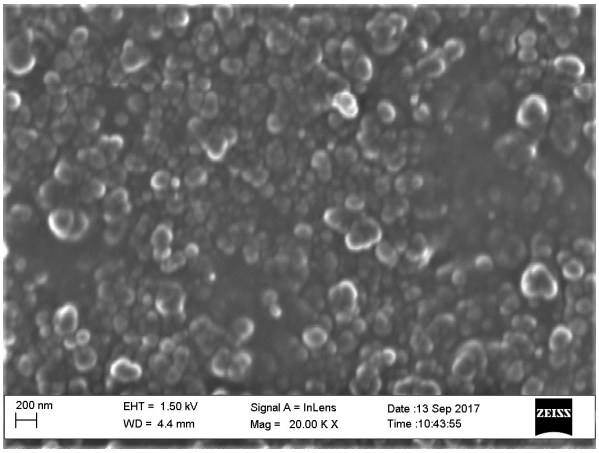

(c) Heated 200 °C - 1 hour

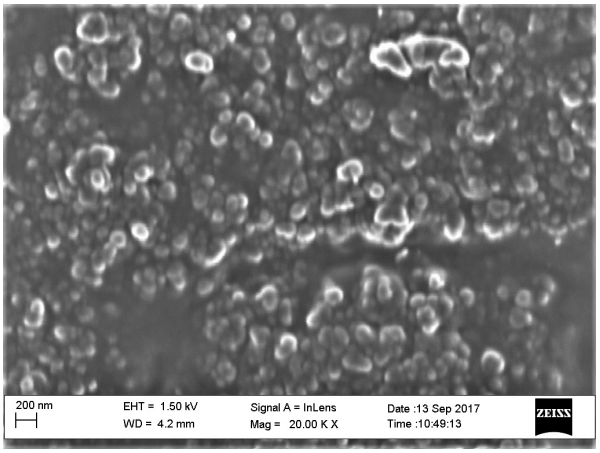

(d) Heated 300 °C - 1 hour

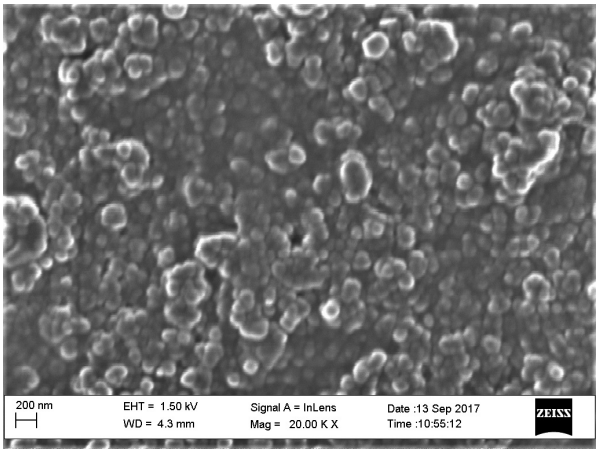

(e) Heated 400 °C - 1 hour

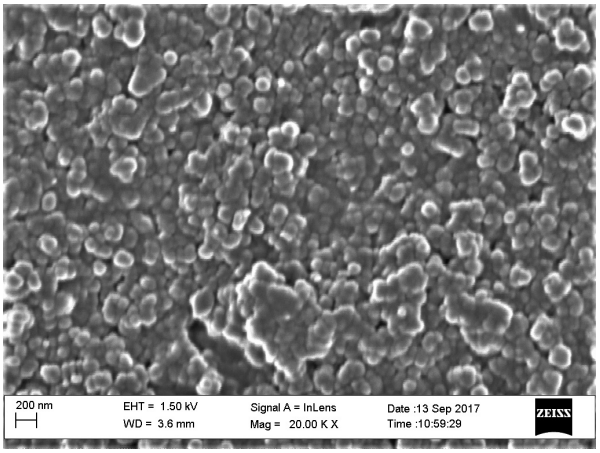

(f) Heated 500 °C - 1 hour

Figure 5.2: SEM images of flat samples [2]

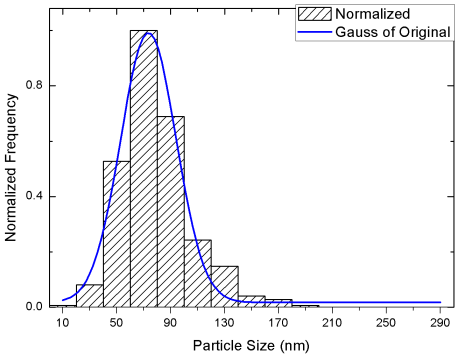

(a) Original sample

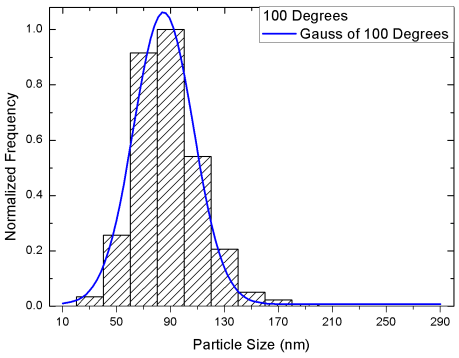

(b) Heated 100 °C - 1 hour

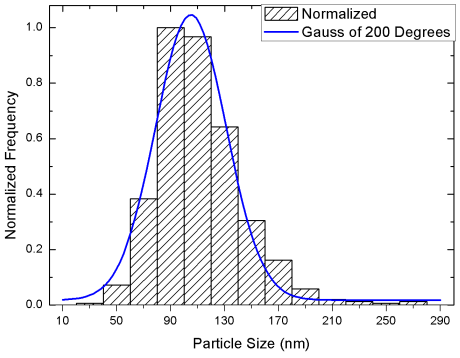

(c) Heated 200 °C - 1 hour

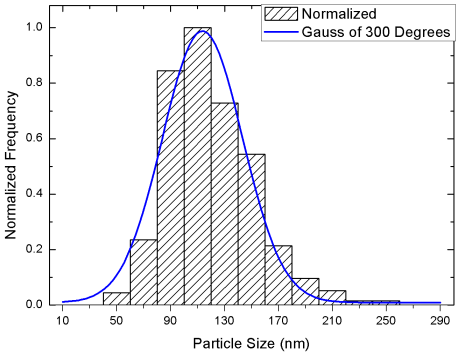

(d) Heated 300 °C - 1 hour

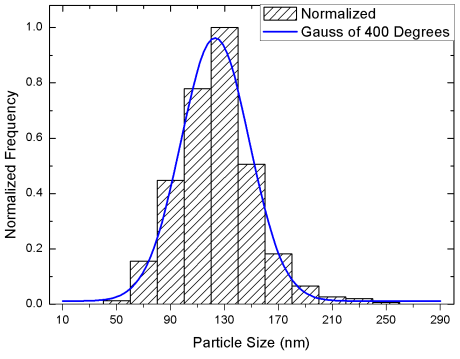

(e) Heated 400 °C - 1 hour

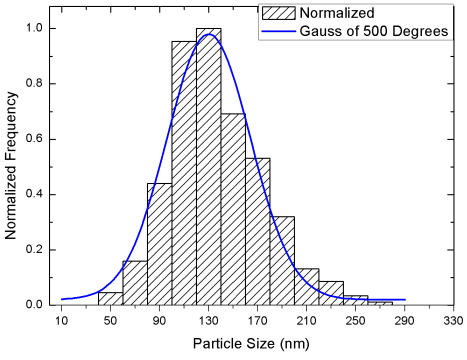

(f) Heated 500 °C - 1 hour

Figure 5.3: Particle Size Distribution of flat samples [2]

5.3.2 Flat samples diffuse reflectance study

The diffuse reflectance of each of the annealed samples was measured using a UV-vis-NIR spectrophotometer equipped with an integrating sphere. The results are shown in Figure 5.4 alongside the solar energy spectrum at air mass 1.5 (AM 1.5) . The measured reflectance's indicate that, when annealed at 100 and 200 °C, the samples maintain their good selective properties and display very little degradation relative to the original sample. As the annealing temperature increases however, from 300 °C upwards, the optical properties of the samples begin to degrade and reflectivity begins to increase at a faster rate from a wavelength of around 800 nm [2]. In addition to that, the cut-off wavelength in the reflectivity spectrum was shifted towards shorter wavelengths.

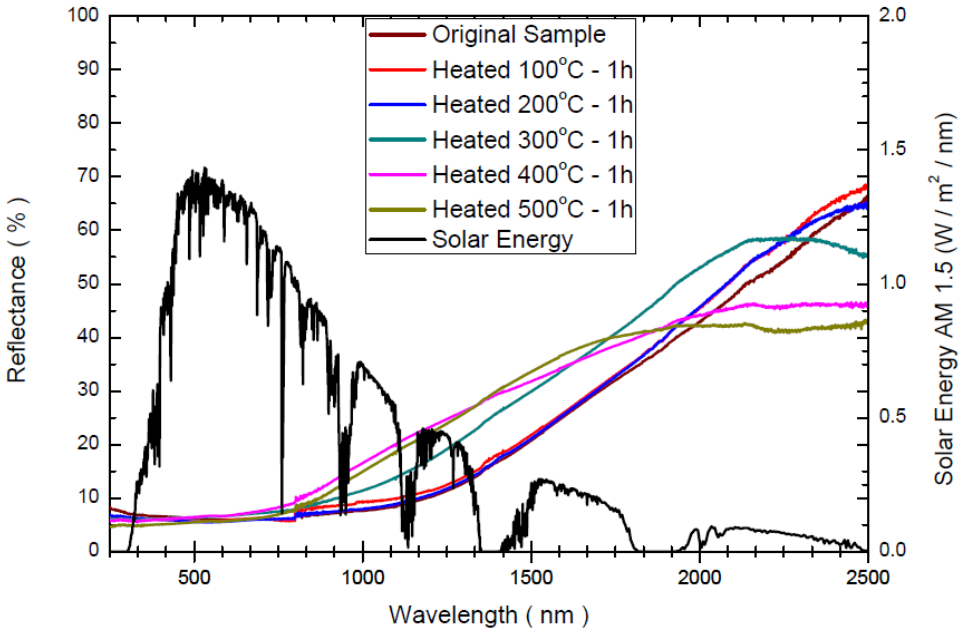

Figure 5.4: Measured diffuse reflectance of flat samples [2]

To calculate the total solar absorption of the annealed samples, the measured diffuse reflectance of the samples from 200 to 2500 nm and the corresponding solar energy at AM 1.5 for each wavelength were used. The absorption that was calculated for the original sample, as well as the measured reflectance confirm the absorption and optical properties of the coating given by the manufacturer, which stated that the absorber selective material has a solar absorption of 90% [113]. The material was able to maintain this level of absorption when heated to both 100 and 200 °C. However, the result of the increase in reflectivity in the 300 °C and above samples, can be seen in the lower absorption of these samples as is shown in Table 5.1 [2]. These calculated absorptions are also illustrated in Figure 5.5.

Table 5.1: Calculated absorption of annealed, flat selective solar absorber samples [2]

Heating Temperature	Calculated Absorption
Original	0.8999
100 °C	0.8954
200 °C	0.8993
300 °C	0.8745
400 °C	0.8633
500 °C	0.8737

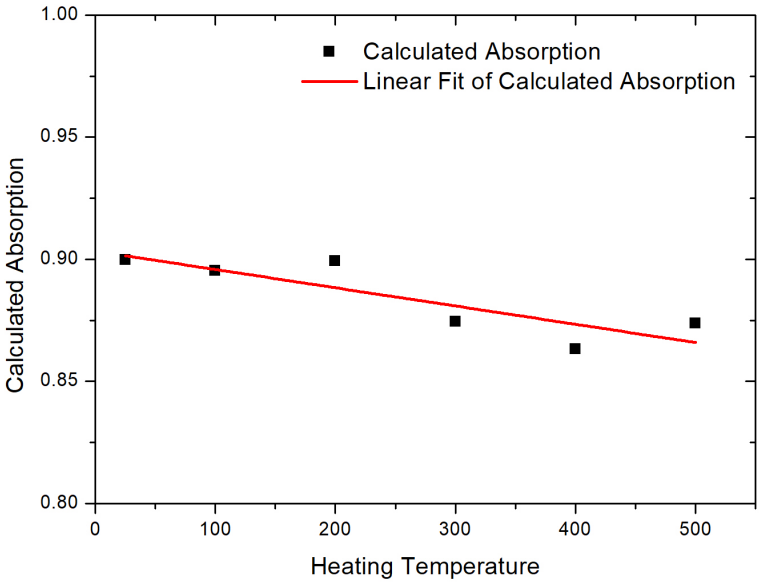

Figure 5.5: Calculated absorption of flat selective solar absorbers after heating

5.3.3 Diffuse reflectance of curved vs. flat samples

The samples of Mirosol TS that were bent into a tubular shape underwent an identical annealing process to the flat samples mentioned previously. The diffuse reflectance of these curved sheets was then measured in the same range as the flat alternatives, the results of which were used to determine the absorption. The diffuse reflectance results of the unheated (original) and 200 °C heated, curved samples are plotted in Figure 5.6 on the same axis as their flat equivalents. It is clear from the figure that their optical properties are almost identical. This was confirmed by using (2.4) to calculate the absorption of the samples, which are given in Table 5.2 [2].

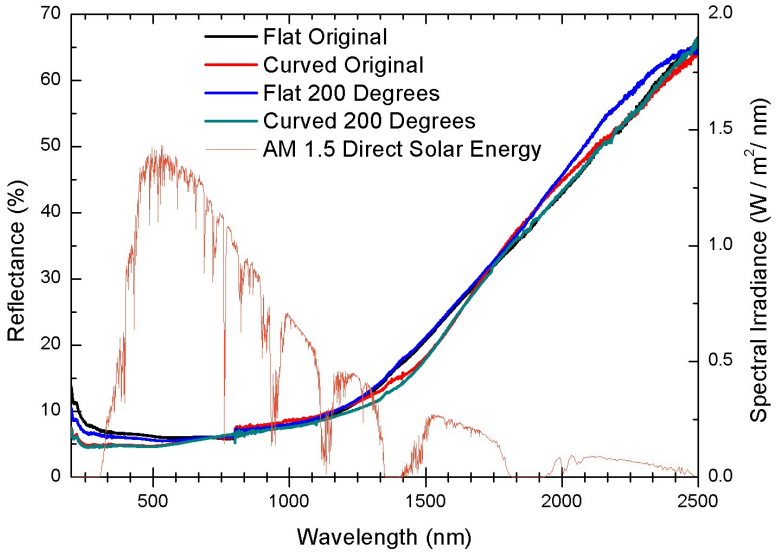

Figure 5.6: Measured diffuse reflectance of curved vs. flat samples [2]

Table 5.2: Calculated absorption of flat and curved samples [2]

Sample	Shape	Calculated Absorption
Original	Flat	0.8999
Original	Curved	0.9041
Annealed 200 °C	Flat	0.8993
Annealed 200 °C	Curved	0.9075

5.3.4 Discussion of commercial selective absorber coating characterization

The degradation of the Mirosol TS thin film solar absorber, observed in the diffuse reflectance spectrums (Figure 5.4) was due to the heat induced surface modification. As observed in the HR-SEM micro-image (Figure 5.2) the grains growth at the surface of these thin films increased their surface roughness, which leads to a degradation when the samples were heated above 200 °C. This observed grain growth can be linked to a phenomenon known as solid-state dewetting [114–116]. This is a process whereby the relatively smaller individual particles of a thin film undergo agglomeration to form larger 3D islands [115]. This process is driven by capillary forces and is initiated when heat is sufficient to activate mass transport of the particles. It is also known to rapidly form and extend any defects or voids that are present on the surface of the film [115, 116]. The change in surface structure causes the overall roughness of the film to increase, caused by these spreading defects [114]. In this selective solar absorber, as a result of heating, the agglomeration of particles began to gradually reduce the thickness of the coating in some parts, affecting the overall homogeneity of the thin films and exposing more of the aluminium substrate to air, allowing surface oxidation to take place. This resulted in an increased reflectance of the samples in the UV-vis region of the solar spectrum, and a reduction in their efficiencies as selective solar absorbers.

The diffuse reflectance measurements of the curved selective absorber samples displayed no apparent decrease in performance relative to the flat samples. This shows that, should the coating need to be used for an application whereby its substrate would be curved instead of flat, it would be able to match the performance of the flat sheets up to 200 °C.

5.4 Deposited candle soot coating characterization results

This section contains the results of the soot based solar absorber coating characterization. It includes XRD, Raman, HR-SEM and HR-TEM analyses as well as diffuse reflectance measurements. The soot coating to be used on the receiver tube is expected to be composed of amorphous hydrocarbons and elemental carbon as a result of the incomplete combustion of the flame [117]. Soot is also generally deposited as a dendritic structure with the majority of its weight percentage being oxygen and carbon. This characterization should therefore confirm that the coating being produced displays the same material properties [117–119].

5.4.1 HR-SEM analysis of deposited candle soot

The images obtained from the HR-SEM, shown in Figures 5.7(a) and 5.7(b), illustrate that the soot coating consists of spherically shaped nanoparticles that are arranged in a dendritic structure. Figure 5.7(b) also shows in more detail that many of the particles are agglomerated and have sizes that appear to be, on average, <50 nm. The dendritic structure that the soot particles form when coated on the surface can also play a role in the absorptive properties in the material. The porosity of the structure can allow for the material to trap light inside and assist the pigmentation, which gives the black colour, with the absorption of the solar energy.

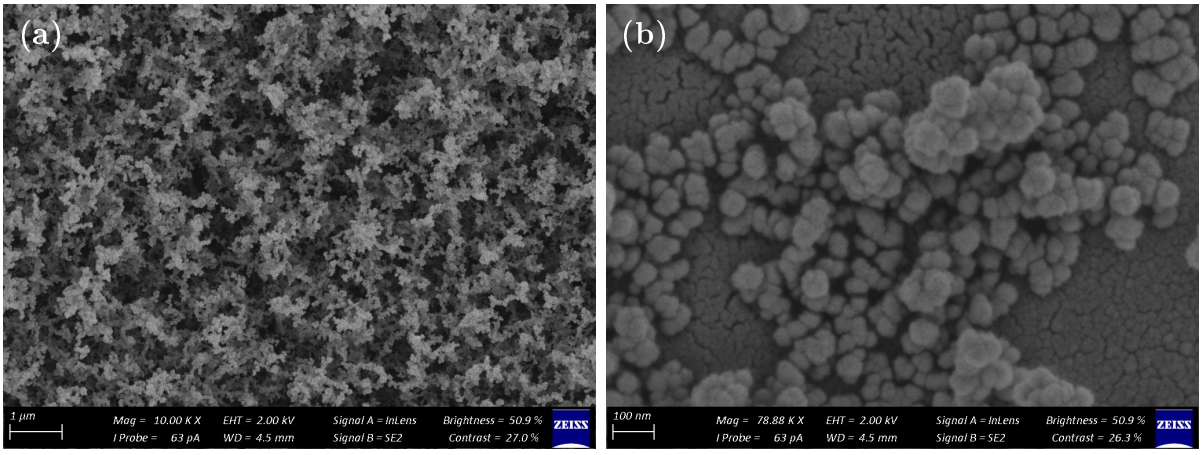

Figure 5.7: Soot coating HR-SEM images

5.4.2 XRD analysis of deposited candle soot

The results obtained from the XRD analysis of the soot sample are given in Figure 5.8. This pattern shows peaks that occur at roughly $2\theta = 25^{o}$, 43^{o} and 65^{o}. The peaks at 25^{o} and 43^{o} are related to the graphite lattice of carbon nanotubes [120, 121]. The broad peaks at 25^{o} and 43^{o} confirmed the amorphous nature of the deposited carbon nanoparticles [117]. This is also confirmed by the low intensity and small size of the 43^{o} peak, which indicates that the carbon nanomaterial present in the soot is amorphous [117].

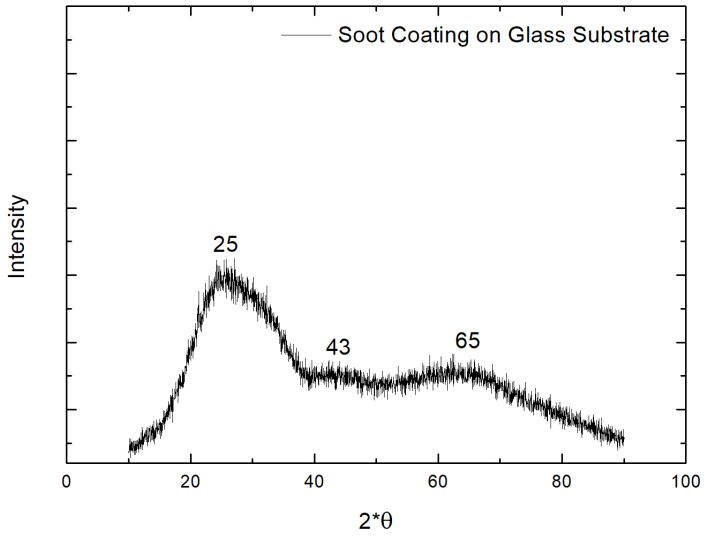

Figure 5.8: XRD analysis of a soot coating on a glass substrate

5.4.3 Raman analysis of deposited candle soot

The Raman spectrum of the deposited candle soot based solar absorber coating on a glass substrate is given in Figure 5.9. This spectrum shows two dominant bands at roughly 1323 cm^{-1} and 1559 cm^{-1}, which are the disorder, D- and graphite, G bands respectively. The D band, which resonates at around 1350 cm^{-1} in the spectra of carbon nanotubes, indicates the presence of amorphous carbon and nanotubes with surface defects [117–119, 122]. The 1323 cm^{-1} band is related to the vibrations that occur in the carbon atoms of disordered graphite, and the 1559 cm^{-1} band is associated to vibrations of sp^2-bonded carbon atoms, corresponding to a mode of graphite and the presence of carbon nano material, either in the form of nanotubes or nanospheres [117, 118].

The intensity ratio of the D and G peaks, I_D/I_G is calculated to be 0.8496. This is a parameter used to assess the quality of deposited carbon nanoparticles, where high ratios indicate high degrees of disorder. The high ratio observed, as well as the peaks present, indicate that the sample consists of amorphous carbon as graphite containing nanoparticles [117, 118].

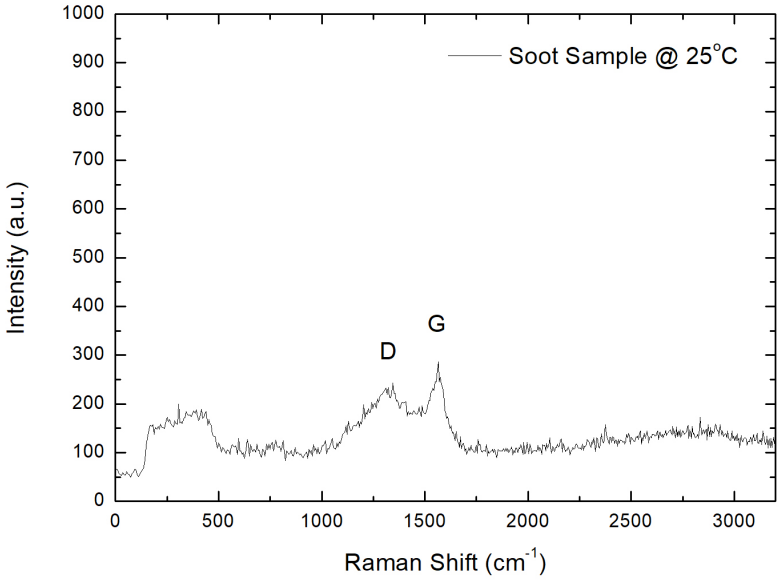

Figure 5.9: Raman spectrum of a soot coating at room temperature

5.4.4 HR-TEM analysis of deposited candle soot

Figure 5.10 shows the TEM and HR-TEM images that were taken of the sample at different magnification levels. It also includes a SAED pattern for the sample. These images confirmed the observations made from the HR-SEM images, that the soot particles consist of spherically shaped nanoparticles, many of which are agglomerated. These observed particle shapes have also been confirmed by previous studies [123, 124]. The figures were used to determine the PSD, given in Figure 5.11, which shows that the average particle size in the given sample is approximately 36 nm. These measured particle diameters agree with soot particles that have been previously studied that fall in the range of 20-40 nm [124]. The HR-TEM image of Figure 5.10(c) shows that the soot particles are stacked on each other in a sheet like structure, and this build-up of layers results in the dendritic pattern that can be seen in the low magnification SEM image of Figure 5.7(a). The SAED pattern, which appears in Figure 5.10(d), is a pattern that is coherent with samples that consist of amorphous material [125–128].

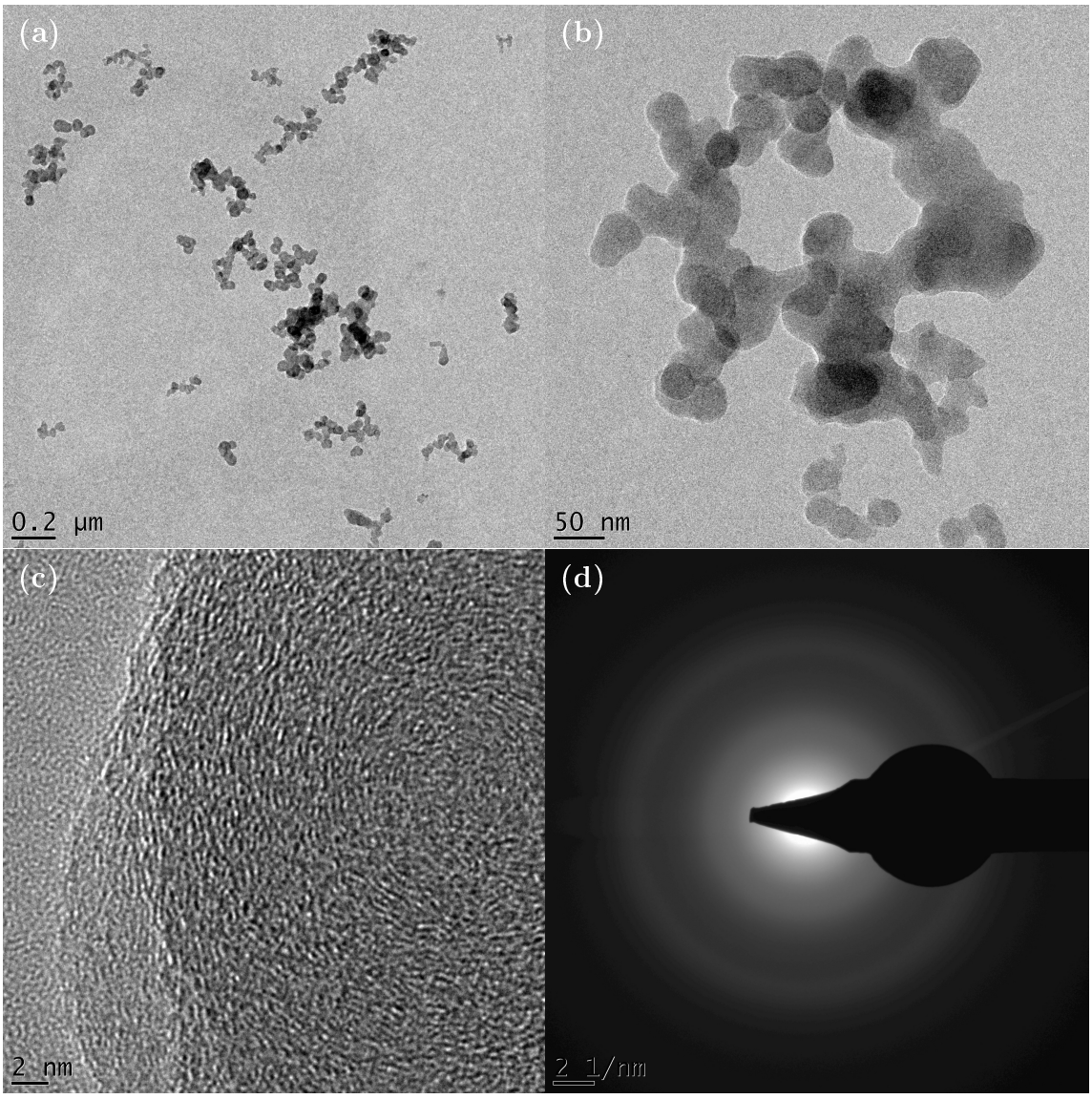

Figure 5.10: TEM, HR-TEM and SAED images of soot particles

The results of the EDS analysis done on the same soot coating sample is given in Figure 5.11. This confirms the speculated composition of carbon and oxygen in the sample, where carbon is the element with the highest count. The copper that is present in the EDS spectrum is a result of the carbon coated copper grid that is used in the TEM sample preparation process, which causes small additional peaks in carbon and copper.

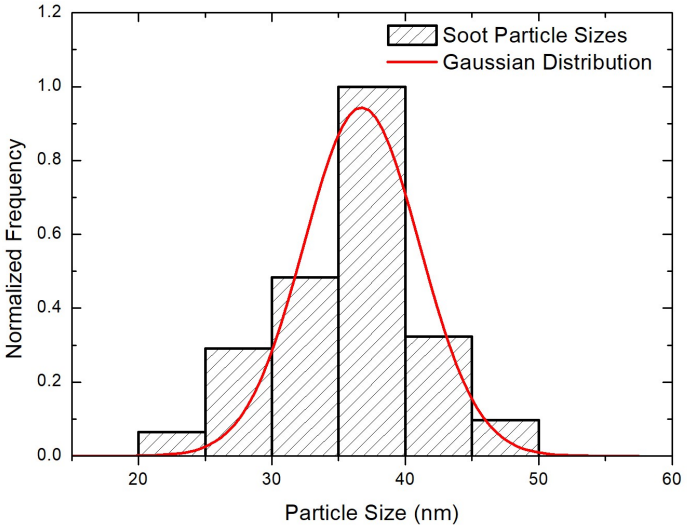

Figure 5.11: Soot coating PSD

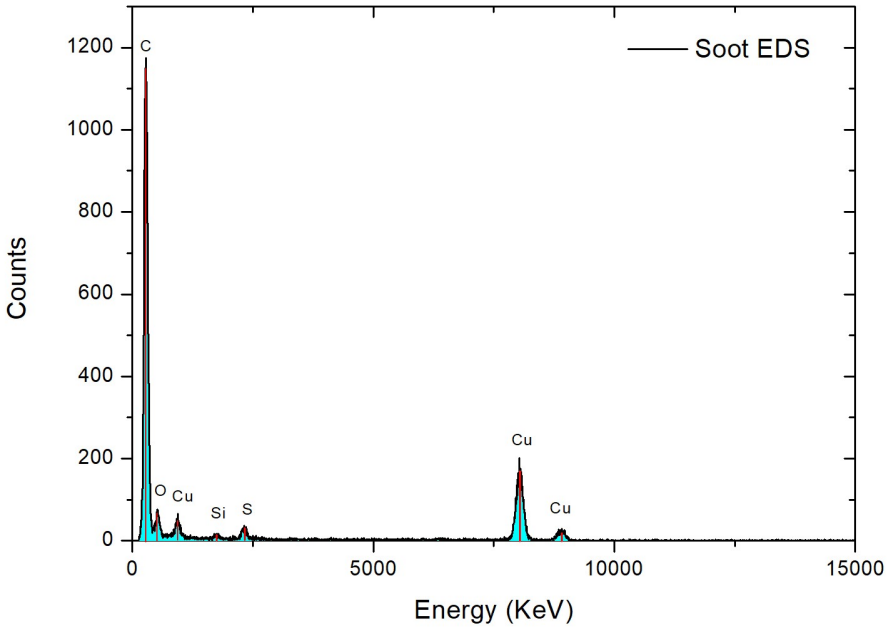

Figure 5.12: Soot coating EDS spectrum

5.4.5 Diffuse reflectance of soot sample

The diffuse reflectance of the soot samples was measured in the same manner as the commercial selective absorbers. The results are plotted in Figure 5.13. It is clear from the figure that soot samples have optical properties that are similar to a black body, and have a very low optical reflectance at all wavelengths in the measured spectrum. The measured reflectance peaks at only 2%, at a wavelength of 400 nm.

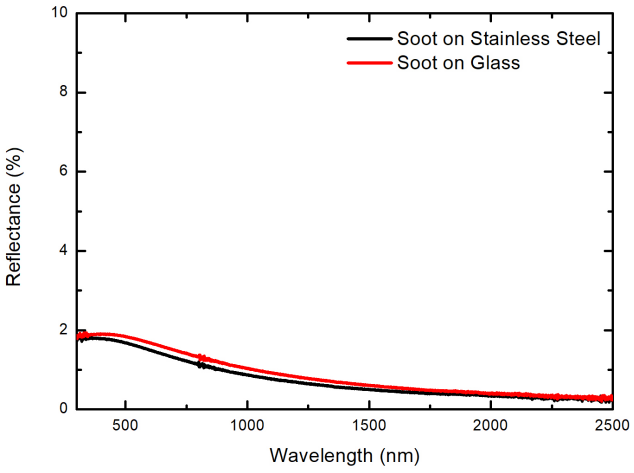

Figure 5.13: Measured diffuse reflectance of soot coating

The soot coating, because of its low reflectance at all wavelengths, would have a high total solar absorption as it has minimal reflection throughout the solar energy spectrum. The total solar absorption of these coatings are given in Table 5.3, but it is important to remember that although their solar absorption is high they will have a high thermal emissivity, as all energy in the IR region is also being absorbed.

Table 5.3: Calculated absorption of soot coating

Sample	Calculated solar absorption
Soot on glass	0.9866
Soot on Stainless Steel	0.9881

5.4.6 Discussion of deposited candle soot coating characterization results

The characterizations and investigations that were done on the deposited candle soot, which is to be used as a receiver tube solar absorber coating, gave some valuable insight about the material. Reflectance measurements showed that the material demonstrated the reflective properties of a black body type material, resulting in a high degree of solar absorption. The high absorption can be attributed to the pigmentation of the material, as well as the porosity of its dendritic structure, which can increase the absorptance of the coating through light trapping. The material was determined to be almost completely composed of a combination of oxygen and carbon, of which a large percentage is amorphous, as a result of the incomplete combustion of the candle flame. The carbon particles were found to be on the nano-scale, having an average particle size of approximately 36 nm. These particles were stacked on top of each other, which resulted in the dendritic surface structure of the material.

5.5 Black spray-paint characterization

This section includes the characterization that was done on the black spray-paint coating, which includes the measurement of its reflectivity and the calculation of its solar absorption.

5.5.1 Black spray-paint diffuse reflectance

The diffuse reflectance of the black spray-paint was measured using the same procedures as the soot and selective absorber samples. The measured reflectance of the spray-paint is shown in Figure 5.14, on the same axis as the reflectance of the soot coatings that are given in Figure 5.13. From these results it is evident that the spray-paint sample is slightly more reflective than the soot coating, with an average reflectance of roughly 3% over the spectrum. The sample is clearly non-selective and would thus, similarly to the soot sample, also absorb all wavelengths in the measured spectrum, including wavelengths in the IR region.

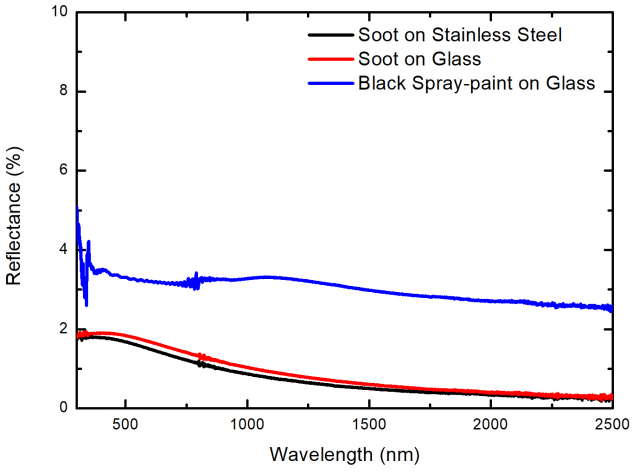

Figure 5.14: Measured diffuse reflectance of soot coating

The low reflectance of the black spray-paint over the measured UV-vis spectrum results in the sample having a high total solar absorption. The calculated absorption is given in Table 5.4. This is slightly less than the absorption that was calculated for the soot coating, and both samples display good solar absorptive properties but do not allow for any wavelength selectivity.

Table 5.4: Calculated absorption of black spray-paint coating

Sample	Calculated solar absorption
Black spray-paint on glass	0.9679

5.6 Chapter summary

This chapter contained the results of various characterizations that were conducted on a selective solar absorber, both flat and curved, a soot coating and of black spray-paint. It gave insight into the surface structures and optical properties of the different materials. Sections of the results presented in this chapter also appear in a research paper published by the author and presented at the AMRS Botswana conference in December 2017 (Appendix F). With a detailed understanding of the properties and characteristics of the receiver coating materials, more information and a better understanding can be drawn from the results obtained when using the materials in the system for testing.

Chapter 6

CSP milk pasteurizer performance results

This chapter presents the results that were obtained on three different days that the parabolic concentrator was tested, namely 12 March 2018, 20 March 2018 and 27 March 2018.

In the Cape Town Area, South Africa, where the system was tested, these dates occur during autumn. The first two days consisted of tests that were run only with water, to assess the heating ability of the CSP and to gauge roughly what the flow rate at these temperatures would be. On the final testing day, raw milk was used and the system's ability to pasteurize it was tested. Appendix E shows further details of the environmental conditions on the days of testing, these being the DNI in the area, air temperature and wind speed.

6.1 Test day 1 : 12 March 2018

Testing on day 1 was done using water as the HTF, and measurements were taken using all three of the receiver tube coatings, i.e. the selective solar absorber sheets, high-temperature black spray-paint and the soot coating. The inlet and outlet temperatures that were recorded during these tests are shown in Figures 6.1, 6.2 and 6.3 for each of the tube coatings. During the tests, which were all conducted between 12:30 and 14:00 to ensure optimal conditions, the system was kept directly aligned with the sun and was rotated as needed. The flow rate was also increased and decreased manually using the PWM controller to allow the output temperature to reach and be held at the desired values.

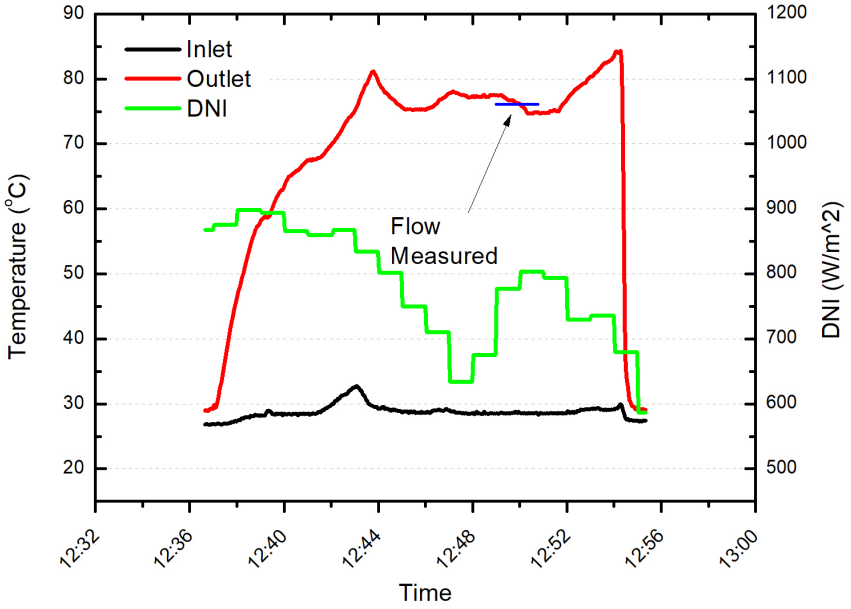

Figure 6.1: Water test 12-03 with selective absorber coating

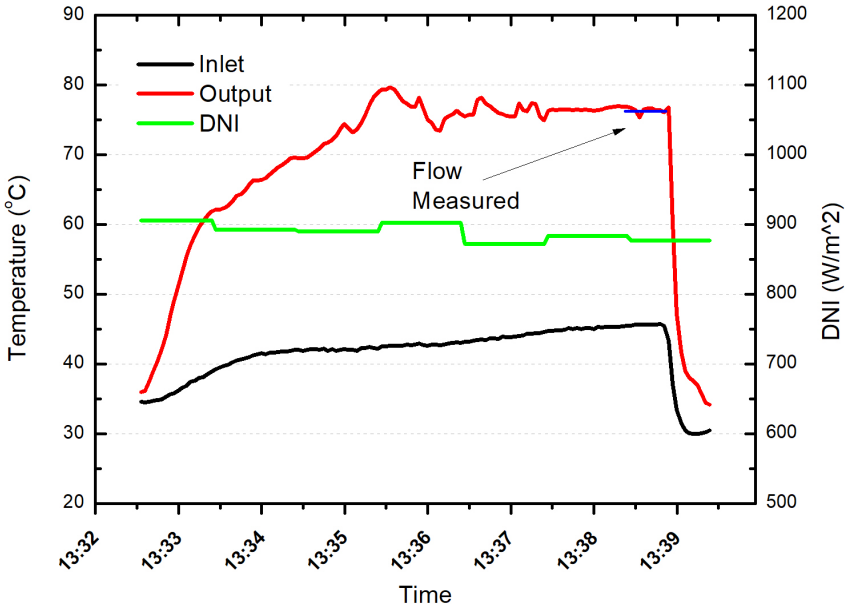

Figure 6.2: Water test 12-03 with black paint coating

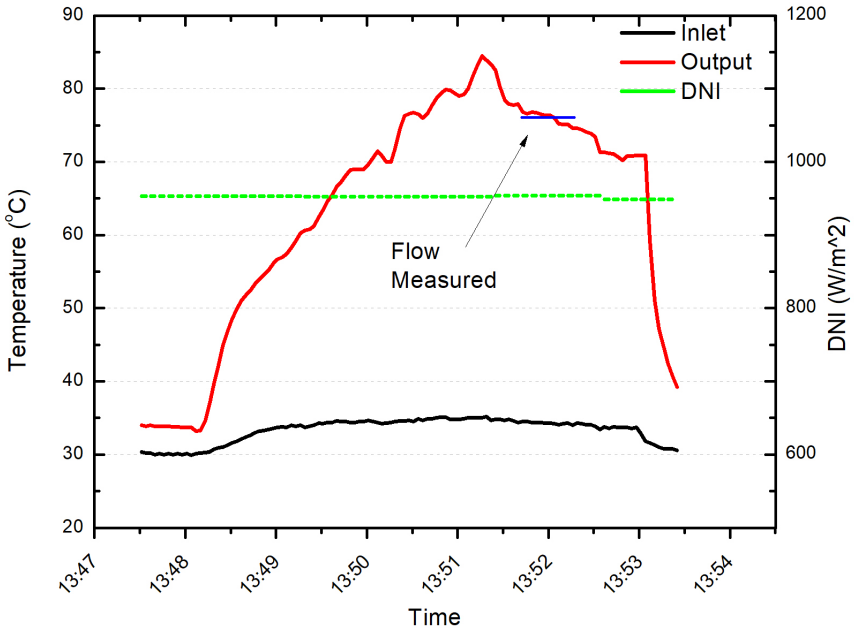

Figure 6.3: Water test 12-03 with soot coating

At the end of each measurement time period, while the output temperature was at or above the target temperature, the flow rate of the system was measured, this is indicated on each of the figures with a blue line. After each of the flow rates were measured, the test was concluded and the flow-rates were increased sharply, which flushed the heated fluid from the system and caused the visible steep drop in output temperature. The measured flow rates are given in Table 6.1.

Table 6.1: Measured flow rates during testing 12-03-2018

Absorber tube coating	Flow rate (L/hr)
Selective coating wrap	5.4135
Black spray paint	9.6
Soot coating	8.6746

From these tests it was clear that the system was able to function as desired. The necessary temperatures were achieved with ease and the flow rates were similar to those estimated in Appendix A. The flow rate of the system using the selective absorber wrap was, however, significantly less than the other two coatings. This could be attributed to either the poor heat transfer between the absorber sheets and the receiver tube, or the intermittent clouds that were partially present during that particular test. The average DNI and air temperature on this day of testing were 832.77 W/m^2 and 28.92 °C respectively.

6.2 Test day 2 : 20 March 2018

The test procedure that was used on Day 2 was similar to what was used on Day 1. Water was again used as the HTF, and testing was done between 12:45 and 13:45 for all three of the receiver tubes with different absorber coatings. The average DNI during the testing time was 1005.06 W/m^2 with an average air temperature of 20.64 °C. As was done in tests of Day 1, the input and output temperatures and the flow rates of the system with each receiver tube were recorded. Additionally, the maximum temperature that could be achieved by the system was also recorded. The maximum temperature was measured by reducing the flow rate of the pump to the minimum possible output, while still ensuring a flow. Figures 6.4, 6.5 and 6.6 display the results of the three tests done on that day.

The testing procedure consisted of starting the flow rate high, reducing it slowly until the target output temperature was reached and measuring the flow rate at this temperature. The flow rate was then increased to flush all hot water out of the system, and finally the flow rate was set to a minimum to observe the maximum temperature that could be reached. The minimum flow rate of the system was measured to be roughly 3.1718 L/hr, and it was at this flow rate that the maximum temperatures were measured. The maximum temperatures, as well as the period where flow was measured are also indicated in each of the figures that follow.

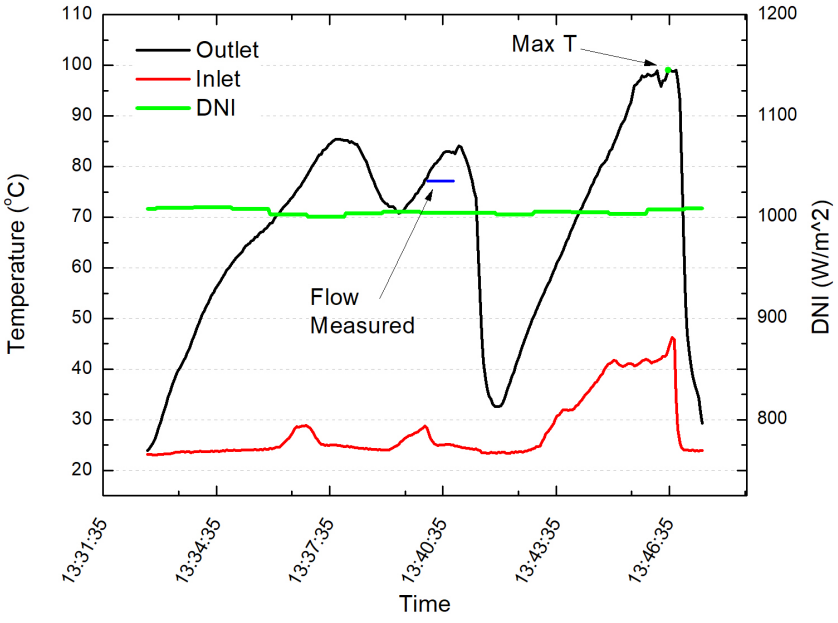

Figure 6.4: Water test 20-03 with selecting coating

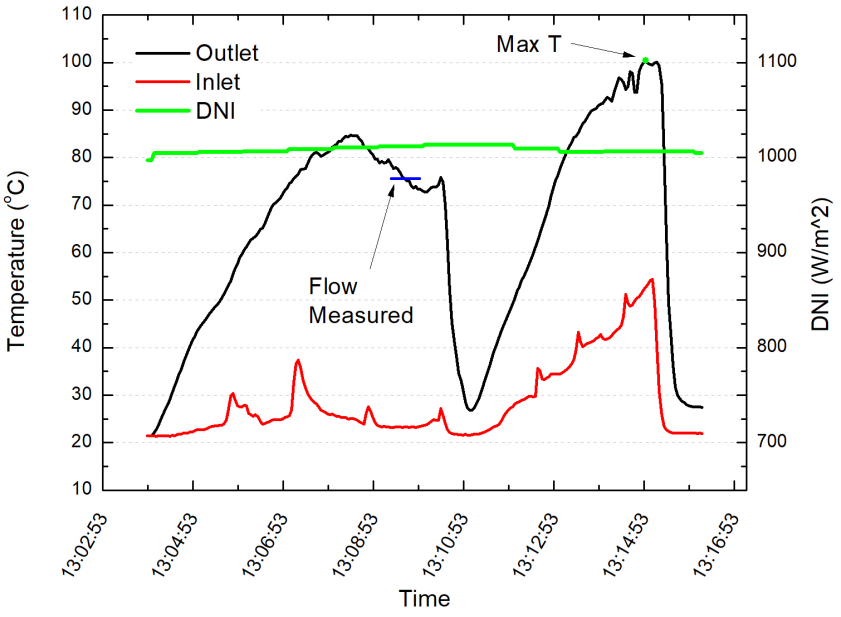

Figure 6.5: Water test 20-03 with black paint coating

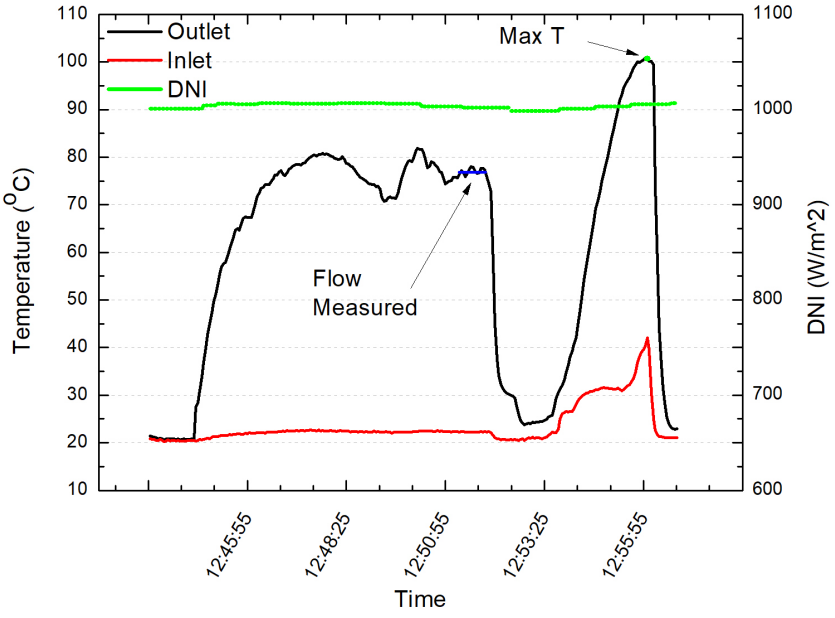

Figure 6.6: Water test 20-03 with soot coating

The measured flow rates and maximum temperatures that were recorded during these tests are given in Table 6.2.

Table 6.2: Measured flow rates during testing 20-03-2018

Absorber tube coating	Flow rate (L/hr)	Maximum T (°C @ 3.17 L/hr)
Selective coating wrap	10.4347	99.3
Black spray paint	9.4736	100.63
Soot coating	10.7462	100.07

The results obtained on this day of testing confirm those that were obtained on Day 1. The system's performance was almost identical to the first day, and the flow rates of each of the tubes coatings were all in the same range. The performance of the selective coating wrap was significantly better than on the first test day, which could be linked to the more consistent DNI over the test period. These tests also showed the full spectrum of the system's performance, and for each of the tubes used the system was capable of reaching a temperature of around 100 °C, well above what is necessary for pasteurization to occur.

6.3 Test day 3 : 27 March 2018

Test day 3, which was the 27th March, was the day that the system's ability to pasteurize milk was tested. The tests that were run on this day used only the soot coated receiver tube to obtain the results. Testing was started by using water as the HTF, until the system was correctly aligned and a flow rate had been reached where the output temperature was in the target range for pasteurization to occur (>75 °C). The source of fluid input was then transferred from a water supply to a raw milk supply. Once the water had been flushed from the system, samples of the milk at the output were taken at various different temperatures to determine if it had been successfully pasteurized. Only one sample was taken from the first test (shown in Figure 6.7). Shortly afterwards another test was conducted, results of which are given in Figure 6.8, during which several samples were taken of milk that had been processed. These samples were taken at various temperatures ranging from 64 °C to 100 °C to determine the temperatures at which the process was successful, and below which resulted in an ineffective pasteurization.

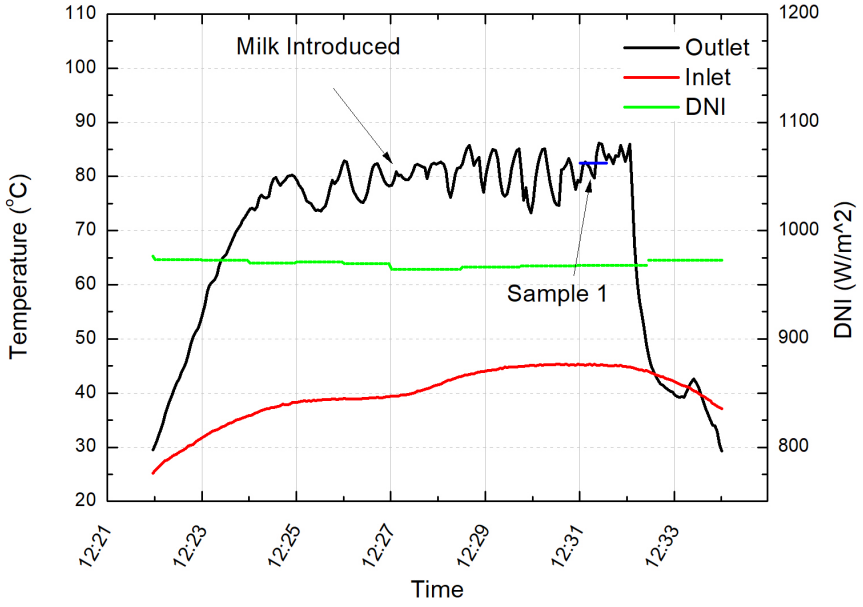

Figure 6.7: Milk test 1 with soot coating 27-03

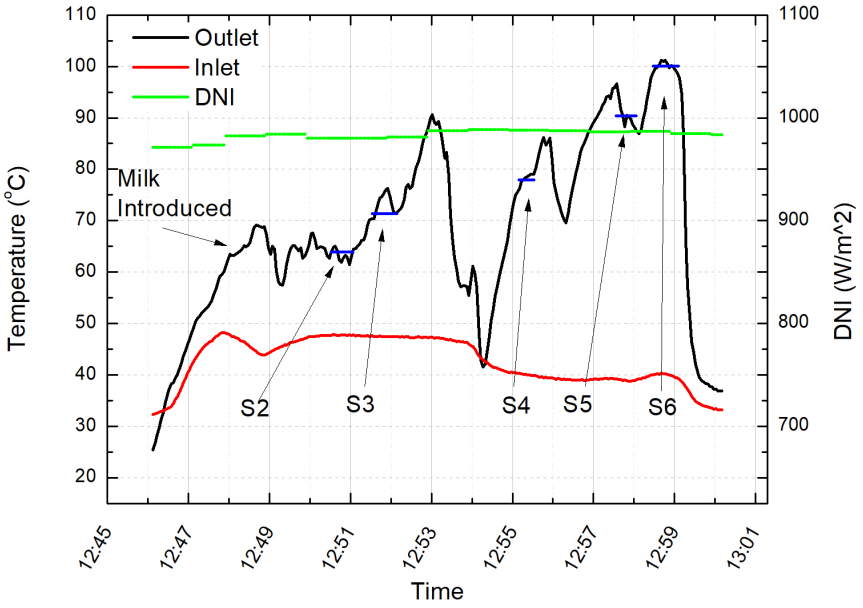

Figure 6.8: Milk test 2 with soot coating 27-03

The samples that were taken during the testing procedure were then tested using ALP pasteurization biostrips, to determine whether successful pasteurization had occurred. Table 6.3 shows the average temperatures at which the samples were taken, as well as the result of the biostrip tests. Figure 6.9 shows all of the strips and their respective samples. The strips that changed from blue to green indicate the presence of ALP, meaning that

the process was unsuccessful, and those that remained an unchanged colour blue were successfully pasteurized. Figure 6.10 shows a close up photo of the samples tested. Each sample was tested using two strips to ensure there was no false-positives or negatives, and were compared next to a strip that was tested on raw milk.

Table 6.3: Description of milk samples taken 27-03

Temperature reached °C	Sample number	Pasteurized True/False
Raw	Raw	False
64	S2	False
73	S3	False
78	S4	True
82	S1	True
90	S5	True
100	S6	True

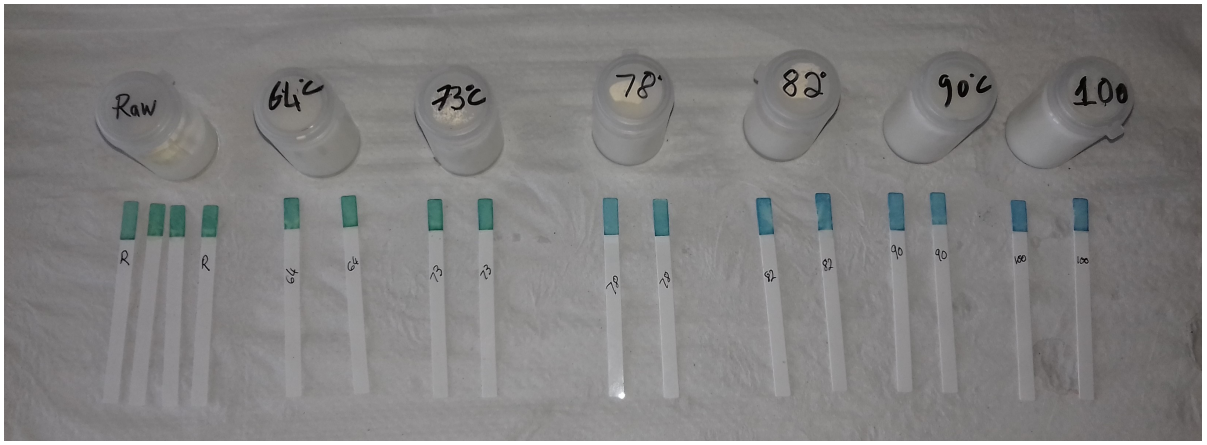

Figure 6.9: Milk pasteurization test strips and samples

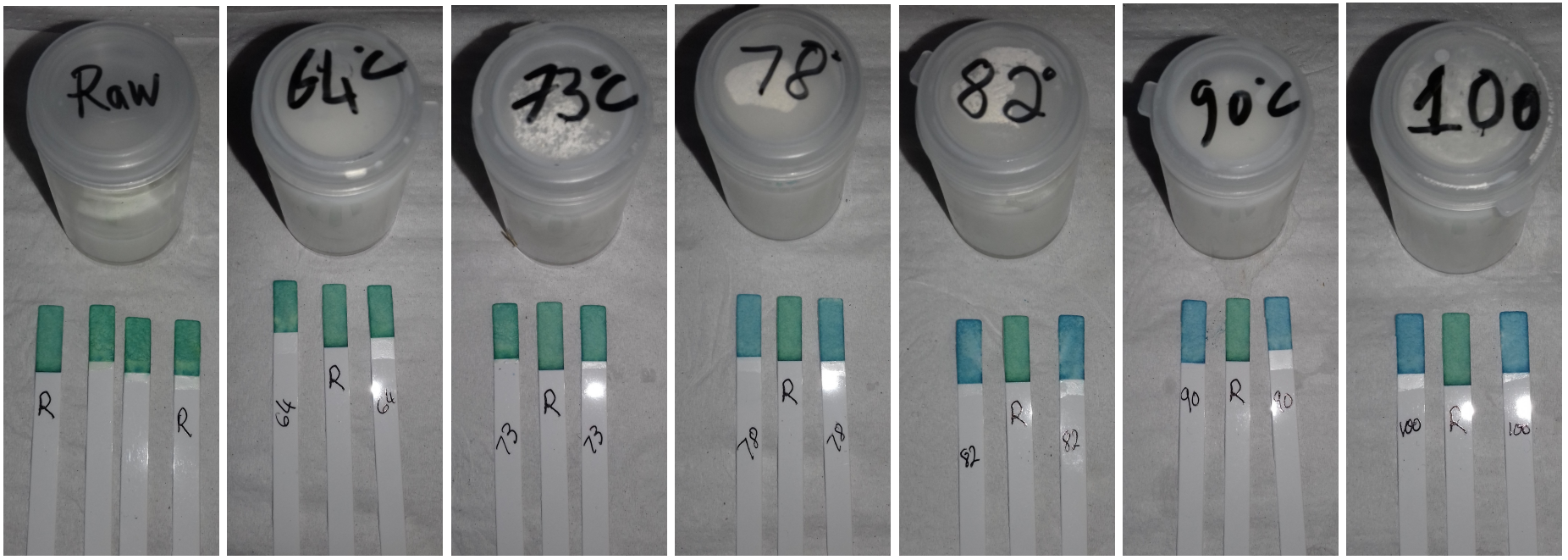

(a) Raw milk (b) 64 °C sample (c) 73 °C sample (d) 78 °C sample (e) 82 °C sample (f) 90 °C sample (g) 100 °C sample

Figure 6.10: Milk pasteurization testing biostrips

6.4 System efficiency

The solar concentrating system essentially had three main aims from a performance perspective. The first was to be able to concentrate all solar energy that falls on the aperture correctly. The second was to be able to capture and absorb this energy into the receiver tube. And thirdly, it needed to be able to transfer the heat to a HTF as effectively as possible. This was to be done as well as reasonably possible, while still utilizing a relatively simple design and basic materials. By producing output temperatures in and above the desired range, the system was ultimately able successfully achieve these performance aims. To measure the degree of which these aims were met, the overall efficiency of the collector is an important metric to consider. It is dependant on each of the performance aims and it gives a good indication of the overall abilities of the system. Using the parameters given in Table 6.4, which are measurements taken from Day 2 of testing (20 March 2018), the approximate efficiency of the system with each receiver tube coating was calculated, using (3.9), and are given in Table 6.5.

Table 6.4: System efficiency parameters

Coating	Test Time (hh:mm:ss)	Flow Rate (L/hr)	DNI (W/m^2)	Tin (°C)	Tout (°C)
Selective	13:40:05 - 13:40:35	10.4347	1004	26.5	80
Black	13:09:25 - 13:09:55	9.4736	1008	23.5	76
Soot	12:51:25 - 12:51:55	10.746	999	23.1	77

Table 6.5: System efficiency

Coating	Efficiency (%)
Selective	53.768
Black	47.713
Soot	56.065

The calculated efficiency of the system appear to be relatively high compared to CSP plants, which achieve solar-to-electric efficiencies of roughly 15-20% [129]. This, however, is purely because this system does not involve the transportation, HTF storage, and an electrical generation process. The efficiency of this system is also calculated only over the heating area of the system. This efficiency can still be improved by reducing losses occurring in the system, such as concentrating losses caused my imperfections on the reflective sheet, and errors caused by the non-ideal receiver tube coating.

6.5 Chapter summary

This chapter showed the results that were obtained when the parabolic concentrator was tested, both with water and with raw milk as a primary HTF. The system was able to reach temperatures of above 72 °C with ease, and showed the ability to even reach up to 100 °C at a minimum flow rate. The results show that the system successfully heated milk to a range of temperatures, and sampling at these temperatures confirmed that pasteurization had been successful when output temperatures were above 78 °C.

Chapter 7

Conclusions and recommendations

7.1 Conclusion

A small scale CSP device was successfully designed and tested during the course of this project. It was able to reach the temperatures which are necessary for the pasteurization of raw milk to occur, and was shown to be able to successfully perform pasteurization.

The motivation behind this project was to develop a system that would be able to improve the standard of living for people in rural areas, by providing them with a sustainable means to remove bacteria from their milk and simultaneously increase its lifespan. Such a system allows for the reduction of illness linked to the consumption of raw milk, as well as respiratory illnesses linked to the use of biomass fuels for heating and cooking. The use of solar energy for cooking allows the users to spend less on the fuels used for cooking and ultimately save costs in the long run.

To be a viable system for the pasteurization of raw milk, the CSP system would need to be able to heat milk from room temperature to a pasteurization temperature and hold it there for a certain length of time. To achieve the highest possible throughput the system was designed to use continuous flow pasteurization instead of batch pasteurization. The minimum temperature-time combination requirement of this method is 72 °C for 15 s, with decreasing time for higher temperatures. The system would also need to be able to reach the necessary temperature in different solar conditions and be able to stay correctly aligned throughout the day.

After determining, through research, that such a device could be very beneficial for those in rural areas, the design was addressed. Key aspects of the system's design that were considered were ease of operation, overall weight and the use of low cost, long lasting and availability of materials. To ensure that the system could safely process products intended for human consumption, the materials that came into contact with the milk also needed to be non-contaminating and resistant to the cleaning procedures. Taking these factors into account, the materials chosen to make up the majority of the device's structure were aluminium and mild steel. The receiver tube, as one of the only components that interacts with the milk, was chosen to be stainless steel, as is standard practice in the dairy industry. The system was designed with an aperture area of 1.2 m^2 and a focal length of 0.225 m, and using a receiver tube with an outer diameter of 19.05 mm the systems concentration ratio was calculated to be 20.051.

To keep operation of the system as simple as possible, manual tracking was incorporated instead of using an automatic system, and by including a sun aiming pin in the design it is possible to tell at all times of operation whether the system correctly aligned. In future, the device can however be modified to accommodate an automatic tracking system without a significant amount of alteration needed. The system was also designed to facilitate the replacement of components that contribute significantly to the the overall device efficiency. In this system, they were the reflector sheet and receiver tube. By doing this, if the components become damaged and need replacement, it can be done with ease. It also allows for alternative materials to be tested with the device, and along with the reflector sheet, the receiver tube could be substituted for parts that are the same size but use different materials or coatings. This feature was used extensively in the measurement of the performance of different absorber tube coatings, where on two of the three test days, three different receiver tubes were tested in quick succession.

The performance of a concentrating system is largely dependant on its ability to concentrate and absorb solar energy. For this reason the reflective sheet and receiver tube absorber coating were important aspects of the design. During the course of this project, a large interest was taken in the properties, structure and performance of the solar absorber coatings. The three types of coatings used were a commercial selective solar absorber, black paint and candle soot. Several characterization techniques were used to gain further insight about these materials and how they behaved. The initial characterizations were done on the selective solar absorber coating. This was done to determine if any degradation would occur if it was heated to temperatures up to 500 °C, and if rolling the material into a tube would cause a reduction in performance.

Various changes were observed with the flat commercial selective absorbers samples, when heated through a range of temperatures up to 500 °C, for one hour each. One of which showed that the optical performance of the coating began to experience degradation after being exposed to temperatures above and including 300 °C. SEM images were taken and the PSD of the surface were recorded to understand the process that was causing the performance reduction. It was observed that with increasing temperatures, the average particle size of the samples increased. The phenomena that was linked to the particle agglomeration, increase in average size, and reduction in optical performance was determined to be solid-state dewetting.

The commercial selective absorber coatings were then further tested, to see if the action of bending the sheets would have any effect on its optical properties. Flat samples of the same material used previously were thus bent into a tubular shape, and heated using the same process. The reflectance of the tubular samples was then measured and used to calculate solar absorption. Upon comparing the results to the flat samples, it was evident that there was no reduction in performance caused by the bending process.

The next receiver tube coating that was studied was the candle soot coating, this was identified as a cost free way to achieve a black surface coating on the receiver tube which could be accessible to all. It was important, for having complete understanding of the system, to determine what the optical properties of this coating were, as well as the surface structure and chemical composition. By measuring the reflectance of a soot coated sample, it was evident that it behaved in a similar manner to a black-body and

had a very low reflectance and therefore high absorption. This meant that a coating such as this would have a relatively high solar absorption, while simultaneously also have high thermal emissivity.

To gain further insight into the nature of the soot coating, characterization was done using various different technologies. HR-SEM, XRD, Raman and HR-TEM were all used to obtain more information about the coating. The images captured with the HR-SEM revealed that the surface structure of the material could also play a role in its absorptive properties because of the porosity of its dendritic structure, as well as its black pigmentation. The particles were observed to be stacked on top of each other to produce this structure, and they were found to be, on average, roughly 36 nm in size. The material composition was almost predominantly composed of oxygen and carbon, most of which was amorphous, that formed as a result of the incomplete combustion of the candle flame as it came into contact with the substrate.

The third type of receiver tube coating that was used in the tests was a high-temperature black spray-paint, another low cost alternative to selective solar absorbers. This coating also exhibited properties of a black body absorber. However, the slightly higher reflectivity resulted in a solar absorption that was marginally less than the soot absorber coating.

With a better understanding of the composition and properties of the different receiver tube solar absorber coatings, each of the three coatings were applied to their own individual receiver tube. This allowed for the performance of the different coatings to be tested and compared. The CSP device was tested on three different days in March 2018, two days of which involved testing with all three coatings and the last day with only the soot coating. Testing with the three different coatings was done using water as a HTF instead of milk, as this allowed for the receiver tubes to be interchanged quickly, without the need for the cleaning steps that are required with milk processing. The first two days of testing showed that the system, with each of the different solar absorber coatings, was able to reach the temperatures that are necessary for milk pasteurization, while maintaining a reasonable flow rate. The results of the testing on the second day (20 March) confirmed the results of the first test day, and were subsequently used to calculate the approximate efficiency of the system when using each of the solar absorber coatings. Of the three tests, the soot coating allowed the system to obtain the highest solar to heat conversion efficiency of 56.065%.

Although the candle soot had a slightly higher absorptivity, lower cost, and was able to achieve the highest efficiency, the high temperature spray-paint may be more practical and durable alternative in the long run. Because the candle soot is essentially a thin coating over the tube that is not stuck in any way, it is prone to being smudged or wiped off when it comes into contact with the operator or other objects; this is something that was noticed when handling the tube during testing and operation. This could result in a time consuming process each time the tube is used, consisting of checks and touch-ups to ensure the coating is uniform and hasn't been wiped off any sections of the tube. For these reasons, it can be thought of as a sensible sacrifice in performance for a substantial gain in durability.

The ability of the system to pasteurize raw milk was tested on March 27, 2018, using the candle soot receiver as the primary tube coating. Testing on this day was done by first using water as a HTF, until a stable flow rate had been reached in the desired temperature range, and then switching the input source of liquid to raw milk. Samples were taken of the heated milk at various temperature and flow rate combinations. This was done to gain an overview of the conditions at which pasteurization would be successful using the device. These samples revealed that output temperatures of 73 °C and below resulted in the milk not being successfully pasteurized, this is likely because the temperature would drop after leaving the receiver tube, resulting in the milk not held at the necessary temperatures for long enough. Samples taken where the measured temperature at the output was 78 °C and above, were, however, found to be successfully pasteurized. This was tested and confirmed using pasteurization biostrips.

Ultimately, the system was able to produce the desired results, and successfully reached the temperatures necessary for milk pasteurization, allowing it to successfully pasteurize raw milk using concentrated solar energy. The device has the potential to greatly assist people in rural areas who are susceptible to milk related illness, and people who rely on milk as a primary source of nutrition or income. It will allow them to remove harmful bacteria from the milk that they consume, making it safer to drink and also allowing it to be stored for longer periods of time.

7.2 Recommendations

This device has only undergone its first iteration, and there are still various additional systems that can be included, or existing components that can be improved. By refining the existing design to maximise the optical efficiency and heat absorption of the device, the overall performance can be enhanced. In order to do this, a detailed study of the device's optical performance would need to be conducted to determine the exact extent of optical errors that occur. By doing this, the source of the greatest errors can be identified and negated, improving the device's efficiency.

The device could facilitate the incorporation of an automatic tracking system to replace the manual system. Although this may overcomplicate the device for use in rural areas, it could be useful should the device be used for other applications. This can be done by using small solar panels mounted on the end of the device, to both detect misalignment and to power a small motor to rotate the device. These panels, if large enough, can also be used to provide the energy necessary to power the pump system that the device utilizes. This would allow for the device to be completely free-standing and be able to function without any dependence on an electrical power supply.

Another feature that can be integrated into the design would be an automatic flow control system. The system could utilise the measured output temperature to increase or decrease the flow rate automatically to protect against sub-optimal temperatures that result in incomplete pasteurization. Alternatively, if the upgraded device includes the addition of small solar panels, it can pre-emptively alter the flow rate based on the amount of solar energy the panels are able to detect.

To safeguard against incomplete pasteurization there are various other components that could be incorporated into the design, an example of which could be a temperature operated valves to ensure the output temperature is kept above the minimum required. For rural applications, where these more advanced components may need to be avoided, it would still be useful to include measurement equipment that would facilitate optimal performance and operation of the device. An example of such measurement equipment could be a large colour-coded thermometer to warn the operator when the output temperature is dropping to a level where pasteurization may be compromised, and guide them into adjusting the correct components to raise the temperature back to a suitable level of safety.

7.2.1 Potential applications

Listed below are several potential applications of the parabolic trough that was built, which became apparent during the process of design, building and testing of the device.

- **Water pasteurization -** This is a process that would be similar to milk pasteurization in function and procedure, with slight variations in required temperatures and process times. Water pasteurization would not result in the deposition of milk particles on the inside of the tube and could therefore use copper pipes and fittings, which would have much higher heat conductivity, to increase heat transfer and efficiency of the system. This is something which could also be extremely beneficial to people living in poorer communities that rely on wells or rivers as their primary sources of water, these can be home to various bacteria that can cause illness.

- **Solar cooking -** As is done with various other solar cooking devices, the heat that is obtained using this device could be used as a means to cook food. This could be done using a different HTF and circulating the heated fluid around a cooking pot or similar receptacle.

- **Further studies -** In the duration of the project, working among other scientists at the Material Research Department at iThemba Labs, it became clear that the device could facilitate many different paths of study. Because the device was designed to have interchangeable components, it would allow for testing of different receiver tubes, absorber coatings, reflective sheets and heat transfer fluids.

Appendices

Appendix A

Design calculations

This Appendix highlights the main calculations that were used to determine the dimensions and aspects of the parabolic trough system.

A.1 Acceptance angle, minimum receiver diameter

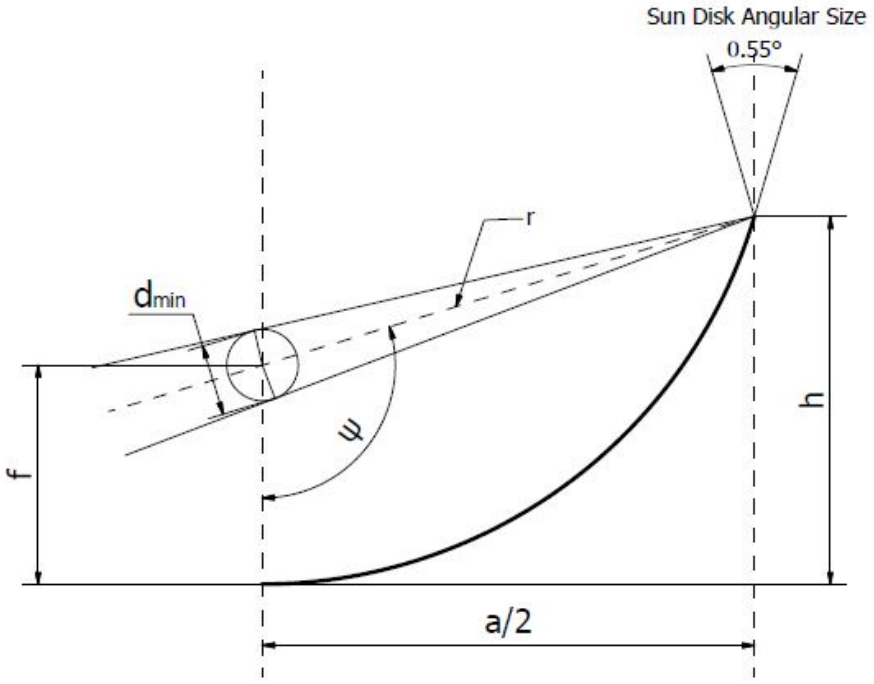

Figure A.1: Variable for calculating minimum receiver tube size calculatio

The length of r is chosen to be the furthest point on the parabola from the focal point, this will give an indication of the largest possible range of solar energy that can be expected on the structure.

$$r = \sqrt{(h-f)^2 + (a/2)^2} \tag{A.1}$$

$$\frac{d_{min}}{2} = r \times \tan(\frac{0.55^{o}}{2}) \tag{A.2}$$

A.2 Design parameters and flow estimation

The following calculations cover the design parameters that were used in the system, as well as a rough estimation of the solar conditions and necessary flow rates. These estimated flow rates were used to assist in the selection of a pump for the system.

13 Apr 2018 12:42:15 - Flow Calculations.sm

Design of a Parabolic Solar Trough

JG Mallett

Calculations based on methods shown in Gunther et. al, n.d. and Stine and Geyer, 2001.

Parabolic Solar Trough Design Parameters

$f := 225\ mm$ Parabola focal length

$W_a := 1200\ mm$ Arpeture Width

$l := 1000\ mm$ Trough Length $h := 400\ mm$

$d_o := 19.05\ mm$ Absorber outer diameter

$\beta := 2\ deg$ Acceptance Angle "Most commercial PTC designs have acceptance angles, of 1-2°, with geometric concentration ratios of 20 to 30."

Concentration Ratio:

$$Cg := \frac{W_a}{\pi \cdot d_o} = 20.051$$

"Concentration ratio is usually about 25, although, theoretically, the maximum is on the order of 70".

Estimated Optical Loss Parameters:

$\rho := 0.68$ *Reflectivity* This value is of a Polished Stainless steel

$\alpha := 0.8$ *Absorptivity* Estimated value assuming a non-ideal solar absorber

Design Calculations:

Aperture Area

$$A_a := W_a \cdot l = 1.2\ m^2$$

Mirror Surface Area:

$$A_{surface\_reflector} := l \cdot \left(\frac{W_a}{2} \cdot \sqrt{1 + \frac{W_a^2}{16 \cdot f^2}} + 2 \cdot f \cdot \ln\left(\frac{W_a}{4 \cdot f} + \sqrt{1 + \frac{W_a^2}{16 \cdot f^2}} \right) \right) = 1.4944\ m^2$$

Rim Angle:

$$\Psi := \operatorname{atan}\left(\frac{1}{\left(\frac{W_a}{8 \cdot h}\right) - \left(\frac{2 \cdot h}{W_a}\right)} \right) = -73.7398\ deg$$

$$180\ deg + \Psi = 106.2602\ deg$$

"Usually rim angles are in the range 70°-110°. Smaller rim angles are not advised because they reduce aperture surface"

13 Apr 2018 12:42:15 - Flow Calculations.sm

Flow Rate Estimation

Receiver_Tube_parameters:

$pipelength := 1\ m$

$pipethickness := 1.6\ mm$

$Pipe\_surfaceA := 2 \cdot \pi \cdot \frac{d_o}{2} \cdot pipelength = 0.0598\ m^2$

$d_o = 19.05\ mm$

$d_i := d_o - 2 \cdot pipethickness = 15.85\ mm$

Estimated Solar operating conditions:

$q_{dot\_solar\_min} := 500\ \frac{W}{m^2}$ Estimated Minimum DNI condition

$q_{dot\_solar\_max} := 900\ \frac{W}{m^2}$ Estimated Maximum DNI condition

Esimtated solar energy concentrated on pipe, taking into account the reflectivity and absorptivity of the mirror and tube:

$q_{dot\_onPIPE\_min} := q_{dot\_solar\_min} \cdot Cg \cdot \rho \cdot \alpha = 5453.8765\ \frac{W}{m^2}$

$q_{dot\_onPIPE\_max} := q_{dot\_solar\_max} \cdot Cg \cdot \rho \cdot \alpha = 9816.9777\ \frac{W}{m^2}$

Milk Properties

$T_{in} := 25\ °C$

$\rho_{milk} := 1030\ \frac{kg}{m^3}$

$C_{p\_milk} := 3.93\ \frac{kJ}{kg\ K}$

$V_{dot\_milk} := 9\ \frac{L}{hr}$

$m_{dot\_milk} := V_{dot\_milk} \cdot \rho_{milk} = 0.0026\ \frac{kg}{s}$

$vel_{milk} := \frac{V_{dot\_milk}}{\pi \cdot \left(\frac{d_i}{2}\right)^2} = 0.0127\ \frac{m}{s}$

$T_{exit\_max} := T_{in} + \frac{q_{dot\_onPIPE\_max} \cdot Pipe\_surfaceA}{m_{dot\_milk} \cdot C_{p\_milk}} = 83.0568\ °C$

$T_{exit\_min} := T_{in} + \frac{q_{dot\_onPIPE\_min} \cdot Pipe\_surfaceA}{m_{dot\_milk} \cdot C_{p\_milk}} = 57.2538\ °C$

$time\_totalintube := \frac{pipelength}{vel_{milk}} = 78.9239\ s$

Equivalent Flow rates:

$V_{dot\_milk} = 150\ \frac{mL}{min}$

$V_{dot\_milk} = 0.009\ \frac{m^3}{hr}$

$V_{dot\_milk} = 0.0396\ \frac{gal}{min}$

$V_{dot\_milk} = 2.3775\ \frac{gal}{hr}$

This is to calculate at what point inside the tube it will reach 72deg and how long it wi stay at, or higher than this temperature.

$T_{exit\_72} := 72\ °C$

At Maximum estimated solar conditions and flow rate of 9L/hr:

$$pipelength72deg\_max := \frac{\left(T_{exit\_72} - T_{in}\right) \cdot m_{dot\_milk} \cdot C_{p\_milk}}{q_{dot\_onPIPE\_max}} = 0.8096\ m$$

$$time\_above72 := \frac{pipelength - pipelength72deg\_max}{vel_{milk}} = 15.0309\ s$$

At Minimum estimated solar conditions and flow rate of 9L/hr:

$$pipelength72deg\_min := \frac{\left(T_{exit\_72} - T_{in}\right) \cdot m_{dot\_milk} \cdot C_{p\_milk}}{q_{dot\_onPIPE\_min}} = 1.4572\ m$$

$$time\_above72\_min := \frac{pipelength - pipelength72deg\_min}{vel_{milk}} = -36.0836\ s$$

So changing the flow rate for less solar energy:

$V_{dot\_milk} := 5.5\ \frac{L}{hr}$

$m_{dot\_milk} := V_{dot\_milk} \cdot \rho_{milk} = 0.0016\ \frac{kg}{s}$

$$vel_{milk} := \frac{V_{dot\_milk}}{\pi \cdot \left(\frac{d_i}{2}\right)^2} = 0.0077\ \frac{m}{s}$$

$$T_{exit\_min} := T_{in} + \frac{q_{dot\_onPIPE\_min} \cdot Pipe\_surfaceA}{m_{dot\_milk} \cdot C_{p\_milk}} = 77.7789\ °C$$

$$pipelength72deg\_min := \frac{\left(T_{exit\_72} - T_{in}\right) \cdot m_{dot\_milk} \cdot C_{p\_milk}}{q_{dot\_onPIPE\_min}} = 0.8905\ m$$

$$time\_above72\_min := \frac{pipelength - pipelength72deg\_min}{vel_{milk}} = 14.1407\ s$$

So theoretically, flow rates between 5 and 10 L/hr will be ideal for milk pasteurization for a DNI between 500 and 900 W/m^2. This range can be increased to 3-12 L/hr to ensure that majority of solar conditions will be able to perform the task correctly.

Appendix B

CAD files

This appendix contains the main assemblies of the parabolic trough system. An additional drawing pack is provided with this document containing the drawings for all parts.

IF IN DOUBT ASK

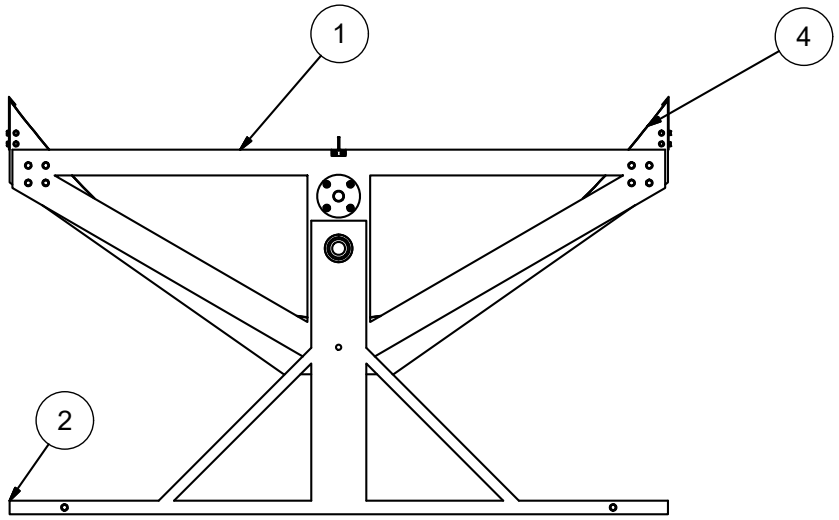

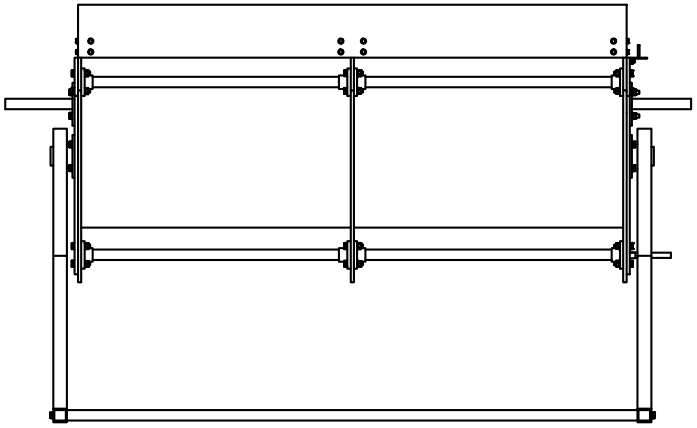

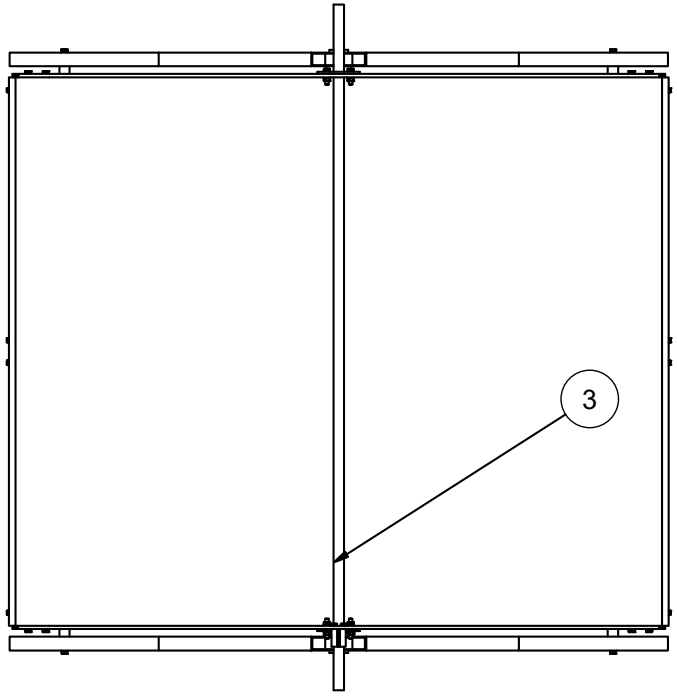

A (1 : 20)

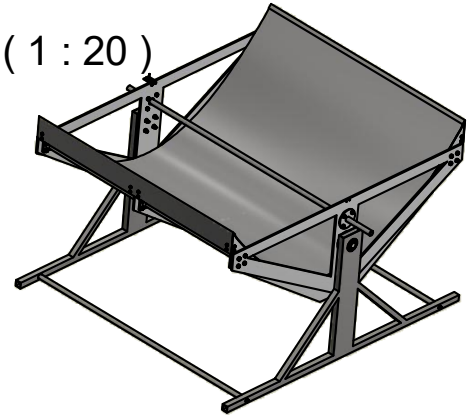

Parts List			
4	Reflector Sheet	1	SEE DRAWING (PSR-P14)
3	Receiver Tube	1	SEE DRAWING (PSR-P13)
2	Frame Sub-Assembly	1	SEE DRAWING (PSR-A-02)
1	Rotating body Sub-Assembly	1	SEE DRAWING (PSR-A-01)
ITEM	**BESKRYWING**	**AANTAL**	**MATERIAAL / SPESIFIKASIES**

97

APPENDIX B. CAD FILES

UNIVERSITEIT VAN STELLENBOSCH

STUDENTE No. 17597099	**TEKENAAR** JG MALLETT	**NAGESIEN**	**SKAAL OP A3** =1:10 **MATE IN** mm	**TITEL:** FULL ASSEMBLY	
			DATUM 21-03-2017	**VEL No.** 1 **VAN** 2 **VELLE**	**No.** PSR-A-00

IF IN DOUBT ASK

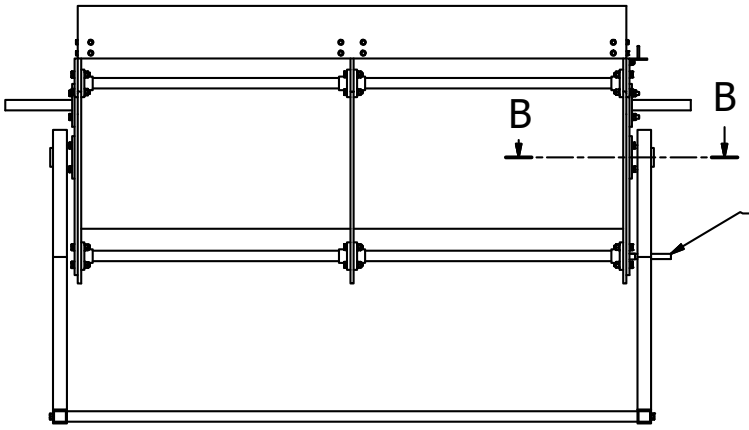

B-B (1 : 10)

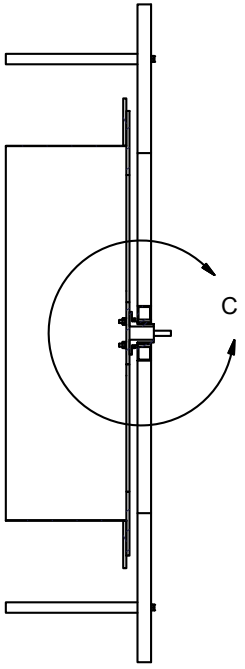

C (1 : 2)

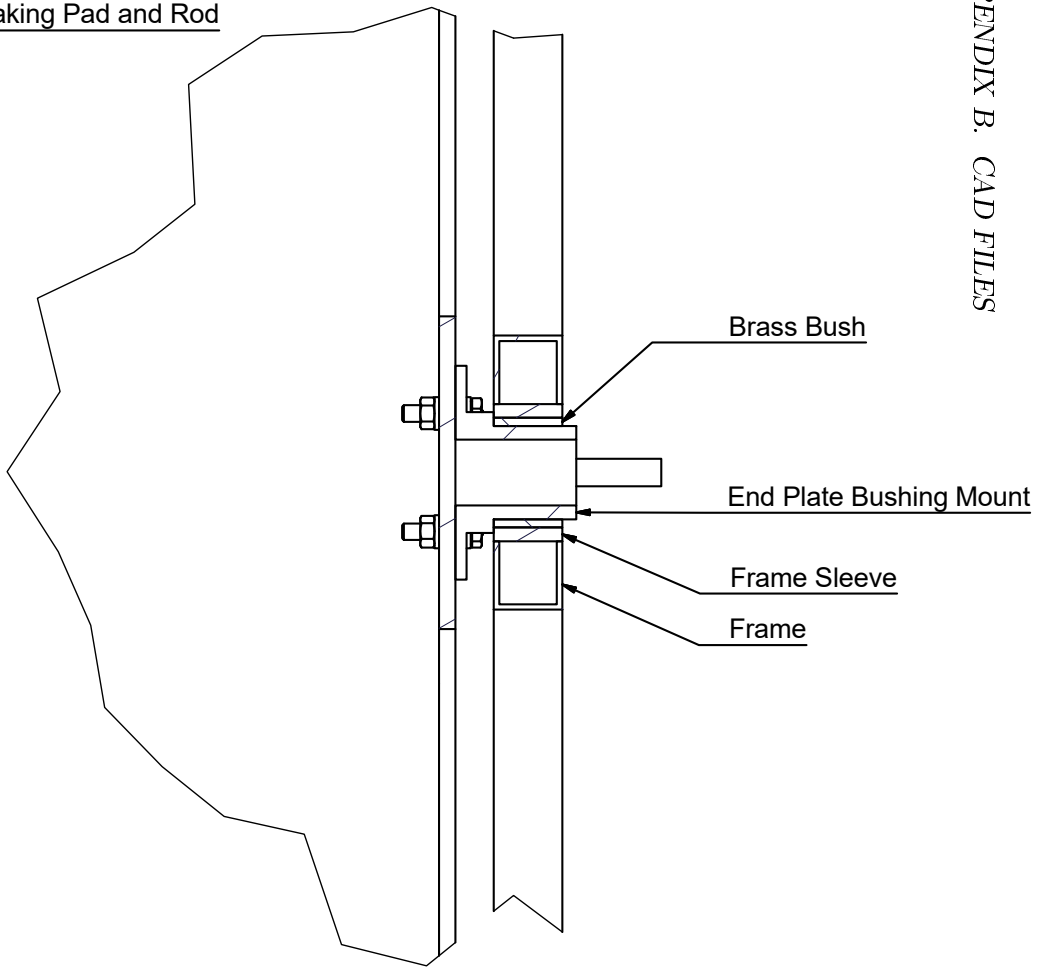

APPENDIX B. CAD FILES

ITEM	BESKRYWING	AANTAL	MATERIAAL / SPESIFIKASIES

98

UNIVERSITEIT VAN STELLENBOSCH

STUDENTE No. 17597099	**TEKENAAR** JG MALLETT	**NAGESIEN**	**SKAAL OP A3** =1:10 **MATE IN** mm **DATUM** 21-03-2017	**TITEL:** FULL ASSEMBLY **VEL No.** 2 **VAN** 2 **VELLE**	**No.** PSR-A-00

IF IN DOUBT ASK

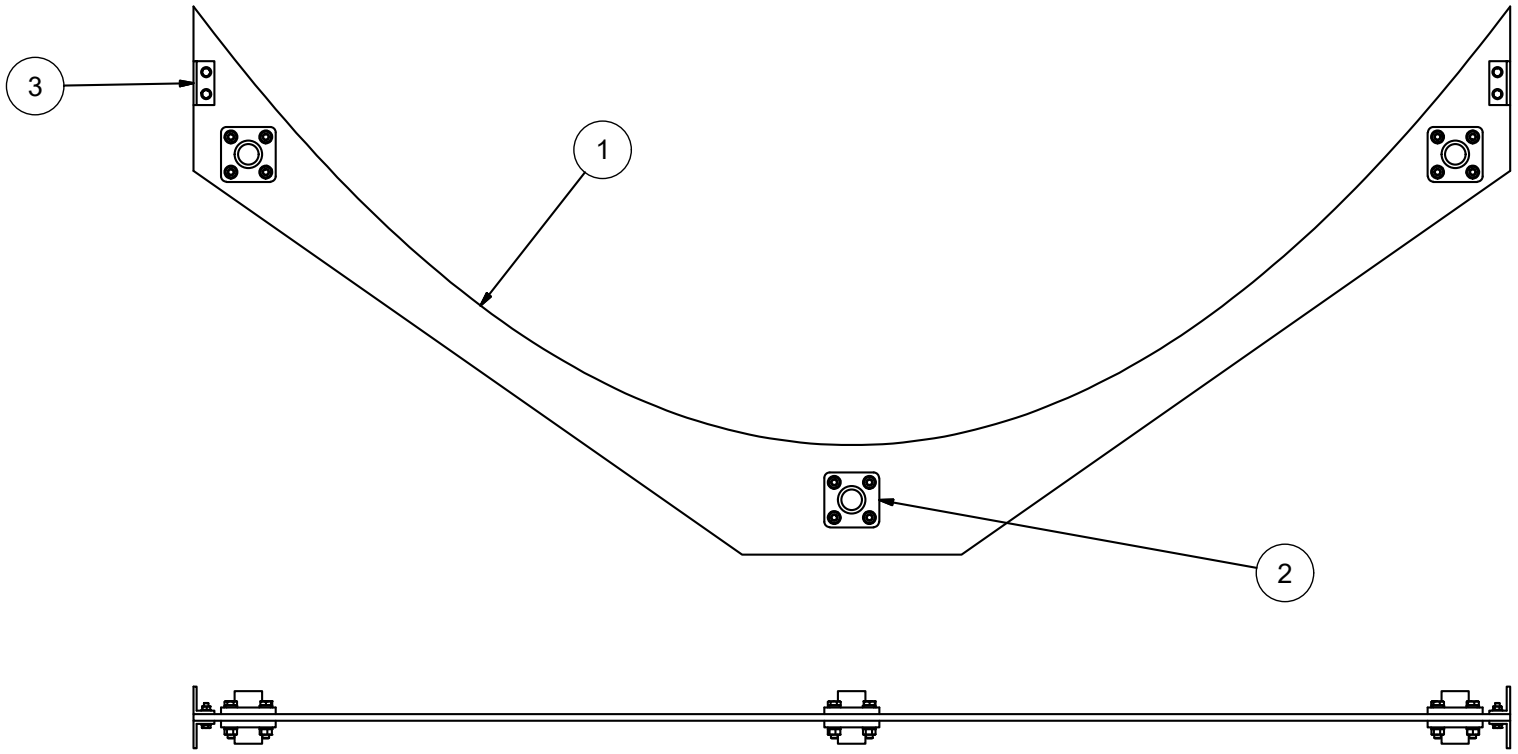

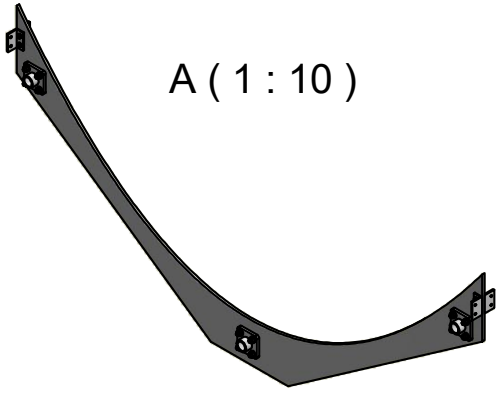

A (1 : 10)

Parts List			
3	90 Deg Clip Mount	4	SEE DRAWING (PSR-P04)
2	Stabilising Mount	6	SEE DRAWING (PSR-P03)
1	Support Rib	1	SEE DRAWING (PSR-P01)
ITEM	BESKRYWING	AANTAL	MATERIAAL / SPESIFIKASIES

APPENDIX B. CAD FILES

99

UNIVERSITEIT VAN STELLENBOSCH

STUDENTE No. 17597099	**TEKENAAR** JG MALLETT	**NAGESIEN**	**SKAAL OP A**3 =1:5 **MATE IN** mm	**TITEL:** MID RIB SUB-ASSEMBLY	
			DATUM 21-03-2017	**VEL No.** 1 **VAN** 1 **VELLE**	**No.** PSR-A-01-01

IF IN DOUBT ASK

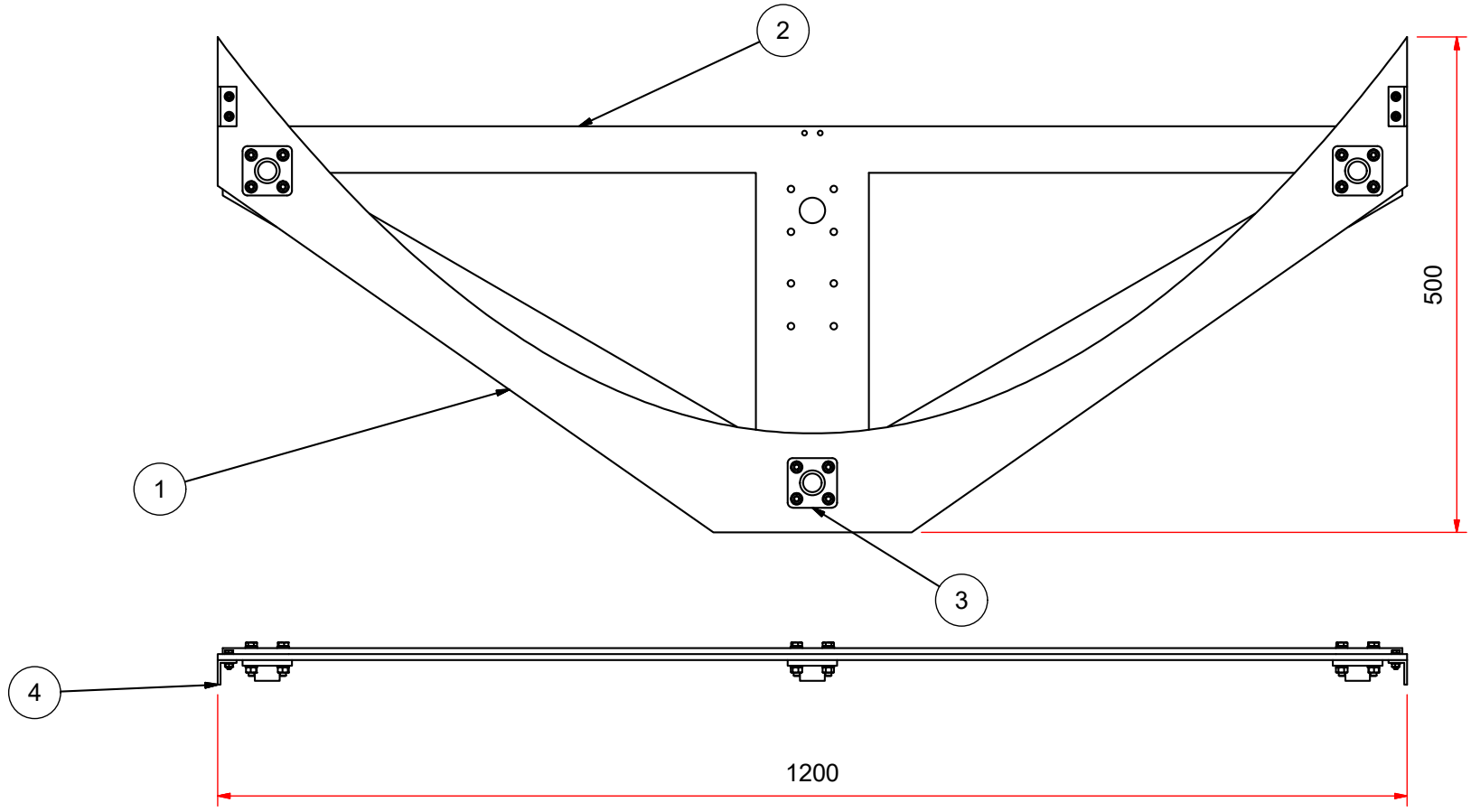

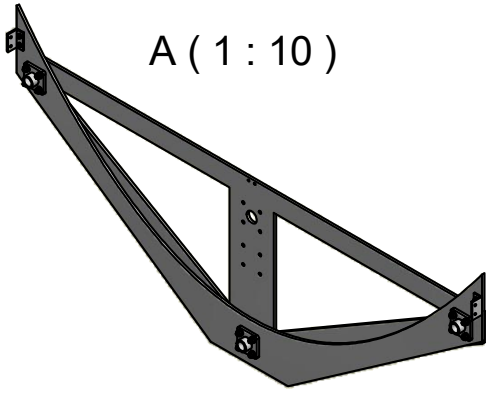

A (1 : 10)

APPENDIX B. CAD FILES

Parts List			
4	90 Deg Clip Mount	2	SEE DRAWING (PSR-P04)
3	Stabilising Mount	3	SEE DRAWING (PSR-P03)
2	End Plate	1	SEE DRAWING (PSR-P02)
1	Support Rib	1	SEE DRAWING (PSR-P01)
ITEM	BESKRYWING	AANTAL	MATERIAAL / SPESIFIKASIES

100

UNIVERSITEIT VAN STELLENBOSCH

STUDENTE No. 17597099	TEKENAAR JG MALLETT	NAGESIEN	SKAAL OP A3 =1:5 MATE IN mm DATUM 21-03-2017	TITEL: END PLATE RIB SUB-ASSEMBLY VEL No. 1 VAN 1 VELLE	No. PSR-A-01-02

IF IN DOUBT ASK

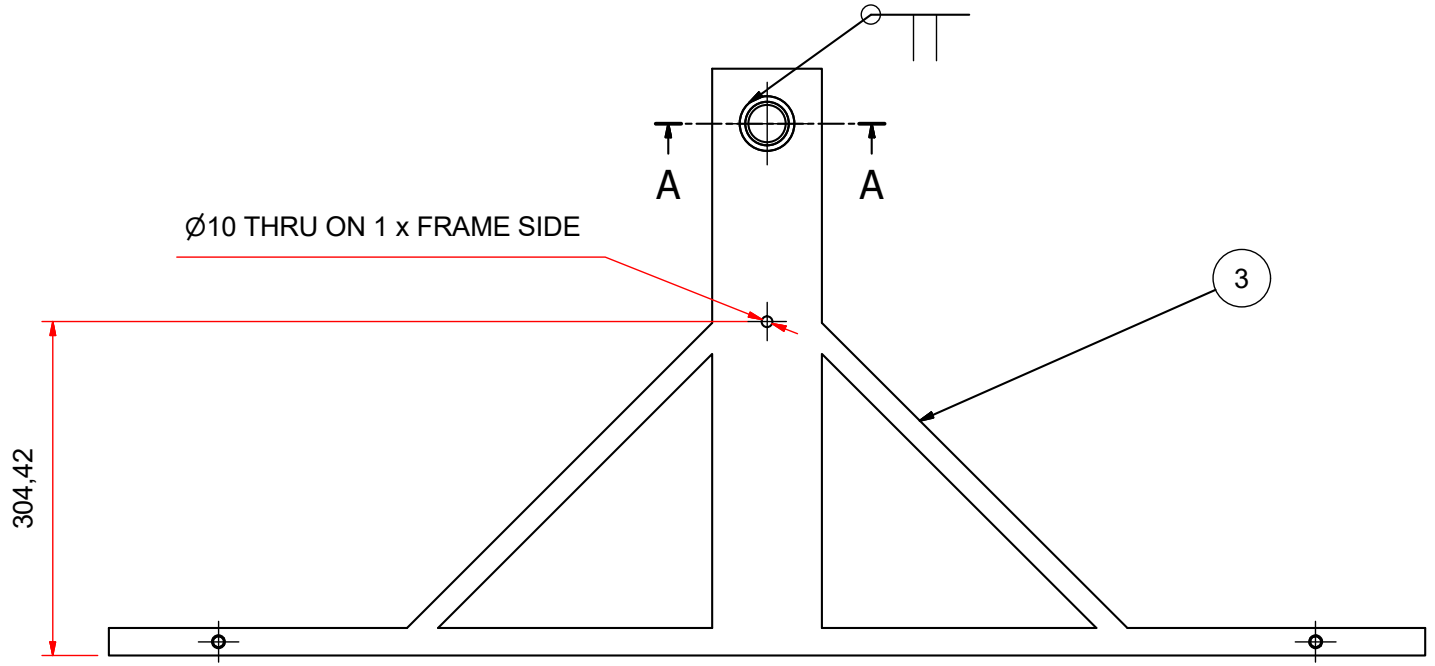

A-A (1:2)

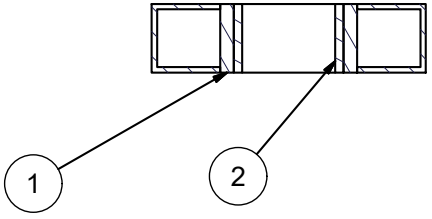

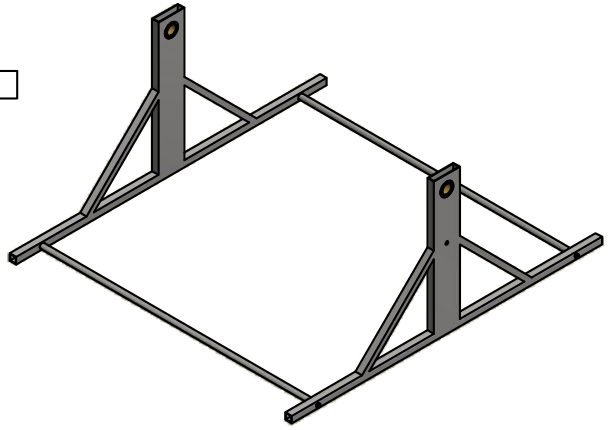

Parts List			
5	Frame Suppor Plug	4	SEE DRAWING (PSR-P12)
4	Frame Stabiliser	2	SEE DRAWING (PSR-P11)
3	Frame	2	SEE DRAWING (PSR-P10)
2	Brass Bush	2	SEE DRAWING (PSR-P09)
1	Bushing Sleeve	2	SEE DRAWING (PSR-P08)
ITEM	**BESKRYWING**	**AANTAL**	**MATERIAAL / SPESIFIKASIES**

101

UNIVERSITEIT VAN STELLENBOSCH

SKAAL OP A3 =1:5		**TITEL:**	FRAME SUB-ASSEMBLY
MATE IN mm			
STUDENTE No. 17597099	**TEKENAAR** JG MALLETT	**NAGESIEN**	
DATUM 21-03-2017	**VEL No.** 1 **VAN** **VELLE** 2	**No.** PSR-A03	

IF IN DOUBT ASK

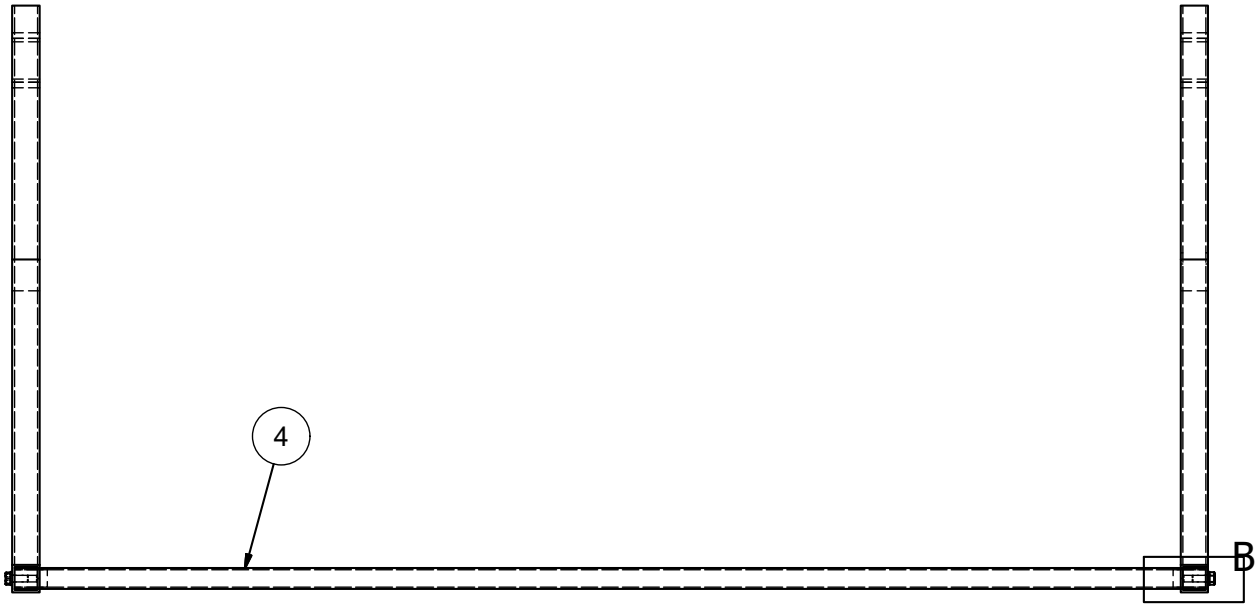

APPENDIX B. CAD FILES

A (1 : 10)

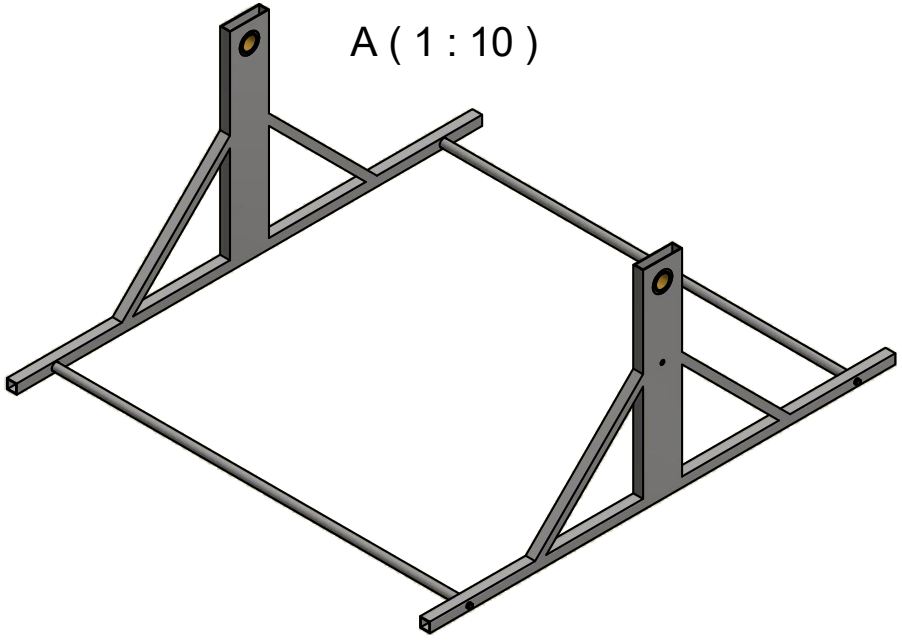

B (2 : 1)

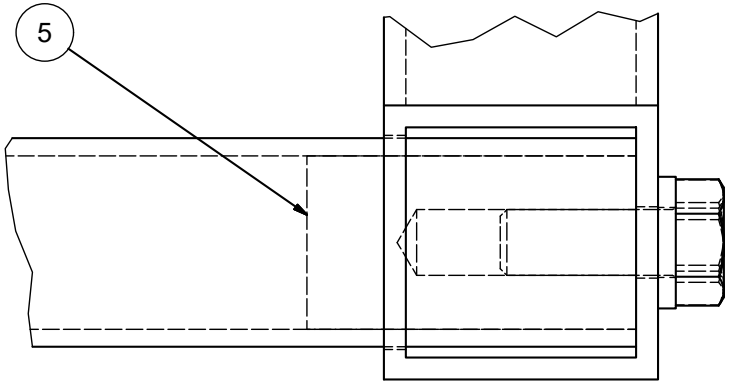

ITEM	BESKRYWING	AANTAL	MATERIAAL / SPESIFIKASIES

UNIVERSITEIT VAN STELLENBOSCH

SKAAL OP A 3 =1:5		TITEL: FRAME SUB-ASSEMBLY	
MATE IN mm			
STUDENTE No. 17597099	TEKENAAR JG MALLETT	NAGESIEN	DATUM 21-03-2017
VEL No. 2 VAN VELLE 2		No. PSR-A03	

102

Appendix C

Operating procedures

This appendix describes the steps taken to set-up, operate and pack away the CSP milk pasteurizer. Following these steps will ensure device is used as designed for, and operates optimally.

C.1 Device set-up

1. Remove the weather resistant cover.
2. Connect flow tubing to 90 degree tees as necessary for input and output flow of HTF.
3. Ensure temperature probes are straight and insert onto each 90 degree tee.
4. Ensure all connections to the input and output 90 degree tees are tightly fastened to avoid leaks (Receiver tube connection, thermocouple connection and flow tubing connection to or from the device).
5. Check power supply to pump, flow controller and data-logger is operational.
6. Switch on data logger and ensure both thermocouples give identical temperature readings.
7. Check reflective sheet is dust and dirt free, clean if necessary.
8. Ensure device is located in direct sunlight where shade will not interfere during the day.

C.2 Device operation

C.2.1 Solar tracking

1. Check solar tracking pin at regular intervals.
2. When the pin casts a shadow, adjust device rotation to maintain correct alignment.
3. Rotate device by pulling the brake rod to disengage the brake and rotating as necessary, releasing brake rod re-engages the brake.

C.2.2 Flow and temperature control

1. Increase or decrease flow rate manually using PWM flow controller to lower and raise output temperature as needed.
2. User is responsible for checking that the flow rate produces the desired output temperature, days with lower DNI will require lower flow rates to achieve higher temperatures.

C.2.3 Cleaning

These steps need to be followed when milk has been used as the HTF, as discussed in Section 2.4.4.

1. When pasteurization has been completed, or milk source has been depleted, switch input fluid source to water.
2. Increase flow rate to maximum to flush remaining milk from system with turbulent flow.
3. Change input fluid to cleaning detergent, lower flow rate to allow output temperature to reach above 70 °C, let the system run like this for several minutes.
4. Flush system again with water at high flow rate.
5. Change input fluid to acidic solution, lower flow rate to allow output temperature to reach above 70 °C, let the system run like this for several minutes.
6. Flush system again with water at high flow rate.
7. Repeat steps 3-6 if necessary.

C.3 Device storage

1. Rotate cleaned device out of direct sunlight.
2. Remove inlet tube from source of fluid.
3. Dry-run pump to ensure all fluid is drained.
4. Unplug and disconnect pump system and data logger.
5. Loosen and remove temperature probes.
6. Remove flow tubing connection from each 90 degree tee joint.
7. Elevate one side of the device to drain any remaining fluid from inside receiver tube.
8. Allow device to stand until remaining moisture has dried out.
9. Cover device with weather resistant cover

C.4 Component replacement

C.4.1 Reflector sheet

Steps to follow when replacing the reflector sheet of the CSP device.

1. Undo fastening and remove one Mirror Clip (Part PSR-P06).
2. Slide out reflective sheet to be replaced.
3. Slide new reflective sheet along the ribs, into place.
4. Reattach and fasten the removed Mirror Clip.

C.4.2 Receiver tube

Steps to follow when replacing the receiver tube of the CSP device.

1. Ensure all electronics and tubing is disconnected from either side of the receiver tube.
2. Remove 90 degree tees from both ends of the receiver tube.
3. To avoid damaging absorber coating, remove tube holders from rotating body.
4. Remove receiver tube to be replaced.
5. Slowly insert new receiver tube, and re-attach tube holders to rotating body.
6. Attach 90 degree tees to both ends of new receiver tube along with all tubing and electronics as necessary.

Appendix D

Matlab code

The following code was used to calculate the solar absorption of the different absorber coatings tested during the course of this project. The code allows for a user to select a csv file containing the solar energy data from 200-2600 nm, and a csv file containing the sample reflectivity measured over the same wavelength range. Both the solar energy spectrum and the reflectivity are then plotted, and the solar absorptivity of the sample is returned.

```
% Load Data Files
[baseFileName, folder] = uigetfile('*.csv','Select the Solar Data file');
fullFileName = fullfile(folder, baseFileName);
Sol = csvread(fullFileName,2,0);
[baseFileName, folder] = uigetfile('*.csv','Select the Reflatance Data file for the Sample');
fullFileName = fullfile(folder, baseFileName);
Sample = csvread(fullFileName,2,0);
Sample=flipud(Sample);

%Layout plot with solar data and reflectivity
xaxis=Sol(:,1)';
hold on;
xlim([280 2600])
yyaxis right
S=plot(xaxis,Sample(:,2),'-r');
ylabel('Reflectance (%)','Color','k')
yyaxis left
sol=plot(xaxis,Sol(:,2),'-');
ylabel('Solar Energy (W*m-2*nm-1)','Color','k')
xlabel('Wavelength (nm)')
z=[S;sol];
legend(z,'Sample','Solar AM1.5');
hold off;
% Calculate the bottom and top of the absorption calculation
bot=trapz(xaxis,(Sol(:,2)));
top=trapz(xaxis,(Sol(:,2).*(1-(Sample(:,2))/100)));
abs=top/bot;
disp('Sample Absorption=');
disp(abs);
```

Appendix E

Test day conditions

This appendix contains some further information about the environment conditions on the days that testing was conducted. Conditions included are the DNI readings, temperature and wind speeds.

Readings were obtained from The South African Universities Radiometric Network (SAURAN) [130] station at Stellenbosch University, roughly 16km from the test site.

E.1 DNI readings on test days

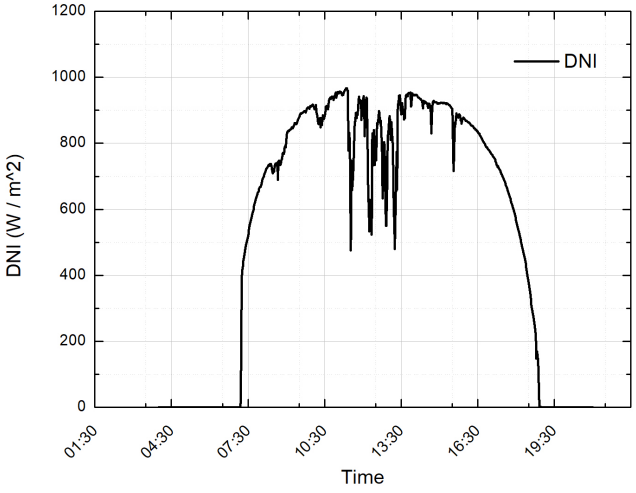

Figure E.1: Test day 1 DNI readings 12-03 [130]

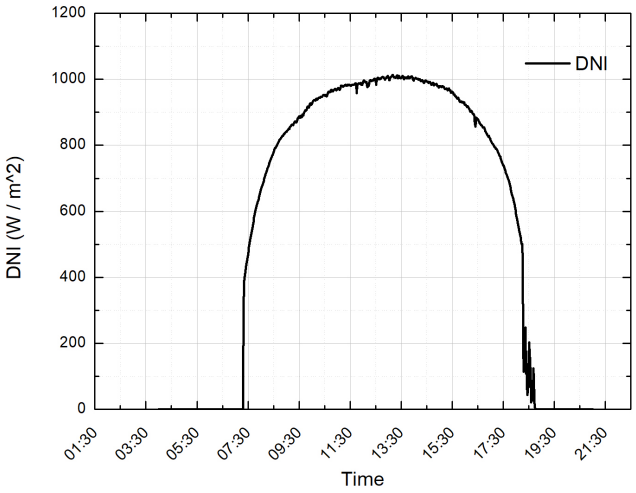

Figure E.2: Test day 2 DNI readings 20-03 [130]

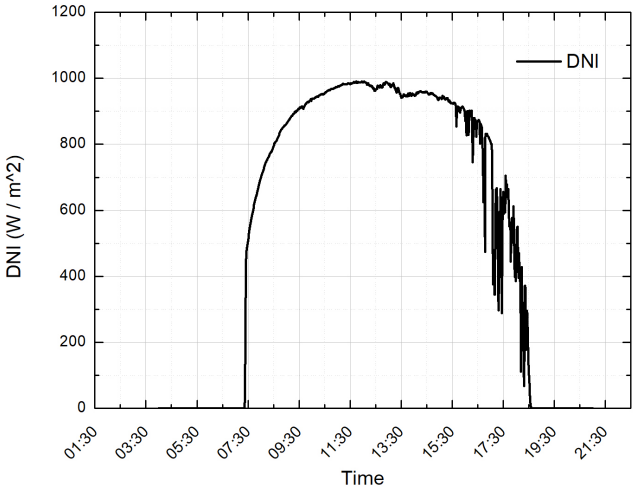

Figure E.3: Test day 3 DNI readings 27-03 [130]

Table E.1: Average DNI over testing periods

Day	Time	Average DNI W/m^2
Day 1	12:30 - 14:00	832.77
Day 2	12:30 - 14:00	1005.06
Day 3	12:00 - 13:30	975.45

E.2 Temperature and wind conditions

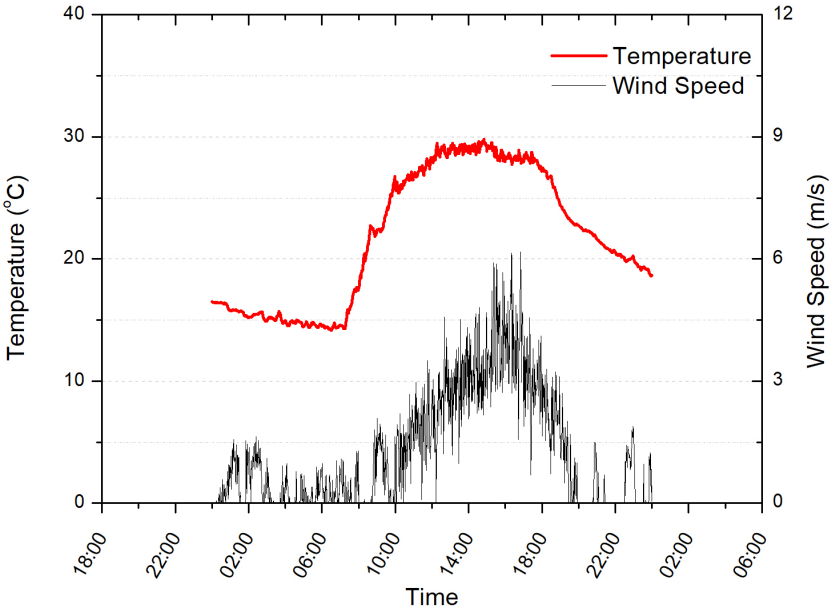

Figure E.4: Test day 1 atmosphere conditions 12-03 [130]

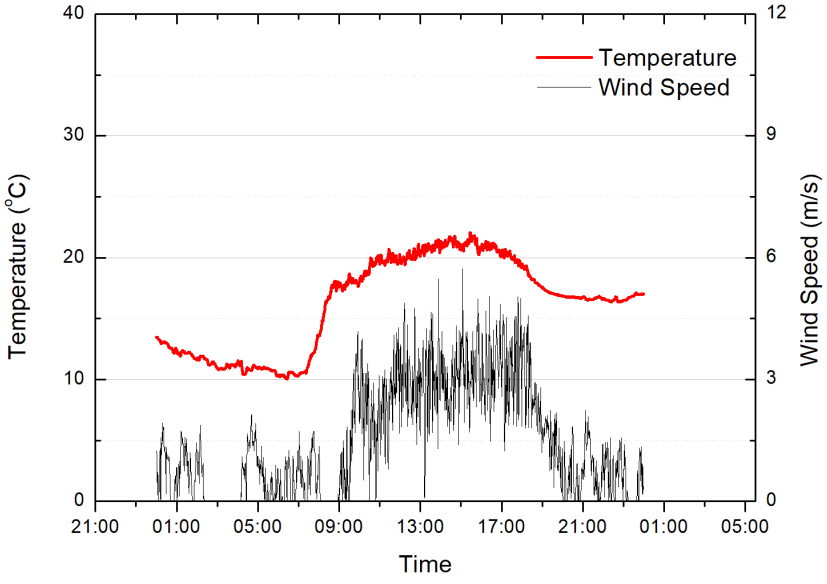

Figure E.5: Test day 2 atmosphere conditions 20-03 [130]

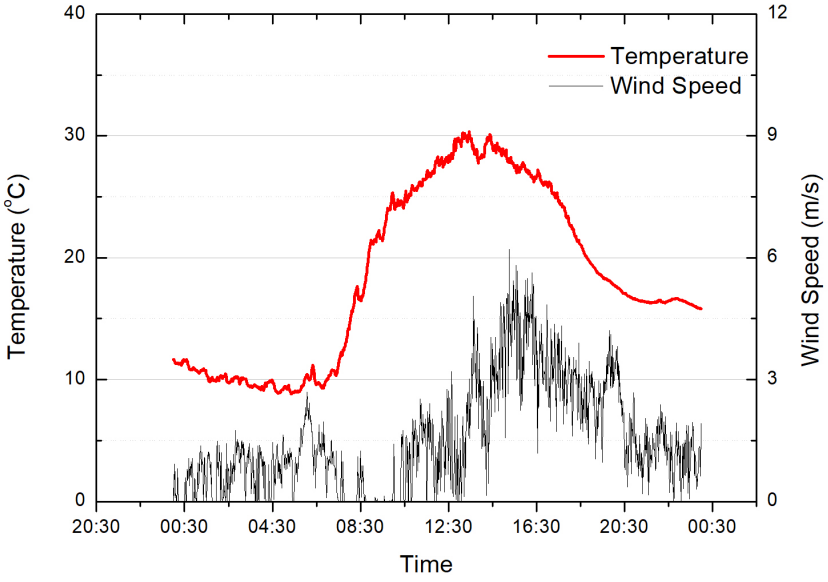

Figure E.6: Test day 3 atmosphere conditions 27-03 [130]

Table E.2: Average temperature and wind speeds over testing periods

Day	Time	Temperature °C	Wind Speed m/s
Day 1	12:30 - 14:00	28.92	2.85
Day 2	12:30 - 14:00	20.64	2.91
Day 3	12:00 - 13:30	28.87	1.32

Appendix F

Publications

Publications that were a result of this thesis.

1. J. G. Mallett, S. Khamlich, M. Maaza. "Comparative study of flat and cylindrically-shaped selective solar absorber for CSP application", *MRS Advances*, 1-10, April 2018. doi: 10.1557/adv.2018.345.

List of References

[1] World Bank, "Sub-Saharan Africa access to electricity," 2018. [Online]. Available: https://data.worldbank.org/indicator/EG.ELC.ACCS.ZS?locations=ZG

[2] J. G. Mallett, S. Khamlich, and M. Maaza, "Comparative study of flat and cylindrically-shaped selective solar absorber for CSP application," *MRS Adv.*, pp. 1–10, apr 2018. [Online]. Available: https://www.cambridge.org/core/product/identifier/S2059852118003456/type/journal{_}article

[3] S. Islam and L. Digneffe, "Investing in Africa: The challenge of agriculture. Spring Edition," Friends of Europe | Internatonal Development, Brussels - Belgium, Tech. Rep., 2014. [Online]. Available: http://www.undp.org/content/dam/rba/docs/IssueBriefs/Fact{_}Sheet{_}InvestingInAfricanAgriculture.pdf

[4] FAO, *Milk and Dairy Products in Human Nutrition. Food and Agriculture Organization of the United Nations*, E. Muehlhoff, A. Bennett, and D. Mcmahon, Eds., Rome, 2013. [Online]. Available: http://www.fao.org/docrep/018/i3396e/i3396e.pdf

[5] A. Bramley and C. McKinnon, "The microbiology of raw milk," *Dairy Microbiol.*, vol. 1, no. Robinson, R.K. (ed.), pp. 163–208, 1990.

[6] V. Holsinger, K. Rajkowski, and J. Stabel, "Milk pasteurisation and safety: a brief history and update," *Rev. Sci. Tech. l'OIE*, vol. 16, no. 2, pp. 441–451, 1997. [Online]. Available: https://www.oie.int/doc/ged/d9152.pdfhttp://doc.oie.int:8080/dyn/portal/index.seam?page=alo{&}aloId=28917

[7] SolarGIS, "Free Solar Resource Maps," 2017. [Online]. Available: http://solargis.com/products/maps-and-gis-data/free/overview/

[8] T. J. Hebrink, "Durable Polymeric Films for Increasing the Performance of Concentrators," in *Third Gener. Photovoltaics*. InTech, mar 2012, ch. 8, pp. 195–196. [Online]. Available: http://www.intechopen.com/books/third-generation-photovoltaics/durable-polymeric-films-for-increasing-the-performance-of-concentrators-

[9] P. Bermel, J. Lee, J. D. Joannopoulos, I. Celanovic, and M. Soljači, "Chapter 7 - Selective Solar Absorbers," *Annu. Rev. Heat Tarns.*, vol. 15, pp. 231–254, 2012. [Online]. Available: https://pdfs.semanticscholar.org/44cc/ef4c0961bc6698fafdabda5f5a63d2ba74b2.pdf

[10] G. Xiao, "A closed parabolic trough solar collector," 2007. [Online]. Available: http://wims.unice.fr/xiao/solar/collector.pdf

[11] SEIA, "About Solar Energy," 2016. [Online]. Available: https://www.seia.org/initiatives/about-solar-energy

[12] E. Morse and A. Turgeon, "National Geographic Society - Solar energy," 2012. [Online]. Available: https://www.nationalgeographic.org/encyclopedia/solar-energy/

[13] J. Buick and R. Zahn, "Overview on Renewable Energy Technology," Tech. Rep., 2004. [Online]. Available: http://www.osce.org/baku/41338?download=true

[14] R. Schleeter, "National Geographic Society - Electricity Generation from Renewable Energy," 2015. [Online]. Available: https://www.nationalgeographic.org/maps/electricity-generation-renewable-energy-sources/

[15] S. K. Juneja, N. Sobti, and A. Wais, "Solar Energy: A Clean Energy System," in *Int. Conf. Renew. Energy Institutes Communities Urban Rural Settings*, R. K. Behl, R. N. Chhibar, S. Jain, V. P. Bahl, and N. E. Bassam, Eds. New Delhi: Agrobios (International), 2012, pp. 228–229. [Online]. Available: http://www.ifeed.org/pdf/media/BOOK{_}Renewable-Energy-Sources-and-their-Applications.pdf

[16] J. H. Gibson, "UVB Radiation: Definition and Characteristics," Colorado State University, Tech. Rep., 2000. [Online]. Available: http://uvb.nrel.colostate.edu/UVB/publications/uvb{_}primer.pdf

[17] Fondriest Environmental Inc., "Solar Radiation and Photosynethically Active Radiation - Fundamentals of Environmental Measurements," 2014. [Online]. Available: http://www.fondriest.com/environmental-measurements/parameters/weather/photosynthetically-active-radiation/

[18] Ammonit Measurement GmbH, "Solar Radiation Measurement," 2017. [Online]. Available: http://www.ammonit.com/en/wind-solar-wissen/solarmessung

[19] Department of Energy, "Renewable Energy - Solar Power," 1999. [Online]. Available: http://www.energy.gov.za/files/esources/renewables/r{_}solar.html

[20] SOLA, "South Africa's Solar Resource Compared to the Rest of the World - SOLA Future Energy," 2017. [Online]. Available: http://www.solafuture.co.za/news/south-africas-solar-resource-compared-to-the-rest-of-the-world/

[21] M. Mendelsohn, T. Lowder, and B. Canavan, "Utility-Scale Concentrating Solar Power and Photovoltaics Projects: A Technology and Market Overview," National Renewable Energy Laboratory, Colorado, Tech. Rep., 2012. [Online]. Available: https://www.nrel.gov/docs/fy12osti/51137.pdf

[22] Office of Energy Efficiency & Renewable Energy, "Linear Concentrator System Basics for Concentrating Solar Power | Department of Energy," 2013. [Online]. Available: https://energy.gov/eere/energybasics/articles/linear-concentrator-system-basics-concentrating-solar-power

[23] Siemens AG, "Siemens - Integrated Solar Combined Cycle (ISCC)," 2017. [Online]. Available: https://www.energy.siemens.com/br/en/fossil-power-generation/power-plants/csp-power-block/

[24] Office of Energy Efficiency & Renewable Energy, "Power Tower System Concentrating Solar Power Basics | Department of Energy," 2013. [Online]. Available: https://energy.gov/eere/energybasics/articles/power-tower-system-concentrating-solar-power-basics

[25] IRENA and EA-ETSAP, "Technology Brief 1: Concentrating Solar Power (CSP)," p. 7, 2013. [Online]. Available: www.etsap.org

[26] SolarPACES, "CSP Technology," 2016. [Online]. Available: http://www.solarpaces.org/csp-technology

[27] PROTERMOSOLAR, "What it is, plant types, benefits," 2015. [Online]. Available: http://www.protermosolar.com/honorificos/que-es-tipos-de-plantas-beneficios/

[28] India Goes Solar, "A Brief on Types of Concentrated Solar Power (CSP)," 2014. [Online]. Available: http://abcofsolar.com/a-brief-on-types-of-concentrated-solar-power-csp/

[29] Office of Energy Efficiency & Renewable Energy, "Dish/Engine System Concentrating Solar Power Basics | Department of Energy," 2013. [Online]. Available: https://energy.gov/eere/energybasics/articles/dishengine-system-concentrating-solar-power-basics

[30] Ennex Developments (Pty) Ltd., "Introduction to Dish Sterling CSP technology," 2011. [Online]. Available: http://www.ennex.co.za/downloads/DishStirlingSolarSouthAfricaConference21June2011.pdf

[31] L. A. Weinstein, J. Loomis, B. Bhatia, D. M. Bierman, E. N. Wang, and G. Chen, "Concentrating Solar Power," *Chem. Rev.*, vol. 115, no. 23, pp. 12 797–12 838, dec 2015. [Online]. Available: http://pubs.acs.org/doi/10.1021/acs.chemrev.5b00397

[32] C. Granqvist, "Solar Energy Materials," *Adv. Mater.*, vol. 15, no. 21, pp. 1789–1803, nov 2003. [Online]. Available: http://doi.wiley.com/10.1002/adma.200300378

[33] C. E. Kennedy and K. Terwilliger, "Optical Durability of Candidate Solar Reflectors," *J. Sol. Energy Eng.*, vol. 127 (2), no. April 2005, pp. 262–269, 2005.

[34] C. Fei Guo, T. Sun, F. Cao, Q. Liu, and Z. Ren, "Metallic nanostructures for light trapping in energy-harvesting devices," *Light Sci. Appl.*, vol. 3, no. 4, p. e161, apr 2014. [Online]. Available: http://www.nature.com/doifinder/10.1038/lsa.2014.42

[35] C. Kennedy, "Review of mid-to high-temperature solar selective absorber materials," *NREL Tech. Rep.*, no. July, pp. 1–58, 2002. [Online]. Available: http://large.stanford.edu/publications/power/references/troughnet/solarfield/docs/31267.pdf

[36] SEIA, "Solar Industry Data," 2016. [Online]. Available: https://www.seia.org/solar-industry-data

[37] J. Chikaire, F. Nnadi, R. Nwakwasi, N. Anyoha, O. Aja, P. Onoh, and C. Nwachukwu, "Solar Energy applications for Agriculture," *J. Agric. Vet. Sci.*, vol. 2, no. September, pp. 58–62, 2010. [Online]. Available: http://www.matchinggrants.org/global/pdf/doc122-89.pdf

[38] OECD/IEA, "Energy for Cooking in Developing Countries," p. Chapter 15, 2017. [Online]. Available: https://www.iea.org/publications/freepublications/publication/cooking.pdf

[39] WHO, "Household air pollution and health," 2016. [Online]. Available: http://www.who.int/mediacentre/factsheets/fs292/en/

[40] P. P. Otte, "Solar cookers in developing countries: What is their key to success?" *Energy Policy*, vol. 63, pp. 375–381, 2013.

[41] M. Wentzel and A. Pouris, "The development impact of solar cookers: A review of solar cooking impact research in South Africa," *Energy Policy*, vol. 35, pp. 1909–1919, 2007.

[42] R. M. Muthusivagami, R. Velraj, and R. Sethumadhavan, "Solar cookers with and without thermal storage: A review," *Renew. Sustain. Energy Rev.*, vol. 14, pp. 691–701, 2010.

[43] C. Z. M. Kimambo, "Development and performance testing of solar cookers," *J. Energy South. Africa*, vol. 18, no. 3, pp. 41–51, 2007. [Online]. Available: http://www.erc.uct.ac.za/sites/default/files/image{_}tool/images/119/jesa/18-3jesa-kimambo.pdf

[44] O. O. Craig, "A stand-alone parabolic dish solar cooker for African conditions," *M.Eng Proj. Report, Stellenbosch Univ. South Africa*, no. December, pp. 1–133, 2015. [Online]. Available: http://hdl.handle.net/10019.1/98096

[45] M. M. Rathore and R. M. Warkhedkar, "A Review of Solar Cookers," *Int. J. Mod. Trends Eng. Res.*, vol. 2, no. 7, pp. 1997–2004, 2015. [Online]. Available: http://www.ijmter.com/published{_}special{_}issues/07-02-2015/a-review-of-solar-cookers.pdf

[46] K. Kuhnke, M. Reuber, and D. Schwefel, *Solar Cookers in the third world*, 2nd ed. Vieweg+Teubner Verlag, 1990.

[47] S. R. Kalbande, A. N. Mathur, S. Kothari, and S. N. Pawar, "Design, Development and Testing of Paraboloidal Solar Cooker," *Karnataka J. Agric. Sci*, vol. 20, no. 3, pp. 571–574. [Online]. Available: http://14.139.155.167/test5/index.php/kjas/article/viewFile/921/914

[48] I. Yaholnitsky, "A Parabolic Trough Baking Device Developed in Lesotho," Brace Research Institute, Mt. Moorosi, Lesotho, Tech. Rep., 2007.

[49] B. A. Fox and A. G. Cameron, "Food spoilage, preservation and hygiene." *Food Sci. - a Chem. approach.*, no. Ed. 4, pp. 315–316, 1982. [Online]. Available: https://www.cabdirect.org/cabdirect/abstract/19781469801

[50] D.-W. Sun, *Thermal food processing : new technologies and quality issues*. CRC/Taylor & Francis, 2006.

[51] WHO, "Zoonoses and the Human-Animal-Ecosystems Interface," 2013. [Online]. Available: http://www.who.int/zoonoses/en/

[52] D. Schoder, A. Maichin, B. Lema, and J. Laffa, "Microbiological Quality of Milk in Tanzania: From Maasai Stable to African Consumer Table," *J. Food Prot.*, vol. 76, no. 11, pp. 1908–1915, nov 2013. [Online]. Available: http://www.ncbi.nlm.nih.gov/pubmed/24215695http://jfoodprotection.org/doi/abs/10.4315/0362-028X.JFP-13-101

[53] J. Munjere, "Pilot investigation of selected milk-borne pathogens in communal cattle in the uMkhanyakude district," Ph.D. dissertation, University of Pretoria, 2017.

[54] Milk SA (NPC), *Dairy Farming in South Africa*, 2nd ed. Cape Town: Leza Putter, 2014. [Online]. Available: http://www.milksa.co.za/sites/default/files/TheMilkSAguidetodairyfarminginSouthAfrica-2ndedition.pdf

[55] A. P. Schutte, J. Kurz, B. J. H. Barnard, and D. J. Roux, "Q fever in cattle and sheep in southern Africa, A preliminary report," *Onderstepoort J. vet . Res*, vol. 43, no. 3, pp. 129–132, 1976.

[56] WHO, "Global Tuberculosis Report," World Health Organisation, Geneva, Tech. Rep., 2016. [Online]. Available: http://apps.who.int/iris/bitstream/10665/250441/1/9789241565394-eng.pdf?ua=1

[57] G. Pappas, P. Papadimitriou, N. Akritidis, L. Christou, and E. V. Tsianos, "The new global map of human brucellosis," *Lancet Infect. Dis.*, vol. 6, no. 2, pp. 91–99, feb 2006. [Online]. Available: http://linkinghub.elsevier.com/retrieve/pii/S1473309906703826

[58] T. Marrie and D. Raoult, "Q fever-a review and issues for the next century," *Int. J. Antimicrob. Agents*, vol. 8, no. 3, pp. 145–161, 1996.

[59] O. Cerf and R. Condron, "Coxiella burnetii and Milk pasteurization: an early application of the precautionary principle?" *Epidemiol. Infect.*, vol. 134, no. 5, pp. 946–951, 2006.

[60] FDA, "The Dangers of Raw Milk: Unpasteurized Milk Can Pose a Serious Health Risk," no. August, 2012. [Online]. Available: https://www.fda.gov/downloads/Food/FoodborneIllnessContaminants/UCM239493.pdf

[61] University of Guelph, "Thermal Destruction of Microorganisms | Food Science," 2017. [Online]. Available: https://www.uoguelph.ca/foodscience/book-page/thermal-destruction-microorganisms

[62] FDA, "Grade A Pasteurized Milk Ordinance," 2015. [Online]. Available: https://www.fda.gov/downloads/food/guidanceregulation/guidancedocumentsregulatoryinformation/milk/ucm513508.pdf

[63] International Dairy Foods Association, "Pasteurization," 2017. [Online]. Available: http://www.idfa.org/news-views/media-kits/milk/pasteurization

[64] R. L. Earle, "Unit Operations in Food Processing - Web Edition," p. Chapter 6, 1983. [Online]. Available: http://www.nzifst.org.nz/unitoperations/httrapps2.htm

[65] Minister of Health: South Africa, "Foodstuffs, Cosmetics and Disinfectants Act (Act No. 54 of 1972)," 1972.

[66] ——, *Government Notice No. R. 1555: Regulations Relating To Milk and Dairy Products*, 1997. [Online]. Available: http://www.milksa.co.za/sites/default/files/milk{_}news/STR012Reg1555-DOHRegulationsremilk{%}2Bdairyproducts.pdf

[67] S. M. Albillos, R. Reddy, and R. Salter, "Evaluation of Alkaline Phosphatase Detection in Dairy Products Using a Modified Rapid Chemiluminescent Method and Official Methods," *J. Food Prot.*, vol. 74, no. 7, pp. 1144–1154, 2011. [Online]. Available: http://jfoodprotection.org/doi/abs/10.4315/0362-028X.JFP-10-422

[68] Advanced Instruments, "Confirming Pasteurization," 2017. [Online]. Available: https://www.aicompanies.com/education/dairy-analysis/confirming-pasteurization/

[69] Cornell University, "Alkaline phosphatase testing for milk pasteurization," Cornell University, Tech. Rep., 2007. [Online]. Available: https://foodsafety.foodscience.cornell.edu/sites/foodsafety.foodscience.cornell.edu/files/shared/documents/CU-DFScience-Notes-Milk-Alk-Phosphatase-11-07.pdf

[70] H. D. Kay and W. R. Graham, "105. The Phosphatase Test for Pasteurised Milk," *J. Dairy Res.*, vol. 6, no. 02, p. 191, may 1935. [Online]. Available: http://www.journals.cambridge.org/abstract{_}S0022029900001333

[71] H. Scharer, "A Rapid Phosphomonoesterase Test for Control of Dairy Pasteurization," *J. Dairy Sci.*, vol. 21, no. 1, pp. 21–34, 1938. [Online]. Available: http://www.sciencedirect.com/science/article/pii/S0022030238956085?showall{%}3Dtrue{%}26via{%}3Dihub

[72] S. Rankin, A. Christiansen, W. Lee, D. Banavara, and A. Lopez-Hernandez, "The application of alkaline phosphatase assays for the validation of milk product pasteurization," *J. Dairy Sci.*, vol. 93, no. 12, pp. 5538–5551, dec 2010. [Online]. Available: http://linkinghub.elsevier.com/retrieve/pii/S0022030210006041

[73] R. Aschaffenburg and J. E. C. Mullen, "A rapid and simple phosphatase test for milk," *J. Dairy Res.*, vol. 16, no. 1, pp. 58–67, 1949.

[74] P. Fox and A. Kelly, "Indigenous enzymes in milk: Overview and historical aspects: Part 2," *Int. Dairy J.*, vol. 16, no. 6, pp. 517–532, jun 2006. [Online]. Available: http://linkinghub.elsevier.com/retrieve/pii/S0958694605002566

[75] C. Payne and R. A. Wilbey, "Alkaline phosphatase activity in pasteurized milk: A quantitative comparison of Fluorophos and colourimetric procedures," *Int. J. Dairy Technol.*, vol. 62, no. 3, pp. 308–314, aug 2009. [Online]. Available: http://doi.wiley.com/10.1111/j.1471-0307.2009.00503.x

[76] R. Black, M. Kuzyk, and J. Duggan, "Evaluation of a fluorometric assay for alkaline phosphatase in fluid dairy products," *Aust. J. Dairy Technol.*, vol. 47, pp. 64–67, 1992. [Online]. Available: https://search-proquest-com.ez.sun.ac.za/docview/356481994?rfr{_}id=info{%}3Axri{%}2Fsid{%}3Aprimo

[77] W. L. Claeys, A. M. Van Loey, and M. E. Hendrickx, "Kinetics of alkaline phosphatase and lactoperoxidase inactivation, and of β-lactoglobulin denaturation in milk with different fat content," *J. Dairy Res.*, vol. 69, no. 04, pp.

541–553, nov 2002. [Online]. Available: http://www.journals.cambridge.org/abstract{_}S0022029902005721

[78] I. Charm Sciences, "Phosphatase Overview - Test Equipment." [Online]. Available: https://www.charm.com/phosphatase-overview

[79] Tetra Pak International SA, *Dairy Processing Handbook*. Tetra Pak International SA, 2018. [Online]. Available: http://dairyprocessinghandbook.com/chapter/cleaning-dairy-equipment

[80] J. Franco, L. Saravia, V. Javi, R. Caso, and C. Fernandez, "Pasteurization of goat milk using a low cost solar concentrator," *Sol. Energy*, vol. 82, no. 11, pp. 1088–1094, nov 2008. [Online]. Available: http://linkinghub.elsevier.com/retrieve/pii/S0038092X07002253

[81] F. O. Wayua, M. W. Okoth, and J. Wangoh, "Design and performance assesment of a flat-plate solar milk pasteuriser for arid pastoral areas of Kenya," *J. Food Process. Preserv.*, vol. 37, pp. 120–125, 2013.

[82] M. F. Atia, M. M. Mostafa, M. F. Abdel-Salam, and M. A. El-Nono, "Solar Energy Utilization for Milk Pasteurization," Ain Shams University, Cairo, Egypt, Tech. Rep., 2011.

[83] R. Zahira, H. Akif, N. Amin, M. Azam, and Z. ul Haq, "Fabrication and performance study of a solar milk pasteurizer," *Pakistan J. Agric. Sci.*, vol. 46, no. 2, pp. 162–168, 2009.

[84] M. S. Al-Soud, E. Abdallah, A. Akayleh, S. Abdallah, and E. S. Hrayshat, "A parabolic solar cooker with automatic two axes sun tracking system," *Appl. Energy*, vol. 87, pp. 463–470, 2010.

[85] A. Sonune and S. Philip, "Development of a domestic concentrating cooker," *Renew. Energy*, vol. 28, pp. 1225–1234, 2003.

[86] W. B. Stine and M. Geyer, "Power From The Sun :: Chapter 8," 2001. [Online]. Available: http://www.powerfromthesun.net/Book/chapter08/chapter08.html

[87] M. Fedkin, "EME 812: Utility Solar Power and Concentration - Concentration with a Parabolic Reflector," 2017. [Online]. Available: https://www.e-education.psu.edu/eme812/node/557

[88] M. Günther, M. Joemann, and S. Csambor, "Advanced CSP Teaching Materials Parabolic Trough Technology." [Online]. Available: http://edge.rit.edu/edge/P15484/public/DetailedDesignDocuments/SolarTroughPreliminaryanalysisreferences/ParabolicTroughTechnology.pdf

[89] P. Pih and S. A. Kalogirou, "Design and Construction of a One-axis Sun-tracking System," vol. 57, no. 6, pp. 465–469, 1997.

[90] S. Lund and F. Struckmann, "Analysis of a Flat-plate Solar Collector," Tech. Rep., 2008. [Online]. Available: http://www.lth.se/fileadmin/ht/Kurser/MVK160/Project{_}08/Fabio.pdf

[91] M. Sodha, S. Mathur, and M. Malik, "Reviews of renewable energy resources. Volume 2," jan 1984. [Online]. Available: https://www.osti.gov/scitech/biblio/6550822

[92] S. A. Kalogirou, *Solar Energy Engineering: Processes and Systems*, 2nd ed. Elsevier Inc., 2014. [Online]. Available: http://ac.els-cdn.com/B9780123745019000042/3-s2.0-B9780123745019000042-main.pdf?{_}tid=1366b6a4-88d7-11e7-8a63-00000aab0f6c{&}acdnat=1503584478{_}8c2ba23b527393c37e61e5c9cf2dde1e

[93] H. M. Guven and R. B. Bannerot, "Determination of error tolerances for the optical design of parabolic troughs for developing countries," *Sol. Energy*, vol. 36, no. 6, pp. 535–550, 1986.

[94] B. Karlsson and C. G. Ribbing, "Optical constants and spectral selectivity of stainless steel and its oxides," *J. Appl. Phys.*, vol. 53, no. 9, 1982.

[95] A. Fernández-García, M. E. Cantos-Soto, M. Röger, C. Wieckert, C. Hutter, and L. Martínez-Arcos, "Durability of solar reflector materials for secondary concentrators used in CSP systems," *Sol. Energy Mater. Sol. Cells*, vol. 130, pp. 51–63, 2014.

[96] Council of Europe, "Council of Europe's Policy Statements Concering Materials and Articles Intended to come into contact with foodstuffs," 2002. [Online]. Available: http://www.mast.is/Uploads/document/guidelines{_}metals{_}alloys{_}used{_}as{_}food{_}contact{_}materials.pdf

[97] Engineering ToolBox, "Thermal Conductivity of Metals," 2005. [Online]. Available: https://www.engineeringtoolbox.com/thermal-conductivity-metals-d{_}858.html

[98] J. H. Hemmer, "Solar Absorptance and Thermal Emittance of Some Common Spacecraft Thermal-Control Coatings," p. 12, 1984. [Online]. Available: https://ntrs.nasa.gov/archive/nasa/casi.ntrs.nasa.gov/19840015630.pdf

[99] SimplyPumps.com, "Tubing Data Sheet." [Online]. Available: http://www.simplypumps.com/pumps/perimax-pumps/pm300.aspx

[100] Verder International B.V. [NL], "Explanation Of Peristaltic Hose and Tube Pumps and How They Work." [Online]. Available: https://www.verderliquids.com/int/en/how-do-peristaltic-pumps-work/

[101] Engineering ToolBox, "Specific Heat of Liquids and Fluids," 2003. [Online]. Available: https://www.engineeringtoolbox.com/specific-heat-fluids-d{_}151.html

[102] S. Khamlich, "Technological applications of aqueous, chemically derived Cr2O3 monodispersed particles," Doctor Technologiae, Tshwane University of Technology, 2012.

[103] Purdue University, "Scanning Electron Microscope," 2017. [Online]. Available: https://www.purdue.edu/ehps/rem/laboratory/equipmentsafety/ResearchEquipment/sem.html

[104] AMMRF, "The electron gun | MyScope," 2014. [Online]. Available: http://www.ammrf.org.au/myscope/sem/practice/principles/gun.php

[105] I. Materials Evaluation and Engineering, "Energy Dispersive X-Ray Spectroscopy | EDS Failure Analysis | EDS Material Analysis | EDX Failure Analysis | EDX Material Analysis," 2014. [Online]. Available: https://www.mee-inc.com/hamm/energy-dispersive-x-ray-spectroscopyeds/

[106] D. o. P. The Chinese University of Hong Kong, "Atomic World - Transmission electron microscope(TEM) - Principle of TEM," 2018. [Online]. Available: http://www.hk-phy.org/atomic{_}world/tem/tem02{_}e.html

[107] Phenom-World, "SEM and TEM: what's the difference?" 2016. [Online]. Available: http://blog.phenom-world.com/sem-tem-difference

[108] B. L. Dutrow and C. M. Clark, "X-ray Powder Diffraction (XRD)," 2018. [Online]. Available: https://serc.carleton.edu/research{_}education/geochemsheets/techniques/XRD.html

[109] Y. Leng, *Materials Characterization: introduction to microscopic and spectroscopic methods*, 1st ed. Singapore: John Wiley & Sons publisher, 2008.

[110] Nanophoton, "What is Raman Spectroscopy? | Nanophoton," 2016. [Online]. Available: https://www.nanophoton.net/raman/raman-spectroscopy.html

[111] Renishaw plc. All rights reserved., "Raman spectroscopy in more detail," 2018. [Online]. Available: http://www.renishaw.com/en/raman-spectroscopy-in-more-detail--25806

[112] R. S. Czernuszewicz, "Resonance Raman spectroscopy of metalloproteins using CW laser excitation," 1993.

[113] Alanod GmbH, "Technical Information," 2018. [Online]. Available: https://www.alanod.com/en/absorption-products/technical-information/

[114] C. V. Thompson, "Solid-State Dewetting of Thin Films," *Annu. Rev. Mater. Res.*, vol. 42, no. 1, pp. 399–434, 2012. [Online]. Available: http://www.annualreviews.org/doi/10.1146/annurev-matsci-070511-155048

[115] F. Leroy, Borowik, F. Cheynis, Y. Almadori, S. Curiotto, M. Trautmann, J. C. Barbé, and P. Müller, "How to control solid state dewetting: A short review," *Surf. Sci. Rep.*, vol. 71, no. 2, pp. 391–409, 2016. [Online]. Available: http://dx.doi.org/10.1016/j.surfrep.2016.03.002

[116] D. T. Danielson, D. K. Sparacin, J. Michel, and L. C. Kimerling, "Surface-energy-driven dewetting theory of silicon-on-insulator agglomeration," *J. Appl. Phys.*, vol. 100, no. 8, 2006.

[117] E. D. Dikio, "Morphological characterization of soot from the atmospheric combustion of kerosene," *E-Journal Chem.*, vol. 8, no. 3, pp. 1068–1073, 2011.

[118] J. Liu, M. Shao, X. Chen, W. Yu, X. Liu, and Y. Qian, "Large-Scale Synthesis of Carbon Nanotubes by an Ethanol Thermal Reduction Process," *J. Am. Chem. Soc*, vol. 125, pp. 8088–8089, 2003.

[119] S. K. Srivastava, V. Vankar, and V. Kumar, "Growth and microstructures of carbon nanotube films prepared by microwave plasma enhanced chemical vapor deposition process," *Thin Solid Films*, vol. 515, pp. 1552–1560, 2006.

[120] R. M. M. Abbaslou, J. Soltan, and A. K. Dalai, "Effects of nanotubes pore size on the catalytic performances of iron catalysts supported on carbon nanotubes for Fischer Tropsch synthesis," *Appl. Catal. A Gen.*, vol. 379, no. 1-2, pp. 129–134, may 2010. [Online]. Available: http://linkinghub.elsevier.com/retrieve/pii/S0926860X10001778

[121] H. Mi, X. Zhang, Y. Xu, and F. Xiao, "Synthesis, characterization and electrochemical behavior of polypyrrole/carbon nanotube composites using organometallic-functionalized carbon nanotubes," *Appl. Surf. Sci.*, vol. 256, no. 7, pp. 2284–2288, jan 2010. [Online]. Available: https://www.sciencedirect.com/science/article/pii/S0169433209014986

[122] M. C. Mbambo, S. Khamlich, T. Khamliche, B. M. Mothudi, and M. Maaza, "Pulsed Nd:YAG laser assisted fabrication of graphene nanosheets in water," *MRS Adv.*, pp. 1–8, 2018. [Online]. Available: https://www.cambridge.org/core/product/5BA8DF9203AF344A74E48373CFBDF359

[123] A. Mastrofrancesco, M. Alfè, E. Rosato, V. Gargiulo, C. Beatrice, G. D. Blasio, B. Zhang, D. S. Su, M. Picardo, and S. Fiorito, "Proinflammatory effects of diesel exhaust nanoparticles on scleroderma skin cells," *J. Immunol. Res.*, vol. 2014, p. 9, 2014. [Online]. Available: http://eds.a.ebscohost.com/eds/pdfviewer/pdfviewer?sid=ab2d40cd-bfc4-4c79-8000-ab12c618603c{%}40sessionmgr4007{&}vid=2{&}hid=4113

[124] F. X. Ouf, P. Parent, C. Laffon, I. Marhaba, D. Ferry, B. Marcillaud, E. Antonsson, S. Benkoula, X. J. Liu, C. Nicolas, E. Robert, M. Patanen, F. A. Barreda, O. Sublemontier, A. Coppalle, J. Yon, F. Miserque, T. Mostefaoui, T. Z. Regier, J. B. Mitchell, and C. Miron, "First in-flight synchrotron X-ray absorption and photoemission study of carbon soot nanoparticles," *Sci. Rep.*, vol. 6, no. August, pp. 1–12, 2016.

[125] Z. Czigany, L. Hultman, and Z. Czigány, "Linköping University Post Print Interpretation of electron diffraction patterns from amorphous and fullerene-like carbon allotropes Interpretation of electron diffraction patterns from amorphous and fullerene-like carbon allotropes Interpretation of elect," *Ultramicroscopy*, vol. 7, no. 110, pp. 815–819, 2010.

[126] E. I. Suvorova and P. A. Buffat, "Electron diffraction from micro- and nanoparticles of hydroxyapatite," *J. Microsc.*, vol. 196, no. 1, pp. 46–58, 1999.

[127] L. E. Murr, K. F. Soto, E. V. Esquivel, J. J. Bang, P. A. Guerrero, D. A. Lopez, and D. A. Ramirez, "Carbon nanotubes and other fullerene-related nanocrystals in the environment: A TEM study," *Jom*, vol. 56, no. 6, pp. 28–31, 2004.

[128] M. Sevilla, C. Salinas Martiez De Lecea, T. Valde-Soli, E. Morallo, and A. B. Fuertes, "Solid-phase synthesis of graphitic carbon nanostructures from iron and cobalt gluconates and their utilization as electrocatalyst supports," *Phys. Chem. Chem. Phys.*, vol. 10, pp. 1433–1442, 2008.

[129] G. A. Heath and J. J. Burkhardt Iii, "Meta-Analysis of Estimates of Life Cycle Greenhouse Gas Emissions from Concentrating Solar Power," *PIX*, vol. 16560, 2011. [Online]. Available: http://www.osti.gov/bridge:http://www.ntis.gov/help/ordermethods.aspx

[130] M. Brooks, S. du Clou, J. van Niekerk, P. Gauche, C. Leonard, M. Mouzouris, A. Meyer, N. van der Westhuizen, E. van Dyk, and F. Vorster, "SAURAN: A new resource for solar radiometric data in Southern Africa," *J. Energy South. Africa*, vol. 26, pp. 2–10, 2015.